FABRICATION OF SOLAR CELL PHOTOVOLTAIC ENERGY SYSTEM USING PULSE ELECTRODEPOSITED $CuIn_xGa_{1-x}Se_2$ ABSORBER UNDER n-TYPE CdS SEMICONDUCTOR FILM WINDOW

A THESIS

Submitted in Partial Fulfilment of the Requirements for the Award of the Degree of

DOCTOR OF PHILOSOPHY

in

CHEMISTRY

by

BOOSAGULLA DIVYA
Roll No. 715094

under the Supervision of

Prof. A. RAMACHANDRAIAH
Professor (HAG) of Chemistry (Retd)
NATIONAL INSTITUTE OF TECHNOLOGY WARANGAL
Hanamkonda, Telangana
(Internal Guide)

Dr. B. V. SARADA
Scientist 'F'
CENTRE FOR SOLAR ENERGY MATERIALS
ARCI, BALAPUR
Hyderabad, Telangana
(External Guide)

to the

DEPARTMENT OF CHEMISTRY

NATIONAL INSTITUTE OF TECHNOLOGY WARANGAL

HANAMKONDA-506004, TELANGANA, INDIA

May, 2022

Dedicated in fond memories to…..

Late BOOSAGULLA VENKATA RAMANA

my mother,

for her endless love, sacrifices, prayers, support and advice

CERTIFICATE

This is to certify that the work embodied in this thesis, entitled, "**FABRICATION OF SOLAR CELL PHOTOVOLTAIC ENERGY SYSTEM USING PULSE ELECTRODEPOSITED $CuIn_xGa_{1-x}Se_2$ ABSORBER UNDER n-TYPE CdS SEMICONDUCTOR FILM WINDOW**", submitted by Ms. Boosagulla Divya in partial fulfillment of the requirements for the degree of Doctor of Philosophy in Chemistry, National Institute of Technology Warangal was carried out under our supervision. Further, the results presented in this thesis have not been submitted previously for the award of any degree or diploma elsewhere.

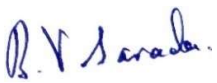

Prof. A. RAMACHANDRAIAH
Professor (HAG) of Chemistry (Retd)
National Institute of Technology Warangal
Hanamkonda, Telangana
Internal Guide

Dr. B.V. SARADA
Scientist 'F'
Centre for Solar Energy Materials (**ARCI**)
Balapur, Hyderabad, Telangana
External Guide

Warangal

30th May, 2022

STATEMENT

I hereby declare that the matter embodied in this thesis, entitled, **"FABRICATION OF SOLAR CELL PHOTOVOLTAIC ENERGY SYSTEM USING PULSE ELECTRODEPOSITED $CuIn_xGa_{1-x}Se_2$ ABSORBER UNDER n-TYPE CdS SEMICONDUCTOR FILM WINDOW",** is based entirely on the results of the research work carried out by me in the Department of Chemistry, National Institute of Technology Warangal and Centre for Solar Energy Materials, (CSEM-ARCI), Hyderabad and the same has not been submitted elsewhere either in part or in full for any degree or diploma.

Warangal **(BOOSAGULLA. DIVYA)**

May, 2022

ACKNOWLEDGEMENTS

I would like to express my sincere gratitude to my supervisors, ***Dr. B. V. Sarada*****,** Scientist F, Centre for Solar Energy Materials (**ARCI**), Hyderabad and ***Prof. A. Ramachandraiah,*** Department of Chemistry, National Institute of Technology Warangal for their guidance and constant encouragement to see important things of chemical research and for the freedom they provided me to do things in my own order. I also want to sincerely thank them for their support, scientific insights, patience and motivation during my PhD studies and research. I am fortunate to work with such supervisors having great enthusiasm and immense knowledge. I am extremely grateful to everyone I have worked with at ARCI, Hyderabad without whom this work would not have been possible. Foremost, I would like to thank the **Director**, International Advanced Research Centre for Powder Metallurgy and New Materials (ARCI), Hyderabad and the **Director**, National Institute of Technology Warangal for providing me with the infrastructure and other necessary facilities to execute the present study in the well-equipped laboratories of ARCI. A lot of special thanks go to ***Dr. Tata Narasinga Rao,*** **Director (I/C)** of ARCI, for his constant support and valuable suggestions during my times at ARCI. I express my warmest thanks to ***Dr. S. Sakthivel*** for his valuable suggestions and also extend my gratitude to ***Dr. Sanjay Dhage*** and ***Dr. Easwaramoorthi Ramaswamy*** for their timely help and cooperation during my PhD work.

I am extremely grateful to ***Dr. M. Sreekanth, Dr. Prashant Misra*** for their technical support on the solar cell characterizations and for fruitful discussions on semiconductor physics. I am also thankful to ***Dr. S. Manasa,*** my dear friend and colleague, for her incredible support, both technically and personally. I thank my fellow lab mates, ***Dr. Brijesh Yadav, Dr. M. Shiva Prasad, B. Ramya Krishna, P. Samhita, Sneha*** and ***Jyoti Gupta*** for the stimulating discussions, I had with them. I express my gratitude to ***Dr. G. Ravi Chandra*** for the excellent training sessions conducted in favor of students to utilize the characterization facilities. My heartful thanks are to ***Dr. Pramod Bors***e for his technical support in photoelectrochemical characterizations. My sincere thanks are also to ***Dr. K. Suresh, Dr. L. Venkatesh, Mr. G. Venkata Ramana Reddy, Mr. K. Ramesh Reddy*** and ***Mrs. Jyothirmayi*** of CMCT at ARCI for the timely slots allotted for the characterization of samples.

I am highly indebted to NIT Warangal and the faculty of the Department of Chemistry for their caring support and guidance in all my academic and official proceedings. I sincerely express my gratitude to the Chairman DSC, ***Dr. Vishnu Shanker,*** Head, Department of Chemistry and the

Members**, *Prof. K. Laxma Reddy, Prof. K. V. Gobi,*** and ***Dr. A. Seshagiri Rao***, for the periodic assessments and their valuable suggestions. I cherish my moments spent with my friends, ***Mr. T. Dhananjaya Rao, Mr. A. Ramesh, Mr. Sunil Kumar, Mr. G. Ambedkar, Dr. Suresh Kumar, Mrs. Arti Gautam, Dr. N. Manjula,*** and ***Dr. Chirra Suman***.

My love and affectionate thanks are to my son, ***Pesaru Sairitish***, who has spent many days with my mom to allow me to focus on my work. I am deeply sorry for the inadequate time I spent with him till now, as a loving mother.

(BOOSAGULLA. DIVYA)

ABBREVIATIONS & SYMBOLS

ED	:	Electrodeposition
PED	:	Pulse Electrodeposition
TCO	:	Transparent Conducting Oxide
mA cm^2	:	Milli Ampere per centimeter square
CV	:	Cyclic Voltammetry
V	:	Potential
EIS	:	Electrochemical Impedance spectroscopy
FESEM	:	Field Emission Scanning Electron Microscopy
HER	:	Hydrogen Evolution Reaction
LSV	:	Linear Sweep Voltammetry
SEM	:	Scanning Electron Microscopy
T	:	Temperature
UHV	:	Ultra-high vacuum
XRD	:	X-ray Diffraction
H	:	Overpotential
Λ	:	Lambda
Σ	:	Ionic conductivity
A	:	Absorption coefficient

ABSTRACT

$CuIn_xGa_{1-x}Se_2$ (CIGS), is a promising p-type semiconductor material for the thin-film solar cell applications. It is known for its high absorption coefficient, direct band-gap. Though, single crystal-based silicon solar cells are commercially dominating till date, the process of making wafers is expensive and is the cause for the higher cost. This prompted the photovoltaic community to look into other options. Thin film solar cells are promising among different generations. In the group of thin-film solar cells, CIGS exhibits excellent stability and has gained potential momentum in the photovoltaic market. As it is well known that Si solar cells are ~ 150-300 μm thick, CIGS is a better option to produce solar cells as only a few microns (3-4 μm) thickness can result in efficient solar cells. The possibility to manufacture flexible solar cells is the most important aspect for their application in portable devices and space applications. Therefore, the production of the all-electrodeposited CIGS solar cells can have the potential to produce cost-effective devices.

The different layers of the device stack are the CIGS, CdS, ZnO and AZO, while CdS is substituted by ZnS in the Cd-free CIGS solar cells. Among these various materials CdS and ZnS are generally chemical bath deposited while CIGS, ZnO and AZO are prepared by vacuum methods such as co-evaporation and sputtering techniques respectively and non-vacuum processes including chemical and electrochemical processes. Generally, a two-stage process is used for the fabrication of CIGS absorber where the CIG precursor is deposited followed by the heat treatment in the presence of selenium (selenization).

In the present thesis, we report a systematic study of the electrodeposition method for different layers to build an all-electrodeposited CIGS solar cell. A hybrid strategy of using both aqueous and non-aqueous electrolytes for CIGS deposition is investigated, which resulted in superior films. The use of additives, such as SDS into non-aqueous electrolyte increased the potential window for metal deposition with good adhesion, finer grains and smoother films. To avoid rapid thermal treatment of CIGS absorber, various post-heat treatment technologies are being investigated. It is observed that multi zone selenization produced competitive films for RTP treated CIGS absorbers. The material properties of phase-pure CIGS with direct bandgap are investigated.

Most crucially, CdS and ZnS are electrodeposited at ambient temperature for the first time to produce crystalline films while optimizing pulse conditions and the organic additives

in the electrolyte. The microstructural examination of films before and after the annealing treatment revealed no change in the grains structure. Moreover, the XRD patterns of the films before and after the annealing treatment revealed no significant change in the crystallinity of as-deposited films. As a result, this method avoids the post-annealing treatment, which is generally recommended during the device manufacture of CIGS solar cells. Thus, our findings reveal that the different layers have improved the electrical and structural properties without any post-heat treatment. Furthermore, AZO films are prepared utilizing a unique process in which Al metal foil is used as the Al source for the first time during thin film electrodeposition. Finally, we fabricated an all-electrodeposited Cd-free CIGS solar cell with a CIGS absorber, a ZnS buffer, and an AZO TCO layer on Mo back contact. To explore the photovoltaic behavior, the device is annealed at various temperatures. CIGS based thin film solar cell is formed by electrodeposition technique for the deposition of all the layers on Mo substrate and formation of the pn junction is observed.

TABLE OF CONTENTS

LIST OF FIGURES

LIST OF TABLES

CHAPTER 1

INTRODUCTION

CHAPTER 1
INTRODUCTION

Solar energy is the most abundant and clean renewable energy source, with enormous potential for electricity generation. Globally, humans consume approximately 1.11×10^{14} KWh of energy, which is provided by the sun in 1 hour 1.78×10^{14} KWh (1). As a result, photovoltaics plays an important role in converting direct sunshine to power. Although solar power cannot meet the world's massive energy demand, careful research and technological innovations can increase the energy sector's market share. With technological advancements, there is a rapid increase in consumption of fuel in developing nations, resulting in an increasing demand for importing fuels that is predicted to climb up by 95 % by 2040 (2). The combustion of fossil fuels creates energy for human needs while emitting CO_2 into the atmosphere, causing global warming, which is the most significant contributor to global climate changes. As a result, using renewable energy sources for energy needs is critical to living a sustainable lifestyle (3). Renewable energy sources include solar, wind, hydro power, wave, tidal and geothermal. These are inexhaustible in nature due to their abundancy. The conversion of these renewable energy into useful electricity would benefit the mankind in terms of reducing greenhouse gases. Diversifying the energy supply from solar power will gradually reduce the dependence on imported fuels. The transformation of renewable energy sources takes place in different ways such as biomass to electrical, solar to electrical, solar to thermal, wind to electrical, biogas to electrical, biogas to thermal, chemical to electrical and potential energy (water) to electrical. Among these, solar to thermal and solar to electrical (photovoltaics) are widely applied energy sources although expensive in conversion process. Therefore, the use of cost-effective methods is highly encouraged in this field of research.

Photovoltaics is often considered as a viable alternative than solar thermal conversion. This is due to the fact that solar thermal utilizes concentrating collectors for trapping direct irradiation to convert to electricity. Thus, the areas with sunnier climate such as deserts is more suitable for solar thermal conversion. While photovoltaics especially thin film technologies can utilize and absorb sunlight even on cloudy days and produces electricity. Therefore, photovoltaics is the more preferred way for conversion of solar energy to electricity.

1.1 Photovoltaic Sector-Global Market

"The diversity, adaptability, and modularity of PV technology distinguishes it from other renewable sources," according to the US Department of Energy (2010, p.1). Until now, the top performing solar modules have been based on monocrystalline silicon, with efficiencies of 26.7 % at the lab scale and 24.4 % at the module level (4).

Figure 1.1 depicts the rise in efficiency of average wafer-based silicon modules over the last ten years, from roughly 12 % to 17 %. At the lab scale, CIGS is around 23.4 % and CdTe is about 22.1 % using thin-film technology, with module efficiencies of 18.6 % for CdTe and 19.2 % for CIGS (5). The efficiency of the multi-junction solar cells was 37.9 % for the three-junction solar cells. Dye-sensitized (DSSC) and perovskite solar cells, which are developing photovoltaics, attained 25.2 % at the lab size (6). These record efficiencies illustrate the possibility for future production efficiency increases. The energy payback of any sort of solar module, however, is totally determined by its geographical position.

1.2 Energy Growth in India and Solar Power

According to the most recent Inter-governmental Panel on Climate Change (IPCC) studies, India is vulnerable to disastrous climate change due to greenhouse emissions that have harmed agriculture. As a result, it is critical to explore for the country's electricity system to absorb clean energy (7). Solar power is extremely dependent on location, making it an obvious choice for a country like India, which has higher number of sunny days with clear sky, per year. Solar cells are the important components for the photovoltaic system **Figure 1.2** that generates free electrons using energy of light and produces electricity.

1.2.1 Solar Cells

The first solar power technology was the invention of solar powered steam engines and water pumps in which sunlight was focused on lenses and mirrors. The most essential part of the solar spectrum, as illustrated in **Figure 1.3**, that may be used by humans is in the range of ultraviolet (UV), visible, and infrared (IR) spectra. The energy of photons is greater at lower wavelengths are essential. As a result, materials that can absorb high-energy photons in order to extract more electricity are required. The present existing silicon solar cells use p type silicon absorber having a band gap of 1.0 eV.

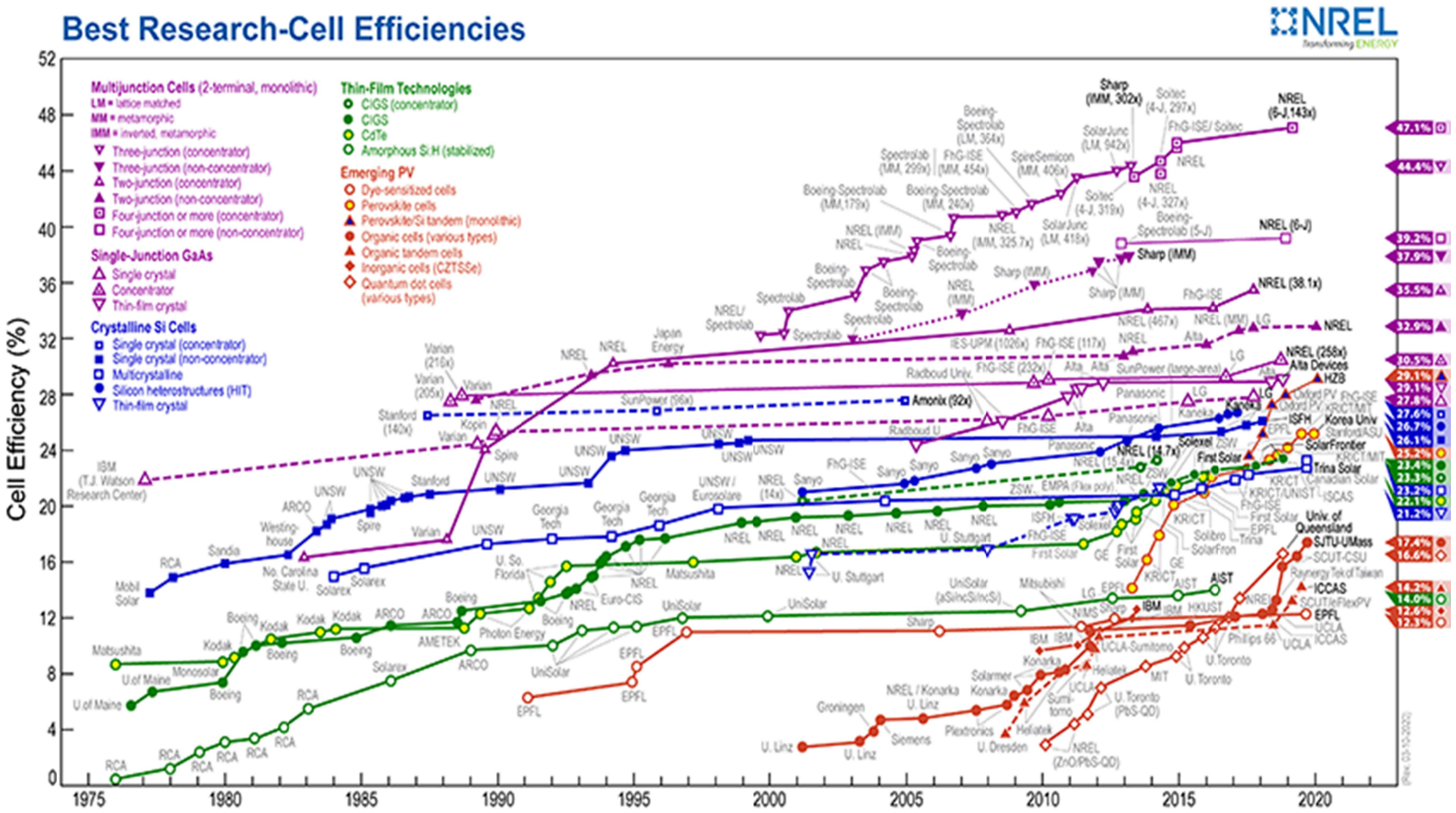

Figure 1.1: NREL chart of efficiencies achieved by different solar cells. Courtesy: NREL

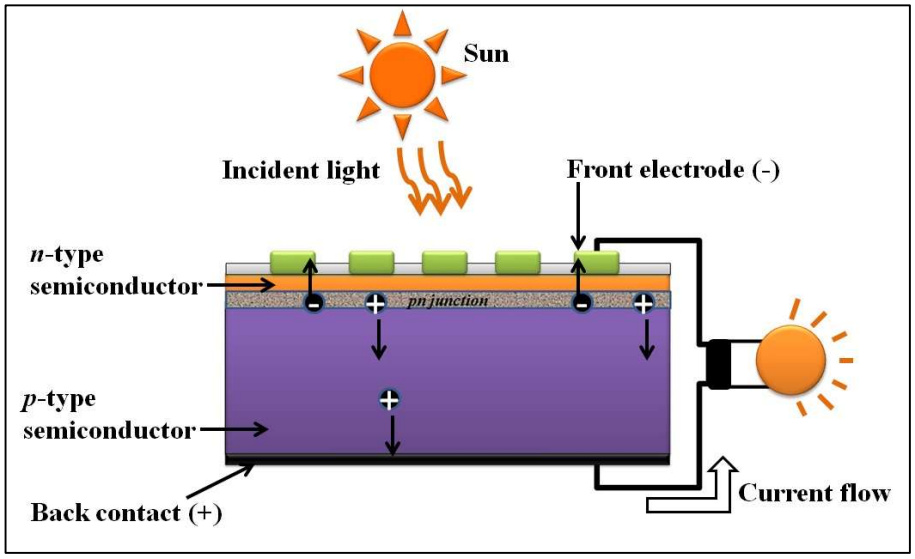

Figure 1.2: Solar power conversion using solar cell

A solar cell is fabricated by forming a *pn* junction that operates as a diode in the dark and generates photovoltage when light is incident. The generated current is proportional to the incident light intensity. Solar cells operate on the concept of "photovoltaic effect". When sunlight strikes a solar cell, various interactions or processes occur, as shown in Figure 1.2. More over half of the Sun's energy is squandered in the form of light, interactions with the atmosphere etc. The energy in the wavelength range of 200-1200 nm is the most usable component of the sun spectrum. When the bandgap of the semiconductor material fits the sun spectrum, it forms electron-hole pairs, which subsequently separate towards the electrode terminals and generate power.

When p-type and n-type semiconductors form a junction, electrons migrate towards the p-type material and holes towards the n-type semiconductor, forming a p-n junction as shown in Figure 1.2. This region is also known as the space charge region/depletion region, and it has built-in electric field. The band energy diagram depicts it, with the slope representing the depletion area. The separation of electron-hole pairs formed by incident sunlight is driven by the existing internal electric field. When the built-in electric field is weak, the charge carriers recombine and the photocurrent is nil (8). When several solar cells are connected in series, it makes a module, and when the modules are connected together, it produces a panel, and when these panels are connected in series, it forms a photovoltaic system. As a result, solar cells serve as the foundation of this photovoltaic system. As a result, the cells are linked in series as a module to boost power generation.

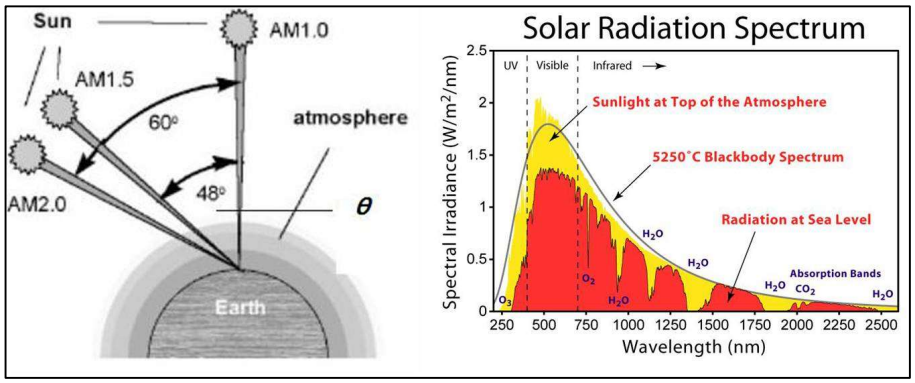

Figure 1.3: Solar spectral irradiance received on Earth and visible part of solar spectrum (9)

On Earth, the incident energy flux spectrum is referred to as air mass 0 (AM 0 = 1366 Wm^{-2}), air mass 1.5 global, and direct (AM 1.5 G and A.M 1.5 D). The AM 1.5 G spectrum 200-2500 nm following various types of reflections and absorptions in the air atmosphere is depicted in Figure 1.3. This is around 1 KWm^{-2} (100 $mWcm^{-2}$) and is a massive quantity of energy. The majority of the light absorbed is in the wavelength range of 300-2000 nm, with a peak at 500-600 nm. The decrease after 1000 nm (near IR) indicates absorption due to CO_2 and H_2O in the environment (9). This divergence from the ideal spectrum is caused by light absorption and scattering. AM 1.0 or AM 1.5 G is the standard solar spectrum used to specify the efficiency of terrestrial cells. A solar cell's conversion efficiency is defined as the ratio of electricity generated by the cell to incident sunlight. Shockley–Queisser analysis, also known as detailed balance limit, is used to calculate the theoretical efficiency limit of any solar cell. This physical phrase describes the highest theoretical efficiency in a solar cell when recombination losses are taken into account (10, 11).

The efficiency of the solar cell is calculated from the current-voltage characteristics. The J-V curve is developed by applying an external load connected to illuminated solar cell. As a result of two counteracting currents the current flows in the circuit. It is theoretically described as

$$I = I_D - I_L = I_0(e^{\frac{qV}{AkT}} - 1) - I_L \quad (1.1)$$

Where I is the total current, I_0 is the saturation current, q the electrical charge, V the applied voltage, k Boltzmann's constant, A the diode ideality factor and T temperature. I_L is the photogenerated current while I_D is the diode current given by characteristics of p-n diode.

Under normal conditions, the highest current value is obtained under short circuit conditions given by

$$I_{sc} = I(V = 0) = I_L \quad (1.2)$$

While V_{oc} open circuit voltage can be obtained from equation below

$$V_{oc} = \frac{AkT}{q} In(\frac{I_L}{I_0} + 1) \quad (1.3)$$

The maximum power is expressed as $P_{max} = I_{max}. V_{max}$ in which I_{max} and V_{max} are obtained from the Fill factor of the IV curve

$$FF = \frac{V_{max}I_{max}}{V_{oc}J_{sc}} \quad (1.4)$$

Therefore, the energy conversion η of the solar cell is defined as

$$\eta = \frac{V_{max}I_{max}}{P_{in}} = \frac{V_{oc}I_{sc}FF}{P_{in}} \quad (1.5)$$

Where P_{in} is the total radiation incident on the solar cell

1.2.2 Different Generations of Solar Cells

The majority of photovoltaic systems in market till date are made of silicon solar cells. This is due to the availability of silica raw material that is abundant in earth's crust. These solar cells are available in two forms monocrystalline and polycrystalline form. The first is made from single crystal silicon material while the polycrystalline solar cells are made from wafers cut from single crystal therefore forming polycrystalline wafers. The solar cell made are of homojunction type as both the p and n type materials are silicon. The p and n type conductivity is obtained by doping phosphorus and boron forming p and n type silicon wafers. Although these are very efficient in energy conversion and dominating the market, the cost of manufacturing opens up possibilities to explore alternative methods for cost reduction. Silicon based solar panels have been prohibitively expensive due to the ingredients needed, which include high purity silicon. The silicon wafers are produced using the "Czochralski" technology, which is expensive due to the usage of vacuum-based equipment to convert raw materials into high quality single crystal and poly-crystalline Si wafers (12). As a result, research into different materials is rising for both terrestrial and space purposes. Figure 1.4 depicts the classification of solar cells into three generations based on their development.

Because silica, which is abundant in the earth's crust, is used as a raw material, first generation silicon solar cells have dominated up to the present day. However, there are significant downsides to the production, which involves highly expensive crystal growth procedures that are

also damaging to the environment. They have an indirect band gap of 1.0 eV and low absorption coefficient, which allows only light with very little energy to be converted into electricity. Therefore, it requires very thick wafers of roughly 200-300 μm. These possess direct band gap with absorption coefficient 10^5 cm^{-1} and hence require only thin layers to convert maximum sunlight into electricity. Thin-film solar cells such as CIGS, CZTS and CdTe are included in the second generation (13). Organic solar cells and tandem solar cells are included in the third and fourth generations, respectively. According to NREL's recent findings, organic solar cells have a significant rise in power conversion efficiency. However, stability difficulties must be addressed before commercialization can take place.

In this context, CIGS solar cells are emerging as promising materials and are seeing tremendous growth in the PV market due to their longer stability. These materials possess direct bandgap that overcomes the limitation of silicon solar cells and is the benchmark for the photovoltaic materials. Solar frontier in Japan, as largest producer has been working on CIGS since 1970s and produced 900 MW at Kunitomi facility with an efficiency of 16.8 %.

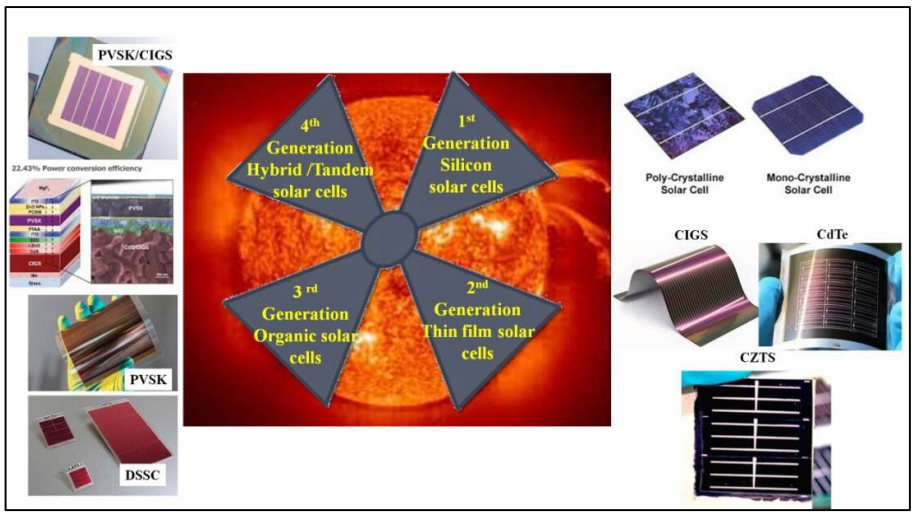

Figure 1.4: Different generations of solar cells

The company's goal is a 20 % module at an output of 220W by 2020 (14). Further, as the technology used for Si solar cells is fully matured for 70 years and approaching the theoretical limits, it is difficult to lower the production cost (4). Thereby, 2nd generation thin-film solar cells as shown in are encouraging in the view of novel designs as thin-film solar cells as well in the tandem solar cells that drive the cost reduction due to their low requirement of materials (15).

1.3 Significance of CIGS Solar Cells

Outstanding semiconductor properties of Cu-In-Ga-Se (CIGS) make it a promising absorber material in thin film solar cells. With a high absorption coefficient of about 10^4 $cm^{-1}$and a flexible optical band gap (1.0 - 1.7 eV) depending on Ga composition), CIGS exhibits a tetragonal unit cell with a lattice parameter ratio c/a close to 2, resulting in tetragonal distortion caused by the different strengths of the Cu-Se, In-Se, and Ga-Se bonds, as shown in Figure 1.5. The characteristic of direct bandgap of this material makes it viable to absorb solar energy in low light even on cloudy days. The band gap can be adjusted by altering the gallium stoichiometric value, which ranges from 1.04 eV (CIS) to 1.68 eV (CGS) (16). Among the desirable features that make CIGS good semiconductors for thin-film solar cells are:

- *p*-type conductivity of the film
- High absorption coefficient (α 10^4-10^5 cm^{-1}) which is equivalent to 90 % of the incident light being absorbed within few nanometers of the thin film.
- Tunable bandgap between that allows to adjust the bandgap to the optimum values of 1.1 eV or 1.3 eV given by Shockley- Queisser limit for maximum power conversion in a single junction solar cell
- It also possesses radiation hardness and long-term stability
- As well the efficiency loss due to recombination at grain boundaries is low compared to other semiconductors

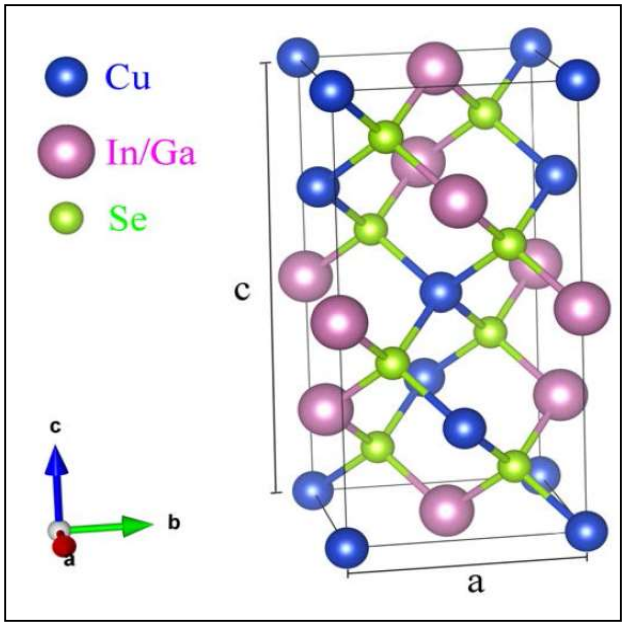

Figure 1.5: Structure of CIGS unit cell(5)

1.4 Advantages of CIGS Thin Film Technology

i. The active layer (CIGS) can be deposited directly onto molybdenum coated on soda lime glass in a polycrystalline form. This requires much lesser energy than producing big crystals, which is necessary in the production of single crystal silicon solar cells.

ii. One advantage of CIGS solar cell technologies over cadmium telluride solar cell panels is that they are more environment friendly since much lower level of cadmium, as cadmium sulfide is used for buffer layer. In some designs, zinc sulfide is used in place of cadmium sulfide for the complete Cd-free device.

iii. High absorption: CIGS being direct-bandgap material absorbs a large portion of the solar spectrum, and achieves the highest efficiency of any thin-film technology.

The substrate configuration of CIGS-based solar cells is shown in Figure 1.6. Molybdenum sputtered on glass serves as a rear contact and forms a conducting base for CIGS deposition.

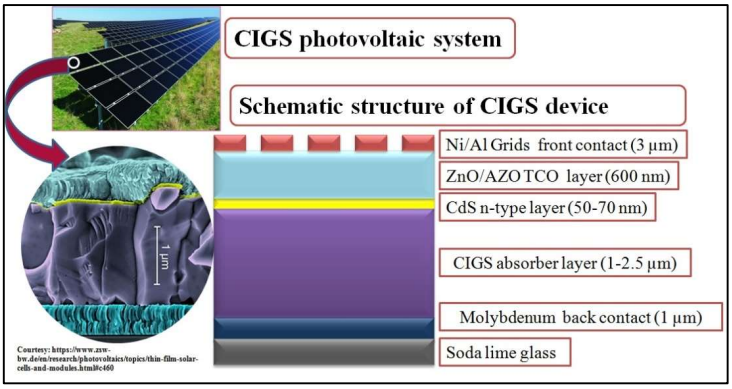

Figure 1.6: Typical structure of CIGS solar cell

1.4.1 Absorber Layer

The thickness of the CIGS is approximately 1 to 1.5 µm. This layer is a p-type semiconductor that aids in the absorption of photons from the sun. When compared to crystalline Si, CIGS has a direct band gap energy with a high absorption coefficient, requiring less material for the fabrication of solar cells. Therefore, this chalcopyrite material is most widely explored and deposited using various vacuum and non-vacuum-based processes. The most conventional method in practice is the sputtering, co-evaporation from the vacuum processes. While electrodeposition, inkjet printing and doctor blade are some of the non-vacuum processes that resulted in better efficiencies.

1.4.2 Buffer Layer

Cadmium Sulfide (CdS) is deposited using a wet chemical method such as chemical bath deposition, with a band gap energy of about 2.42 eV and n-type conductivity, and is incorporated in a solar cell with a thickness of about 50nm, so that the majority of photons are transmitted to the absorber layer and form a pn junction (17). Another important buffer material is the ZnS which is a wide bandgap semiconductor. It has the bandgap of ~ 3.3 to 3.9 eV. It is used as the n-type layer to form the pn junction. It is widely used in the fabrication of Cd-free solar cells. As a result, this layer should have a high transmittance and a low thickness. It also serves as a buffer layer between the CIGS and ZnO layers due to the large band gap differences and protects the absorber layer from the damaging sputtering process of the ZnO and AZO layers. Use of ZnS as buffer layer will omit the toxic CdS and ZnO layers due to its wide bandgap thereby reducing the number of layers in the device fabrication. ZnS is one of the potential semiconductors with special characteristics in thin film technology. The wide bandgap varying between 3.3 to 3.7 eV and thus possess potential applications optoelectronic devices. The presence of wider bandgap favors to deliver more transmittance in the visible range of light. This property expected to increase the creation of electron-hole pairs and thereby increment in the efficiencies. ZnS is fabricated using several methods such as sputtering, atomic layer deposition, screen printing, chemical vapor deposition, molecular beam epitaxy, spray pyrolysis, pulsed laser deposition, chemical bath deposition and electrodeposition.

1.4.3 Transparent Conducting Oxide Layer (TCO)

Intrinsic ZnO has a relatively high resistance and frequently insulates the leakage paths of the CdS layer, thereby increasing the V_{oc}. TCO layer is Al-doped ZnO with a thickness of about 600 nm and a band gap energy of about 3.5 eV (18). This layer transmits almost all of the photon energy to the buffer layer and also serves as the solar cell's front contact. It is also critical to create a better interface between the various layers, as each layer has a different crystal structure, morphology, and lattice constant. Defects at the interface can cause stress, recombination as a result of surface states, and chemical changes as a result of metal interdiffusion.

1.5 Classification of CIGS Thin Film Deposition Techniques

The deposition techniques of thin films can be classified as vacuum or non-vacuum-based based on the capital investment in the manufacturing of CIGS solar cells. Co-evaporation, Sputtering, MOCVD, and Molecular Beam Epitaxy are the best performing vacuum-based methods, as shown in Figure 1.7. Figure 1.8 depicts the non-vacuum-based methods of

Electrodeposition, Ink-jet printing, Spin coating, Spray Pyrolysis, Doctor-blade technique, and Screen printing.

1.5.1 Vacuum Methods

1.5.1.1 Evaporation

Evaporation is a well-known vacuum deposition and in this process the material used for coating is thermally vaporized and then proceeds by potential differences to the substrate. It is capable of depositing any inorganic component. The substrate is heated with tantalum filament and then the metals from individual crucibles evaporate and condense onto the heated substrate under vacuum conditions. The temperature of the substrate ranges from 175 to 400 °C, which promotes crystallization and the formation of a solid film.

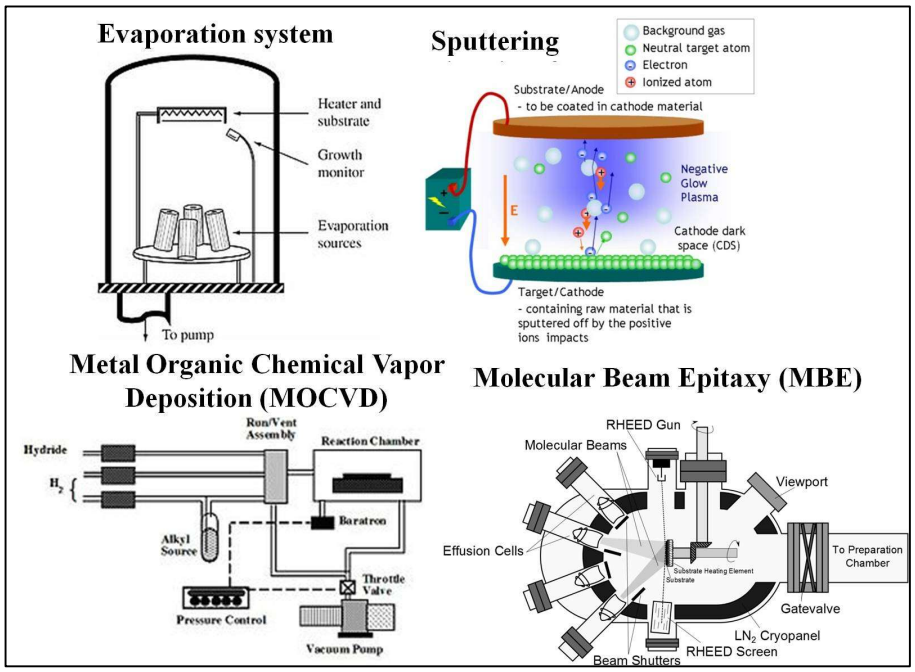

Figure 1.7: Vacuum methods for the fabrication of CIGS absorber (19-21)

After the individual layers of metals are evaporated, the stacks are further evaporated with selenium vapor from the effusion cells and annealed at 450 °C under Ar flow to obtain CIGS film (5). It is the most widely used method for CIGS thin film deposition, in which copper, indium, and gallium are deposited in the correct proportions directly onto the substrate to produce CIG alloy, as shown in Figure 1.7. This alloy incorporates Se by reacting with in situ H_2Se gas or by reacting with Se under rapid thermal processing to form CIGSe. Co-evaporation is a process where these different metals are deposited at the same time. This method of deposition is

advantageous where any inorganic material can be deposited where source of material can be solid in any forma and purity. It can deposit high purity films from high pure source material. The monitoring of deposition rate and control is relatively easy. It is least expensive of PVD techniques. However, only few processing variables are available for film property control which is disadvantageous. Low source material is consumed or utilized. The CIGS devices produced using this method showed the highest efficiency of 22.9 %(22).

1.5.1.2 *Sputtering*

Following evaporation, this is the most commonly used vacuum technique. This method employs plasma to eject Cu, In, and Ga metal atoms from a target cathode containing the metals in the form of alloy. When an electric field is applied to an inert gas, the atoms eject the metal atoms to the anode/substrate, and deposition takes place (23) After sequential sputtering of Cu, In, and Ga, this technique employs rapid thermal annealing (RTP) in the presence of selenium or sulfur at temperatures ranging from 400 to 500 °C for 30 to 60 minutes to produce the highest device quality CIGS. Solar Frontier used this method, which resulted in the highest efficiency of 23.4 % (24, 25). This method is more advantageous in depositing elements, alloys and compounds. The sputtering target provides a stable, long-lived vaporization source. Reactive gases make it feasible to reactive deposition that are activated in plasma. It emits very little radiant heat. On the other hand, sputtering rates are low compared to thermal evaporation which is disadvantageous. The targets used are often expensive and material utilization is low. In reactive sputter mode, the composition of gas must be carefully controlled to prevent poisoning the sputtering target.

1.5.1.3 *Metal Organic Chemical Vapor Deposition (MOCVD):*

This method makes use of epitaxial deposition to produce high purity crystalline thin films with precise tuning. MOCVD systems are made up of heated inert gas flows and heated substrates that are subjected to surface chemical reactions at extremely high temperatures. The precursors are metal organics that are introduced into the reactor and pyrolyzed. The samples are rotated to ensure uniformity, allowing metal to absorb during the reaction. In the case of CIS, a multistep approach is used, with Cu being deposited first, followed by In_2Se_3 and finally heat treated in selenium vapor to produce a single-phase CISe film (26). The CISe solar cells fabricated using this method produced an efficiency of 10.45%(27).

1.5.1.4 *Molecular Beam Epitaxy (MBE):*

This process takes place under ultra-high vacuum conditions, allowing for faster deposition of about 3000 nm per hour with epitaxial growth. The growth chamber is made up of Knudsen cells/effusion cells with Cu, In, Ga, and Se sources. Throughout the deposition, the beam flux is kept constant, while the Se beam flux is varied appropriately to obtain the Se/III ratio. This technique is also very useful in the production of transistors, diodes, and other electronic components. Using the MBE method for the CIGS absorber layer, Nakada et al produced a 16.9 % efficient solar cell.(28).

1.5.2 Non-Vacuum Methods

A large variety of non-vacuum methods are in existence to deposit CIGS thin films. They are crucial due to their low-cost, low operation temperature with high deposition rate. They also possess good yield and reproducibility. The various non-vacuum methods are detailed below.

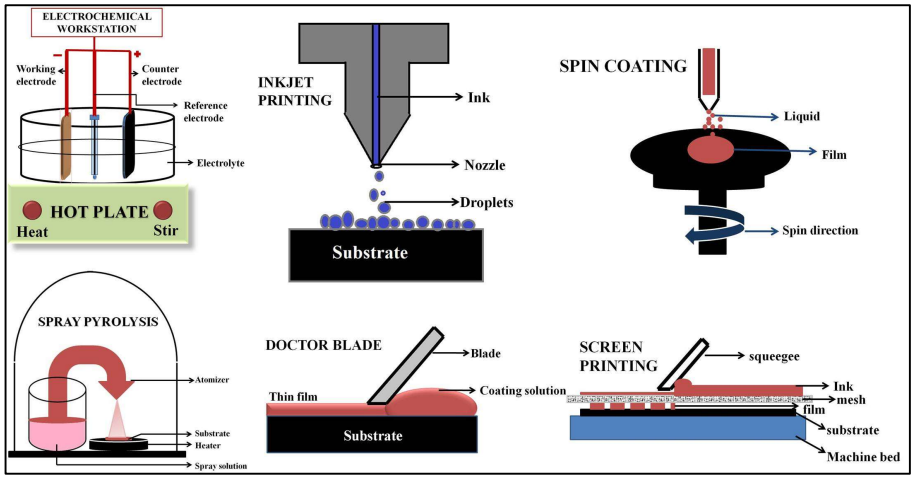

Figure 1.8: Various non vacuum methods for the fabrication of CIGS

1.5.2.1 Electrodeposition

Thin-film electrodeposition can induce the deposition of semiconducting materials such as CIGS over a large area at a low cost when compared to existing vacuum techniques as shown in **Figure 1.8**. The rate of deposition in this method is directly proportional to the applied current/potential. The deposition of Cu, In, Ga, and Se from a single solution is difficult in the case of chalcopyrite semiconductors due to their wide reduction potentials where Cu (E° = +0.34 V vs NHE), In (E° = -0.34 V vs NHE), Ga (E° = -0.53 V vs NHE), and Se (E° = +0.75 V vs NHE) (26, 29). Various schemes are used, however, in which metallic stacks are prepared by sequential deposition of Cu, In, and Ga metals and then selenized to produce CIGS. The second scheme involves sequential deposition of binary selenides such as Cu_xSe, In_xSe_y, Ga_xSe_y, and annealing in an inert

atmosphere. As shown in **Figure 1.9**, the third scheme involves deposition of all four elements from a single pot while shifting the reduction potentials using complexing agents. Because the metals In and Ga tend to form oxides/hydroxides at alkaline pH and are highly soluble in acidic pH and require extremely high potentials to deposit, co-deposition is extremely difficult. As a result, the use of pH 3.0 buffer is common, and the use of additives also plays an important role in the growth of nanostructures from the bottom up along the crystallographic direction. (30). Electrodeposition facilitates the deposition on various shapes and forms. It the most cost-effective method that can produce crystalline thin films. Most importantly it should be noted that individual variables such as frequency, duty cycle can be varied that produces better interfacial bonding between coated material and the substrate. Moreover, it has the feasibility to deposit at room temperature which will minimize the interdiffusion of materials during the multilayer thin film deposition. It also has the provision to monitor the amount of charge delivered which can be related to the thickness of the films. Therefore, it allows the deposition at controlled rate and duration to achieve the desired thickness of the films. The cons of this technique are the entrapping of hydrogen during depositions causing hydrogen embrittlement. Difficulty in deposition of multiple elements. Therefore, deposition is constrained to certain metals.

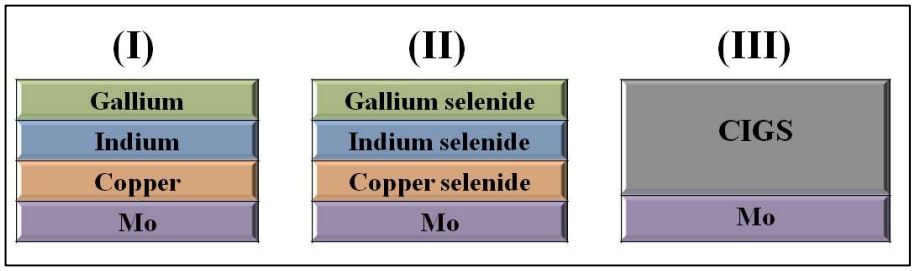

Figure 1.9: Different schemes of electrodeposition of CIGS

1.5.2.2 Inkjet Printing

This method employs a jet printer equipped with a nozzle through which droplets are ejected and projected onto the substrate as shown in **Figure 1.8**. Because it is a non-contact method, the viscosity and contact angle of the ink are critical. To form the film, the settled droplets spread and absorb over the substrate. Cu, In, and Ga precursors are dissolved in organic solvent and stirred and washed for several hours to make CIGS ink. This ink is printed and then annealed in Se vapor to produce CIGS thin film (31). The perovskite solar cells prepared using inkjet printing resulted in higher efficiency of 16.78%(32).

1.5.2.3 Spin Coating

Spin coating is a technique for depositing thin films onto flat substrates that are typically rotated using the spin coater machine's disc as depicted in **Figure 1.8**. Droplets of CIG precursor solution are dispensed onto the substrate, and the rotation is repeated until the desired thickness is achieved, while the solvent evaporates and thickens the coating. To obtain CIGS film, the film is further annealed in an inert atmosphere under selenium vapor (33). one of the reliable methods used for the organic solar cells such as perovskite devices. Recent studies indicated its utilization even for the CIGS based solar cells with good power conversion efficiency of about 13 %(34).

1.5.2.4 Spray Pyrolysis

Pyrolysis is the thermal breakdown of organic materials. When an organic complex precursor solution containing the desired material is sprayed as fine droplets onto a heated substrate, the solvent evaporates and the salts deposit, forming the desired film via a decomposition reaction as seen in **Figure 1.8** (35). Recent study showed that spray pyrolysis of electron transport layer in perovskite resulted in highest efficiency of about 20 %(36)

1.5.2.5 Doctor Blade

This is one of the more cost-effective methods, which involves two steps: ball milling and coating. Ball milling is a simple method for reducing the size of precursor particles while also inducing chemical reactions and synthesizing the product. The powder is then mixed with an organic solvent to form a slurry, which is then dropped over the substrate on one edge and uniformly coated to the other edge with a blade as seen in **Figure 1.8**. To obtain CIGS thin films, the coated films are further annealed in the presence of Se atmosphere. The method is scalable, simple, and cost-effective. However, this technique has a number of drawbacks, including the formation of cracks, poor film adherence, and contamination with the additives (37). It is also recently explored in the optimization of ZnO layer for the organic solar cells. This work resulted in an efficiency of 12.88 %(38).

1.5.2.6 Screen Printing

Screen printers employ a mesh screen with a design that allows ink to be deposited onto the substrate using a squeegee as shown in **Figure 1.8**. To obtain a dense CIGS film, a particle-based ink prepared from ball milling is used, followed by a rapid thermal annealing step. This method is cost-effective for large-area fabrication, but if the densification is not done properly, it results in porous and cracked films that are harmful to solar cells (39). This method used for CIGS device fabrication resulted in an efficiency of 6 %(40).

1.6 Summary

This chapter has included the fundamentals of photovoltaics as well as the various generations of solar cells. It also explained the relevance of CIGS thin film solar cells and the numerous technologies utilized in all stages of CIGS device fabrication. Sputtering and co-evaporation procedures are known to use 75 % to 80 % material, whereas electrodeposition uses 100 % raw material. Also, when compared to vacuum procedures, electrodeposition consumes less energy. With its several parameters that can be altered to make potent solar cells, electrodeposition appears to be the most successful non-vacuum method. As an outcome, this approach is used and examined in the next chapters for the various thin films layered to generate CIGS solar cells.

References

1. C. f. s. systems, Photovoltaic Energy, in *Factsheets energy*, Centre for sustainable systems, Michigan (2019).
2. E. world, India energy demand_ India will register highest GDP, energy growth among nations through 2040_ OPEC, Energy News, ET EnergyWorld.pdf, in (2018).
3. E. Kabir, P. Kumar, S. Kumar, A. A. Adelodun and K.-H. Kim, *Renewable and Sustainable Energy Reviews*, **82**, 894 (2018).
4. L. C. Andreani, A. Bozzola, P. Kowalczewski, M. Liscidini and L. Redorici, *Advances in Physics: X*, **4** (2018).
5. G. Regmi, A. Ashok, P. Chawla, P. Semalti, S. Velumani, S. N. Sharma and H. Castaneda, *Journal of Materials Science: Materials in Electronics*, **31**, 7286 (2020).
6. J. Y. Kim, J. W. Lee, H. S. Jung, H. Shin and N. G. Park, *Chem Rev*, **120**, 7867 (2020).
7. N. L. Panwar, S. C. Kaushik and S. Kothari, *Renewable and Sustainable Energy Reviews*, **15**, 1513 (2011).
8. I. M. Dharmadasa, *Advances in thin-film solar cells*, CRC press (2012).
9. C. J. Chen, in *Physics of Solar Energy*, I. John Wiley & Sons Editor, p. 110, NY (2011).
10. A. L. a. S. Hegedus, *Handbook of Photovoltaic Science and Engineering*, England (2002).
11. S. Rühle, *Solar Energy*, **130**, 139 (2016).
12. P. U. R. Kenu E. Sarah, Prof. Okafor Ephraim N. C, *International Journal of Engineering Research & Technology (IJERT)*, **9**, 741 (2020).
13. M. A. Mohammadnoor Imamzai 1, Yasmin Hanum Md Thayoob 3, Mohammadreza Forouzanfar 2, A Review on Comparison between Traditional Silicon Solar Cells and Thin- Film CdTe Solar Cells, in *National Graduate Conference 2012*, Universiti Tenaga Nasional, Putrajaya Campus, (2012).
14. J. GIFFORD, The weekend read_ CIGS is back, back again in *pv magazine International*, Australia (2018).
15. H. Shen, T. Duong, J. Peng, D. Jacobs, N. Wu, J. Gong, Y. Wu, S. K. Karuturi, X. Fu, K. Weber, X. Xiao, T. P. White and K. Catchpole, *Energy & Environmental Science*, **11**, 394 (2018).
16. Y.-I. Kim, K.-B. Kim and M. Kim, *Journal of Materials Science & Technology*, **51**, 193 (2020).
17. A. K. Yildirim, *Materiali in tehnologije*, **52**, 667 (2018).
18. S. R. Dhage and A. C. Badgujar, *Journal of Alloys and Compounds*, **763**, 504 (2018).
19. H. Simchi, BACK SURFACE STUDIES OF Cu(In,Ga)Se2 THIN FILM SOLAR CELLS, in *Materials Science and Engineering*, p. 200, University of Delaware, DE (2014).
20. F. Pattini, Growth of oxide thin films for energy devices by Pulsed Electron Deposition, in *Scienza e Tecnologia dei Materiali Innovativi XXI Ciclo*, Università degli Studi di Parma (2009).
21. T. Kobayashi, K. Yamauchi and T. Nakada, *IEEE Journal of Photovoltaics*, **3**, 1079 (2013).
22. M. A. Green, Y. Hishikawa, E. D. Dunlop, D. H. Levi, J. Hohl-Ebinger and A. W. Y. Ho-Baillie, **26**, 427 (2018).
23. P. Misra, S. Mandati, T. N. Rao and B. V. Sarada, *Materials Today: Proceedings*, **39**, 2037 (2021).
24. T. Kato, J. Wu, Y. Hirai, H. Sugimoto and V. Bermudez, *IEEE Journal of Photovoltaics*, **9**, 325 (2019).

25. M. Nakamura, K. Yamaguchi, Y. Kimoto, Y. Yasaki, T. Kato and H. Sugimoto, *IEEE Journal of Photovoltaics*, **9**, 1863 (2019).
26. M. Kemell, M. Ritala and M. Leskelä, *Critical Reviews in Solid State and Materials Sciences*, **30**, 1 (2005).
27. I.-H. Choi, *Thin Solid Films*, **525**, 137 (2012).
28. K. F. Tokio Nakada, and Akio Kunioka, *IEEE TRANSACTIONS ON ELECTRON DEVICES*, **46**, 2093 (1999).
29. S. Mandati, B. V. Sarada, S. R. Dey and S. V. Joshi, in *Semiconductors-growth and characterization*, p. 109, INTECH (2018).
30. M.-H. Yeh, S.-J. Ho, K.-C. Wang, H.-R. Hsu, G.-H. Chen and H.-S. Chen, *Solar Energy*, **129**, 116 (2016).
31. X. Lin, R. Klenk, L. Wang, T. Köhler, J. Albert, S. Fiechter, A. Ennaoui and M. C. Lux-Steiner, *Energy & Environmental Science*, **9**, 2037 (2016).
32. B. Gao and J. Meng, *Solar Energy*, **230**, 598 (2021).
33. A. S. P. Dewi, N. Mufti, Arramel, B. H. Arrosyid, Sunaryono and Aripriharta, Synthesis and characterization of CIGS/ZnO film by spin coating method for solar cell application, in *PROCEEDINGS OF THE 3RD INTERNATIONAL SEMINAR ON METALLURGY AND MATERIALS (ISMM2019): Exploring New Innovation in Metallurgy and Materials* (2020).
34. Q. Gao, C. Cao, J. Ao, J. Bi, L. Yao, J. Guo, G. Sun, W. Liu, Y. Zhang, F. Liu and W. Li, *Applied Surface Science*, **578**, 152063 (2022).
35. B. J. Babu, B. Egaas and S. Velumani, *Journal of Materials Science: Materials in Electronics*, **29**, 15369 (2018).
36. A. Culu, I. C. Kaya and S. Sonmezoglu, *ACS Applied Energy Materials*, **5**, 3454 (2022).
37. M. Kaelin, D. Rudmann, F. Kurdesau, H. Zogg, T. Meyer and A. N. Tiwari, *Thin Solid Films*, **480-481**, 486 (2005).
38. G. Ji, W. Zhao, J. Wei, L. Yan, Y. Han, Q. Luo, S. Yang, J. Hou and C.-Q. Ma, *Journal of Materials Chemistry A*, **7**, 212 (2019).
39. H.-P. Kuo, H.-A. Tsai, A.-N. Huang and W.-C. Pan, *Applied Energy*, **164**, 1003 (2016).
40. V. Sousa, B. F. Gonçalves, Y. S. Rosen, J. Virtuoso, P. Anacleto, M. F. Cerqueira, E. Modin, P. Alpuim, O. I. Lebedev, S. Magdassi, S. Sadewasser and Y. V. Kolen'ko, *ACS Applied Energy Materials*, **3**, 3120 (2020).

CHAPTER 2

LITERATURE REVIEW

CHAPTER 2
LITERATURE REVIEW

Thin film solar cells are considered as economically friendly in regards to deposition processes. Many solution-based methods as mentioned in the earlier chapter 1 are explored to deposit thin film solar cells (CIGS, CdTe, CZTS), Among which electrodeposition is convenient for the deposition on complex/rough surfaces with excellent stability. It also provides better crystallinity when compared to other solution-based approaches. Therefore, electrodeposition plays a vital role in semiconductor industry.

2.1 Electrodeposition of CIGS Absorber

Over the two last decades, much research has been conducted on the deposition of CIGS absorber using various methods, as discussed in the previous chapter. Vacuum-based techniques such as sputtering and co-evaporation have been extensively investigated in the literature for CIGS deposition and have achieved the highest efficiencies at commercial scale.

In recent years, breakthrough efficiencies in CIGS absorber with post-deposition alkali treatment (PDT) have been achieved. Jackson et al. reported 21.7 % with a CIGS absorber in which modified substrate is used where the soda-lime glass is deposited with a thin layer of alkali-aluminosilicate followed by molybdenum. During the co-evaporation of the CIGS, this modified substrate diffuses the alkali metal into the absorber, and which occurs during post deposition alkali treatment over the absorber (1). This group also reported a 22.6 % increase in efficiency with the PDT using RbF. The proposed method was tested experimentally, and the device performances were demonstrated using different alkali precursors such as KF and CsF. It was discovered that heavier metal doping increases the J_{sc} and FF with negligible variation in the V_{oc}. Similarly, several researchers have adapted the treatment to date and improved the efficiencies with variation in other stack layers (2). Kato et al. have demonstrated an efficiency of 22.9 % with Cs-treated CIGSSe absorber having CdS as buffer layer (3). However, in order to produce a Cd-free solar cell the CdS is replaced with a modified double buffers Zn(O,S,OH)/ZnMgO, that enhanced the J_{sc} dramatically, resulting in a 23.4 % efficient CIGSSe solar cell. This group investigated the sulfurization treatment after co-evaporated CIGSe absorber selenization, followed by Cs treatment. Although the precise role of

Cs is unknown, the inclusion of a Zn-based double buffer is known to prevent metal interdiffusion into the absorber, thereby increasing the J_{sc} due to low recombination (4). Most studies emphasize the advantages of vacuum techniques in production while downplaying their limitations, particularly in terms of investment and material utilization of the industrial line.

The use of non-vacuum-based CIGS production techniques effectively addresses the aforementioned concerns. As described in section 1.5.2 there are several processes such as electrodeposition, ink-jet printing, spray pyrolysis, spin coating, and doctor blade procedures. In all the processes outlined, the CIGS is produced in two steps, with the CIG precursor deposited at low temperatures and subsequently transformed to CIGS by a high temperature annealing treatment. Furthermore, material waste is minimized, and these methods can operate at low temperatures, resulting in low capital investment compared to vacuum procedures. Because of its low cost and convenience of use, electrodeposition is the only technology discussed above that has reached the commercial level.

Bhattacharya's group at NREL investigates and documents early development in electrodeposited CIGS. They reported an efficiency of about 12.3 % for the electrodeposited CIGS absorber prepared from single step DC deposition, with the composition of In and Ga later adjusted by the PVD technique (5). Later, the same group deposited CIGS with successive layers of Cu-In-Ga metallic stack and annealed it in a selenium atmosphere, yielding an 11.7 % efficiency (6). Murali et al investigated pulse electrodeposition and deposited CIGS at constant current with a duty cycle of 50%, resulting in a 6.6 % efficient device (7). Nexcis developed another novel approach in which CIG precursors are deposited in two steps and then annealed in a sulfur atmosphere to produce $Cu(In,Ga)(S,Se)_2$. Broussillou et al used this approach to report the most efficient device 17.3 % of electrodeposited absorber over 0.5 cm^2 and 14.0 % for the module size 60 × 120 cm^2 (8). These approaches are promising and are being studied by a number of researchers. Gao et al. recently proposed a novel metal precursor structure in which antimony (Sb) is electrodeposited onto the molybdenum back contact. The CIGS absorber 360 nm has reported 11.3 % that is processed by sequential deposition of Sb/Cu/In/Ga layers followed by metal precursor selenization. The presence of Sb had a significant impact on grain growth, resulting in reduced interface recombination (9).

2.2 Pulse Electrodeposition of CdS at Room Temperature

CdS is an n-type semiconductor possessing a bandgap of ~ 2.4 eV exhibits high transmittance in visible region (10). CdS should be as thin as possible (~ 50 – 70 nm) to enhance optical transmission and to reduce reflection from cell surface due to its lower refractive index than the p-type material (11). In addition, CdS is an excellent material for the application as photoanode in photoelectrochemical (PEC) hydrogen generation. Conduction and valence band edges of CdS are appropriate for water splitting thereby making it an extensively studied semiconductor for PEC water splitting. Considering these aspects, it is important to develop a low-cost method for the fabrication of CdS thin films. Also, since CdS is to be coated on thin-film absorbers, the conformal coverage is crucial which decides the device performance. Therefore, several solution-based approaches including spray pyrolysis (12), dip coating (13), chemical bath deposition (CBD)(14) and electrodeposition(15) have been utilized for the deposition of CdS films. Among these CBD is the most widely used method for the CdS deposition (11, 14). CBD involves a chelating agent such as liquid ammonia which complexes with cadmium salt and avoids the formation of hydroxides while thiourea releases sulfide ions (16). CBD is generally performed at slightly high temperatures (60-70 ºC) (17), often leading to the formation of excess precipitates and sediments in the solution which are hazardous environmentally when disposed of in large scale.

The highest efficiencies of thin film solar cells are obtained by employing CBD-CdS. This is due to adsorption and reactive process of CdS formation during CBD technique which is simpler than any other vacuum-based approaches. Moreover, it is cost-effective and the CdS deposited also possess good pn junction properties. This is due to formation of buried heterojunction through Cd-doping of CIGS as depicted in **Figure 2.1**. In addition to CBD, several reports have appeared on electrodeposition of CdS films using ionic liquids (10), aqueous (17) and non-aqueous electrolytes (18) at different process conditions (19). At the very beginning, CdS was electrodeposited by anodizing Cd where Na_2S was utilized as sulfur precursor (20). In addition, there are studies available on electrodeposition of CdS on different substrates from aqueous electrolytes (21, 22). These studies often involve longer deposition time of 2 hr at a temperature of 70-80 ºC to obtain a thickness in the range of 100-200 nm (22).

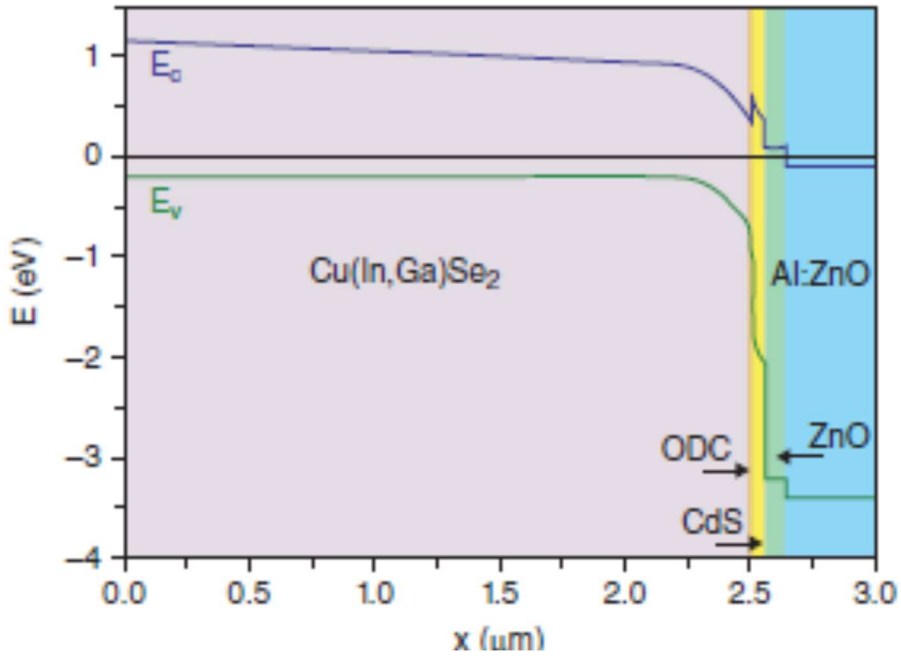

Figure 2.1: Energy band diagram of CIGS solar cell (23)

Dharmadasa et al. have explored the use of thiourea and ammonium thiosulfate as sulfur precursors with HCl for electrodeposition of CdS thin films at 85 ºC for 2hr, where the as-deposited films exhibited a mixture of cubic and hexagonal phases (24). The study, however, utilized a post-deposition heat-treatment in the presence of $CdCl_2$ to obtain pure hexagonal CdS films. Nishino et al electrodeposited CdS using $CdSO_4$, $Na_2S_2O_3$ with H_2SO_4 as supporting electrolyte and glycerol was added to adjust the pH to higher values so as to avoid the formation of excess colloidal sulfur, which often occurs in low pH regime (25). It is therefore understood that often strong acids such as HCl and H_2SO_4 are used for the electrodeposition of CdS which is carried out at higher temperatures (60-90 °C) and use of such acid's forms colloidal sulfur and sediments quickly leading to the deposition of particulates which, in turn, degrades the quality of films and reduces the availability of sulfur ions in the electrolyte (26). On the other hand, electrodeposition of CdS films is generally performed by the conventional direct current (DC) technique (24) where additives such as ethylene glycol (18), EDTA (27) are used to control the composition of Cd & S and achieve smooth films. It is well known that DC electrodeposition process has limited variables like deposition potential and time which often results in rough and porous deposit due to the continuous supply of current or potential in addition to hydrogen evolution during deposition (28). On the other hand, pulse electrodeposition has additional process

control variables such as pulse on-time and off-time which can be conveniently modulated to control the composition of individual elements, the morphology and reduces the effect of hydrogen evolution on the deposit (29). Despite these additional process parameters and advantages of PED, limited reports are available on pulse electrodeposition of CdS films. In addition, the reports have often utilized high temperatures during deposition and/or post heat treatment step for achieving uniform crystalline CdS films (22).

Morris et al. used a three-electrode system to create 11.5 % efficient superstrate CdTe solar cells using potentiostatically deposited CdS. Gal et al demonstrated a 11.4 % efficiency CISe solar cell in substrate configuration using co-evaporated CISe absorber, and electrodeposited the size quantized CdS buffer layer from dimethyl sulfoxide (DMSO). They observed competing efficiency with conventional CBD-CdS, which they attribute to the size quantized ED-improved CdS blue response at lower wavelengths. (30). Xiao-Yun Yu et al. demonstrated 4.8 % efficient quantum dot-sensitized solar cells (QDSSCs) with hierarchical TiO_2 sphere electrodeposition of CdS and CdTe quantum dots onto the modified FTO substrate (HTS). They investigated CdS deposition at constant current mode in DMSO at 90 °C using $Cd(NO_3)_2$ and thiourea with Pt as counter electrodes (31).

2.3 Pulse Electrodeposition of ZnS at Room Temperature

Zinc sulfide (ZnS) is within the most versatile semiconductor materials together with ZnO and GaN exhibiting a wide band gap (3.3 – 3.8 eV) owing to the excellent luminescent properties (32-34). Fields of application include light-emitting diodes (LEDs), Bio-LEDs, electroluminescence devices such as backlights in gadgets, soft robotics, artificial skin actuators, wearable electronics, etc, (35, 36) . However, among the thin-film photovoltaic community, with the focus on Cd-free thin-film solar cells, ZnS is the most suitable alternative with its wide band gap compared to its counterpart CdS having a narrow band gap of ~ 2.4 eV. Although CdS is the widely used buffer layer, chemical bath deposition (CBD) process employed for its deposition, results in huge waste containing Cd which is hazardous and carcinogenic causing concern to the environment. Hence, it is necessary to minimize/replace the Cd in electronics which can be a prevention step to protect the environment (37, 38). In extension, the most reliable way to enhance the power conversion efficiency of CIGS thin-film solar cells is to build a heterojunction having minimal absorption losses. This can be accomplished by the replacement of CdS with a wide band

gap semiconductor material such as ZnS, SnS, ZnSe, and In_2S_3 (39), etc. Among these, ZnS is perceived to be an eco-friendly material consisting of earth-abundant and non–toxic elements. Due to its wide band gap, a significant increment in the transmission of photons in the visible (400-500 nm) region is observed leading to an increase in short-circuit current density, and hence, is a better choice to replace the CdS (40).

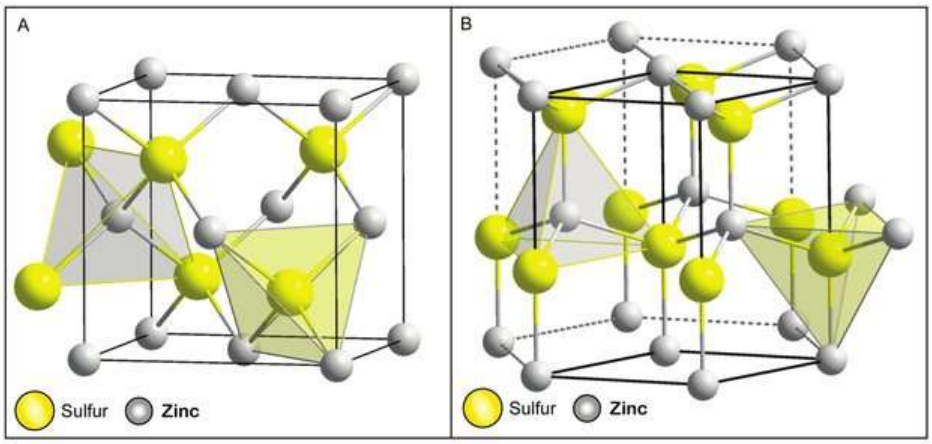

Figure 2.2: Crystal structures of ZnS (A) Cubic (B) Hexagonal (41)

Fundamentally, ZnS crystallizes in cubic and hexagonal structures, and is of interest to notice that cubic ZnS with a lattice parameter of 5.4 A° matches well with that of CIGS (5.6 A°), and is, therefore more apt for CIGS thin film solar cells (41, 42). Various existing methods including chemical bath deposition (CBD) (40), spray pyrolysis (43), RF sputtering (44), atomic layer deposition (45), electrodeposition (ED), etc are adopted for the deposition of ZnS thin films (46-48). Among these, CBD is frequently chosen, wherein the formation of Zn(O, S) is reported. Despite the presence of oxygen, the devices fabricated have evinced remarkable efficiencies owing to its band gap of 3.2 eV. However, there are very few reports available on the electrodeposited ZnS films for solar cell applications (49, 50). Sanders et al. are the early to report electrodeposition of ZnS using glycerol in acidic solutions where the ZnS films have an uneven distribution of grains with cubic phase (200) orientation on ITO substrate (51). A study on the effect of the duty cycle has demonstrated the variation in the band gap of the ZnS films deposited using galvanostatic pulse electrodeposition at room temperature (52). Other articles on pulse electrodeposition at elevated temperatures has disclosed the cubic (200) and hexagonal (002) ZnS, using sodium thiosulfate as a sulfur precursor (53, 54). On contrary, the depositions at an elevated temperatures

using ammonium thiosulfate as sulfur precursor led to ZnO impurity (55). Therefore, it is inferred that the choice of precursors can adversely affect the formation of phase pure ZnS. Further, alkaline electrolytes are also explored to avoid rapid precipitation of sulfides which has resulted in the formation of ZnO along with ZnS. Thus, it is evident that deposition in acidic solutions accelerates the formation of ZnS and subdue the oxides (56). Another pertinent report is the effect of precursor concentrations that have reported n-type ZnS from the zinc-rich electrolyte and p-type ZnS from the sulfur-rich electrolyte with added heat treatment (57). Hence, the outcome of post deposition treatment has shown a positive impact on the optical and electrical properties of the ZnS films (55, 58).

In general, CBD method is utilized to deposit the ZnS layer in the CIGS solar cells. Nakada et al. have explored the CBD-ZnS and have recorded an efficiency of 18.6 % for CBD-ZnS(O, OH) and 18 % for CBD-ZnS using CIGS absorbers fabricated from co-evaporation technique (59). Recently, Nakamura et al have successfully accomplished the highest efficiency of 23.35 % for the Cd –free CIGSSe solar cells while substituting CdS/ZnO layers with Zn(O, S, OH) deposited using CBD (4). The potential benefit of CBD deposited ZnS as buffer layer is also explored for the CZTS solar cells and an increment in the efficiencies is reported with the bilayer to CdS/ZnS as buffer layer compared to CdS alone (60). Apart from the CBD process, electrodeposition is an affordable choice that can produce ZnS films. ZnS is also deposited by electrodeposition from aqueous solutions and then are post-heated. However, the use of electrodeposited ZnS in thin-film solar cells has received little attention. Dharmadasa et al. demonstrated superstrate CdTe solar cells with efficiencies greater than 10% by using electrodeposited ZnS in the device fabrication. For example, because of its wide bandgap, the inclusion of electrodeposited ZnS in 3-layered graded-bandgap CdTe solar cells (Au/CdTe/CdS/ZnS/FTO/glass) improved the J_{sc} and is more efficient than the 2-layered configuration (Au/CdTe/CdS/FTO/glass) (49).

2.4 Electrodeposition of ZnO/Al:ZnO Transparent Conducting Oxides

Several reports on the electrodeposition of ZnO and metal doped ZnO thin films are available. However, their application in solar cells will be discussed in this section. Rousset et al demonstrated a 14.7 % Cd-free CIGSe solar cell with an In_2S_3 buffer layer grown by atomic layer deposition and terminated with electrodeposited front contact ZnO:Cl (Mo/CIGSe/In_2S_3/ZnO:Cl). The work proposes anionic doping of ZnO with $ZnCl_2$, KCl, and oxygen gas deposited at 80 °C

using a three-electrode system and then annealed at 150 °C to obtain the desired electrical properties (61). Mkawi et al. reported a 2.3 % Cd-free CZTS solar cell using CBD-ZnS as a buffer layer and pulse electrodeposited Al:ZnO as the TCO, finally with an Al contact (glass/Mo/Cu_2ZnSnS_4/ZnS/ZnO/Al grid) (62). Another relevant study by Haller et al. replaced conventional TiO_2 with electrodeposited nano porous ZnO for dye sensitized solar cells (DSSCs) and achieved 4.5 % efficiency (63). The conventional 3-electrode system with $ZnCl_2$, KCl, and sodium salt of Eosin Y as structure directing agents was used in this study, and it was deposited with saturated oxygen gas at 75 °C. Kouhestanian et al. recently used electrodeposited ZnO as a blocking layer for the TiO_2 based DSSC. At 70 °C, this group deposited ZnO from an electrolyte containing $ZnCl_2$, KCl, and poly vinyl acetate (PVA) and was saturated with oxygen gas. According to the findings, PVA interacts with Zn^{2+} to form mixed ZnO crystals embedded in the polymer matrix, which acts as a capping agent and prevents excessive growth. They observed a significant increase in the J_{sc} with an efficiency of 5.0 % due to an improvement in electron transfer while reducing recombination caused by the presence of a blocking layer (64).

The majority of research in this field has used zinc nitrates or zinc chlorides as zinc precursors. In any case, deposition is frequently performed in aqueous electrolytes at elevated temperatures (60-80 °C) using nitrate salts as an oxygen precursor (65). It is also critical to obtain crystalline quality thin films, so deposition is frequently performed at high temperatures, which increases the rate of reaction. However, the investigation of non-aqueous electrolytes such as dimethyl sulfoxide (DMSO) is only limited to ZnO thin films where deposition temperatures ranged from 90 to 140 °C and yielded hexagonal ZnO films with larger crystal size (66).

2.5 Fabrication of All Non-Vacuum-based CIGS Solar Cells

Commercially, CIGS thin film solar cells are made with polycrystalline CIGS absorber layers that are widely fabricated using a vacuum-based process that combines co-evaporation or co-sputtering copper, indium, and gallium, followed by thermal treatment in the presence of selenium vapor to form CIGS. As a result, the fabrication cost is high, which raises the price of modules. Thus, research is now shifting toward non-vacuum processing technologies such as electrodeposition (ED), chemical bath deposition (CBD), spray pyrolysis, and spin coating, which reduce manufacturing costs. Among these, electrodeposition is widely used and commercialized module level 60 × 120 cm^2 to the point where NEXCIS group achieved the latest efficiency of

17.3 % (67) who optimized absorber layer CIGS that is electrodeposited on Mo/glass. On the other hand, subsequent buffers and TCO layers, such as CdS and ZnO, are deposited by CBD and sputtering, which affects device cost. In addition to sputtering, CBD and spin coating have also been reported as non-vacuum-based methods of TCO layer synthesis. The final device, however, has a silver contact or metal grid on its top. Thus, the current research involves non-vacuum techniques to produce device-quality films, such as electrodeposition.

In the photovoltaics community, non-vacuum solution processing of inorganic thin films is an important aspect. This is because non-vacuum-based techniques are low-cost and have a high throughput. CIGS solar cells are fabricated using solution processes for layers such as CdS and CIGS using different non-vacuum techniques. The importance of the CIGS layer in the device structure may be the reason for the interest in research on it over other layers. It is the device's heart and is approximately 2 microns thick, whereas CdS, ZnO, and AZO are approximately 100 nm and 500-600 nm, respectively. As a result, extensive research and development has focused on the CIGS absorber, which, when produced through a solution process, can significantly reduce device cost. Scores of researchers have reported on the fabrication of all non-vacuum-based CIGS solar cells in the last few years, where different layers are fabricated using various solution processing techniques to produce a complete non-vacuum based solar cell. Prathap et al. reported the fabrication of a novel device using all spray coated layers with a device configuration of glass/Mo/CIGS/ZnMgO/ZnO:Ga/Cu-Au. This preliminary study demonstrated a device efficiency of about 3.9 % when conventional CdS was replaced with ZnMgO and AZO using ZnO:Ga (68). Manjeet et al. investigated the spin coating process for depositing all of the layers of a CIGS solar cell. The device is built on the structure glass/Mo/CIGS/CdS/ZnO/(AgNW/ZnO) where AZO is replaced with ZnO incorporated with silver nanowires AgNWs. This low-cost, solution-processed device had a 1.6 % efficiency for a 0.1 cm^2 area (69). Wang and Choy investigated spray coated AgNWs/AZO transparent thin electrodes in comparison to conventional electrodeposited CIGS, CBD processed CdS, and spray coated ZnO/AgNWs AZO. The best performance of this device demonstrated a conversion efficiency of about 14 %, which is comparable to the 14.4 % achieved by a device made from a conventional sputtered TCO layer with an area of 0.1 cm^2 (70). Romanyuk et al. demonstrated a promising solution processing approach in which the CIGS absorber is electrodeposited, CdS and AZO are deposited using chemical bath deposition, and i-ZnO is spin coated. The device was mechanically scribed into

0.1cm^2 individual cells with the device structure glass/Mo/CIGS/CdS/ZnO/AZO and demonstrated a 13.8 % efficiency (71). Fabien et al. reported a device with an electrodeposited ZnO:Cl layer in place of the traditional sputtered AZO layer. Electrodeposited CIGS, chemical bath deposited CdS, and then electrodeposited ZnO:Cl were used in the device fabrication, with the device structure being glass/Mo/CIGS/CdS/ZnO:Cl/Ni-Al and finally scribed into individual cells of about 0.5cm^2. This device had a 14.3 % efficiency, which was comparable to the 14.8 % efficiency of the sputtered i-ZnO/AZO device (72). Kemell et al. attempted the first all-electrodeposited CISe solar cell without a CdS buffer layer, instead employing In and Al doped ZnO as TCO layers with an Al contact. This group thoroughly investigated the diode characteristics of various configurations and discovered that In:ZnO (Mo/CISe/i:ZnO/In:ZnO/Al grid) exhibits significantly better rectifying behavior (73). They found appreciable diode behavior in the dark conditions while no response under illumination. Therefore, it is important to note that attempts fabricate CIGS solar cell with electrodeposited CIGS is limited and has enough gap for research on electrodeposition of buffer layers such as CdS and ZnS.

2.6 Aim and Objectives of the Research

A systematic review of all available reports on all-solution CIGS device processing till date demonstrates that devices generated from electrodeposited CIGS absorbers have the highest efficiencies compared to alternative non-vacuum processes, even on flexible substrates. Scalability, minimal energy usage, and effective utilization of raw materials are the advantages of electrodeposition over other methods. As a result, the current research focuses on the electrodeposition technique, which is the most well-established method for producing different layers such as CIGS, CdS, ZnS, ZnO, and Al:ZnO films. Low-cost industrial manufacturing with a high deposition rate and material utilization emerges with the use of a single deposition technique. As a result, a solar cell consisting solely of electrodeposited layers needs a single production line with a lower capital cost. The conventional CBD technique for CdS is as well studied in this investigation and compared the structural and optical properties of the CdS made from both CBD and electrodeposition.

The primary goal of this study is to create CIGS solar cells using thin films created by electrodeposition. This can be accomplished by pursuing goals.

i. To prepare single phase CIGS absorber layer with a high crystallinity. A detailed investigation and overview of material properties is discussed in chapter 4. It also projected the feasibility to produce large area CIGS absorber by different modes of electrodeposition.

ii. To replace the conventional CBD-CdS layer in solar cell fabrication with an electrodeposited CdS layer. Electrodeposition of CdS is explored and developed at room temperature by varying and applying pulse variables of the electrodeposition process (chapter5). The use of organic acid such as tartaric acid is explored that facilitated the formation of crystalline CdS without a post annealing treatment. Further relevant studies are discussed in later part of chapter 5 including the growth mechanism and CIGS device fabrication using pulse electrodeposited CdS as buffer layer

iii. To produce a non-toxic ZnS layer for the fabrication of Cd-free CIGS solar cells. The use of tartaric acid and glycerol is well studied and described in chapter 5 while varying the deposition parameters. The consequences of growth mechanism of films prepared in the presence of tartaric acid is explored and compared with those of without tartaric acid. Further, the relevance of ZnS for the cell performance is discussed in chapter 5

iv. To introduce ZnO and Al:ZnO layers deposited using an electrodeposition technique. The development of AZO films is described in chapter 6. The details include the optimization of Al foil insertion which is the novel approach used for the Al doping. The effect of annealing is studied at various temperatures and examined their dependence on the structural features and morphological aspects.

v. Fabrication of an all-electrodeposited CIGS solar cell. Based on the presented experiments in the chapter 4,5 and 6, the possibility of preparing an all-electrodeposited CIGS solar cell is explored in chapter 7.

References

1. P. Jackson, D. Hariskos, R. Wuerz, O. Kiowski, A. Bauer, T. M. Friedlmeier and M. Powalla, *physica status solidi (RRL) - Rapid Research Letters*, **9**, 28 (2015).
2. P. Jackson, R. Wuerz, D. Hariskos, E. Lotter, W. Witte and M. Powalla, *physica status solidi (RRL) - Rapid Research Letters*, **10**, 583 (2016).
3. T. Kato, J. Wu, Y. Hirai, H. Sugimoto and V. Bermudez, *IEEE Journal of Photovoltaics*, **9**, 325 (2019).
4. K. Y. Motoshi Nakamura , Yoshinori Kimoto, Yusuke Yasaki, Takuya Kato , and Hiroki Sugimoto, *IEEE JOURNAL OF PHOTOVOLTAICS*, **9**, 1863 (2019).
5. H. W. R. N. Bhattacharya, T. A. Berens, R. J. Matson, J. Keane, K. Ramanathan, A. Swartzlander, A. Mason, and R. N. Noufi*, *J. Electrochem. Soc*, **144**, 1376 (1997).
6. R. N. Bhattacharya, *Solar Energy Materials and Solar Cells*, **113**, 96 (2013).
7. A. Shanmugavel, K. Srinivasan and K. R. Murali, *Journal of Materials Science: Materials in Electronics*, **24**, 2398 (2013).
8. C. V. C. Broussillou, A. Rogee, S. Angle, P.P. Grand, S. Bodnar, C. Debauche, J.L. Allary, B. Bertrand, C. Guillou, L. Parissi, S. Coletti,, *IEEE* (2015).
9. Q. Gao, J. Ao, J. Bi, L. Yao, Z. Zhang, Y. Zhang, J. Guo, G. Sun, Y. Zhang, W. Liu and F. Liu, *ACS applied materials & interfaces*, **12**, 24403 (2020).
10. A. S. A. N. Mammadov, and M. Elrouby, *International Journal of Thin Films Science and Technology*, **1**, 43 (2012).
11. S. Hariech, M. S. Aida, J. Bougdira, M. Belmahi, G. Medjahdi, D. Genève, N. Attaf and H. Rinnert, *Journal of Semiconductors*, **39** (2018).
12. A. Pareek, R. Dom and P. H. Borse, *International Journal of Hydrogen Energy*, **38**, 36 (2013).
13. H. Tao, Z. Jin, W. Wang, J. Yang and Z. Hong, *Materials Letters*, **65**, 1340 (2011).
14. M. Cao, Y. Sun, J. Wu, X. Chen and N. Dai, *Journal of Alloys and Compounds*, **508**, 297 (2010).
15. A. A. Ojo and I. M. Dharmadasa, *Materials Chemistry and Physics*, **180**, 14 (2016).
16. S. B. Patil and A. K. Singh, *Applied Surface Science*, **256**, 2884 (2010).
17. D. M. Figen Kadirgan, Wenjie song, Tim ohno,Brian Mccandless, *Turkey Journal of Chemistry*, **24**, 21 (2000).
18. K. Premaratne, S. N. Akuranthilaka, I. M. Dharmadasa and A. P. Samantilleka, *Renewable Energy*, **29**, 549 (2004).
19. M.-C. Chen, J.-C. Sung, C.-Y. Ou, S. Som and C.-H. Lu, *Thin Solid Films*, **645**, 64 (2018).
20. A. H. Barry Miller, *Nature*, **260**, 312 (1976).
21. N. D. Sankir and B. Dogan, *Journal of Materials Processing Technology*, **211**, 382 (2011).
22. N. A. Abdul-Manaf, A. Weerasinghe, O. Echendu and I. Dharmadasa, *Journal of Materials Science Materials in Electronics*, **26**, 2418 (2015).
23. A. W. Gavin.J.covineer, *Solar Cell Materials Developing Technologies*, UK (2014).
24. H. I. Salim, O. I. Olusola, A. A. Ojo, K. A. Urasov, M. B. Dergacheva and I. M. Dharmadasa, *Journal of Materials Science: Materials in Electronics*, **27**, 6786 (2016).
25. S. C. Junichi Nishino, Yukifumi Uotani, Yoshio Nosaka, *Journal of Electroanalytical Chemistry*, **473**, 217 (1999).
26. H. Y. R. Atapattu, S. De Silva, K. A. S. Pathiratne, O. Olusola and I. Dharmadasa, *Journal of Materials Science: Materials in Electronics*, **28**, 18592 (2017).

27. S. K. Shinde, G. S. Ghodake, N. B. Velhal, M. V. Takale, D. Y. Kim, M. C. Rath, H. D. Dhaygude and V. J. Fulari, *Journal of Solid State Electrochemistry*, **21**, 1517 (2016).
28. S. Mandati, B. V. Sarada, S. R. Dey and S. V. Joshi, (2018).
29. S. Mandati, B. V. Sarada, S. R. Dey and S. V. Joshi, *Journal of Renewable and Sustainable Energy*, **5**, 031602 (2013).
30. D. Gal, G. Hodes, D. Hariskos, D. Braunger and H.-W. Schock, *Applied Physics Letters*, **73**, 3135 (1998).
31. J.-Y. L. Xiao-Yun Yu, Kang-Qiang Qiu, Dai-Bin Kuang,* and Cheng-Yong Su, *ACS Nano*, **5**, 9494 (2011).
32. Ü. Özgür, Y. I. Alivov, C. Liu, A. Teke, M. A. Reshchikov, S. Doğan, V. Avrutin, S. J. Cho and H. Morkoç, *Journal of Applied Physics*, **98** (2005).
33. M. Hermann, D. Gogova, D. Siche, M. Schmidbauer, B. Monemar, M. Stutzmann and M. Eickhoff, *Journal of Crystal Growth*, **293**, 462 (2006).
34. D. Gogova, H. Larsson, A. Kasic, G. R. Yazdi, I. Ivanov, R. Yakimova, B. Monemar, E. Aujol, E. Frayssinet, J.-P. Faurie, B. Beaumont and P. Gibart, *Japanese Journal of Applied Physics*, **44**, 1181 (2005).
35. P. H. Borse, W. Vogel and S. K. Kulkarni, *J Colloid Interface Sci*, **293**, 437 (2006).
36. X. Fang, T. Zhai, U. K. Gautam, L. Li, L. Wu, Y. Bando and D. Golberg, *Progress in Materials Science*, **56**, 175 (2011).
37. B. Divya, S. Harish, K. Ramaswamy, M. Kishorebabu, N. Raju, R. Govindaiah, U. Rambabu and N. R. Munirathnam, *International Journal of Environmental Science and Technology*, **14**, 2603 (2017).
38. A. Zyoud, S. Al-Yamani, H. Bsharat, M. H. Helal, H. Kwon, D. Park and H. S. Hilal, *Materials Science in Semiconductor Processing*, **74**, 277 (2018).
39. S. Siebentritt, *Solar Energy*, **77**, 767 (2004).
40. T. Nakada and M. Mizutani, *Japanese Journal of Applied Physics*, **41**, L165 (2002).
41. S. M. A. a. S. J. Piercey, Current Perspectives on Zinc Deposits, in, G. S. o. Ireland Editor, Irish Association for Economic Geology, Ireland (2015).
42. B.-R. K. Won Song, Seok Eui Choi, Yong-Taeg Oh, and Dong-Chan Shin, *International Journal of Materials and Metallurgical Engineering*, **6** (2012).
43. M. Izi, G. Heidari, S. M. Mousavi Khoie and J. Najafi, *Surface Engineering and Applied Electrochemistry*, **53**, 245 (2017).
44. H. S. Kim, G. Kim, E. Kim, S. J. Cho, D. J. Lee, S. G. Choi, F. Shan and S. J. Kim, *Journal of nanoscience and nanotechnology*, **19**, 1799 (2019).
45. T. T. Ngoc Van, A. S. Ansari and B. Shong, *Journal of Vacuum Science & Technology A*, **37**, 020909 (2019).
46. N. A. Abdul-Manaf, A. R. Weerasinghe, O. K. Echendu and I. M. Dharmadasa, *Journal of Materials Science: Materials in Electronics*, **26**, 2418 (2015).
47. M. L. Madugu, O. I.-O. Olusola, O. K. Echendu, B. Kadem and I. M. Dharmadasa, *Journal of Electronic Materials*, **45**, 2710 (2016).
48. S. H. Mohamed, M. El-Hagary and M. Emam-Ismail, *Journal of Physics D: Applied Physics*, **43** (2010).
49. O. D. Echendu, Imyhamy, *Energies*, **8**, 4416 (2015).
50. M. Jafarov, E. Nasirov, S. A. Jahangirova and R. Jafarli, in (2015).
51. B. W. Sanders, *Journal of Crystal Growth*, **100**, 405 (1990).
52. K. R. Murali, *IOSR Journal of Applied Physics*, **6**, 9 (2014).

53. R. Bengas, H. Lahmar, K. M. Redha, L. Mentar, A. Azizi, G. Schmerber and A. Dinia, *RSC Advances*, **9**, 29056 (2019).
54. H. M. M. N. Hennayaka and H. S. Lee, *Thin Solid Films*, **548**, 86 (2013).
55. A. A. Ojo, *Materials Research Express*, **6**, 086465 (2019).
56. N. O. Naohiro Matsuda, and Takeyasu Saito, in *ICEP-IAAC 2018 Proceedings*, Kuwana, Mie, Japan (2018).
57. O. K. Echendu, A. R. Weerasinghe, D. G. Diso, F. Fauzi and I. M. Dharmadasa, *Journal of Electronic Materials*, **42**, 692 (2013).
58. N. Fathy and M. Ichimura, *Solar Energy Materials and Solar Cells*, **87**, 747 (2005).
59. M. A. Contreras, T. Nakada, M. Hongo, A. O. Pudov and J. R. Sites, in *3rd World Conference onPhotovoltaic Energy Conversion, 2003. Proceedings of*, p. 570, Japan (2003).
60. V. Hernández-Calderón, O. Vigil-Galán, M. Guc, A. Carrillo-Osuna, S. Ramírez-Velasco, F. J. Sánchez-Rodríguez, P. Vidal-Fuentes, S. Giraldo, E. Saucedo and Y. Sánchez, *ACS Applied Energy Materials*, **3**, 6815 (2020).
61. J. Rousset, E. Saucedo, K. Herz and D. Lincot, *Progress in Photovoltaics: Research and Applications*, **19**, 537 (2011).
62. E. M. Mkawi, K. Ibrahim, M. K. M. Ali, M. A. Farrukh and A. S. Mohamed, *Applied Nanoscience*, **5**, 993 (2015).
63. S. Haller, J. Rousset, G. Renou and D. Lincot, *EPJ Photovoltaics*, **2**, 20401 (2010).
64. E. Kouhestanian, S. A. Mozaffari, M. Ranjbar, H. SalarAmoli and M. H. Armanmehr, *Superlattices and Microstructures*, **96**, 82 (2016).
65. K. D. Arun Kumar, S. Valanarasu, V. Ganesh, M. Shkir, S. AlFaify and H. Algarni, *Journal of Materials Research*, **33**, 1523 (2018).
66. A. Tello, H. Gómez, E. Muñoz, G. Riveros, C. J. Pereyra, E. A. Dalchiele and R. E. Marotti, *Journal of The Electrochemical Society*, **159**, D750 (2012).
67. C. V. c. Broussillou, A. Rogee, S. Angle, P.P. Grand, S. Bodnar, C. Debauche, J.L. Allary, B. and C. G. Bertrand, L. Parissi, S. Coletti,, *IEEE* (2015).
68. P. Prathap, A. Suryanarayana Reddy, G. Ramachandra Reddy, R. W. Miles and K. T. Ramakrishna Reddy, *Solar Energy Materials and Solar Cells*, **94**, 1434 (2010).
69. M. Singh, J. Jiu, T. Sugahara and K. Suganuma, *ACS applied materials & interfaces*, **6**, 16297 (2014).
70. M. Wang and K. L. Choy, *ACS Appl Mater Interfaces*, **8**, 16640 (2016).
71. Y. E. Romanyuk, H. Hagendorfer, P. Stücheli, P. Fuchs, A. R. Uhl, C. M. Sutter-Fella, M. Werner, S. Haass, J. Stückelberger, C. Broussillou, P.-P. Grand, V. Bermudez and A. N. Tiwari, *Advanced Functional Materials*, **25**, 12 (2015).
72. F. Tsin, A. Venerosy, J. Vidal, S. Collin, J. Clatot, L. Lombez, M. Paire, S. Borensztajn, C. Broussillou, P. P. Grand, S. Jaime, D. Lincot and J. Rousset, *Scientific Reports*, **5**, 1 (2015).
73. M. Kemell, F. Dartigues, M. Ritala and M. Leskelä, *Thin Solid Films*, **434**, 20 (2003).

CHAPTER 3

EXPERIMENTAL METHODOLOGY AND GENERAL CHARACTERIZATION TECHNIQUES FOR THE EVALUATION OF ELECTROPOSITED THIN FILMS

CHAPTER 3
EXPERIMENTAL METHODOLOGY AND GENERAL CHARACTERIZATION TECHNIQUES FOR THE EVALUATION OF ELECTRODEPOSITED THIN FILMS

In this chapter, the different methods and setups used for depositing CIGS, CdS, ZnS, ZnO and Al: ZnO will be discussed. All these different materials are fabricated used electrodeposition technique. The various electrolytes and modified experimental conditions will be discussed.

3.1 PART A: Experimental Methods

Thin film electrodeposition requires several steps prior to deposition, including substrate preparation, electrolyte preparation, and deposition.

3.1.1 Substrate Preparation

Glass/FTO (Sigma Aldrich, 7 Ωsq^{-1}) substrates are used for both the buffer layers such as CdS and ZnS thin film depositions. The absorbers CISe and CIGSe thin films are deposited on inhouse made Mo sputtered SLG glass substrates (1). Depending on the application, the substrates are cut into 3×3 cm^2 for FTO and 7.5 × 2.5 cm^2 and 2.5 × 2.5 cm^2 for Mo/glass, respectively. In all cases, the substrates are cleaned ultrasonically for about 10 minutes in a soap solution made from Labolene liquid. They are then rinsed in de-ionized (DI) water for 10 minutes before being washed with acetone (C_3H_6O, SRL extra pure 99.5 %) and ethanol (C_2H_5OH, Changshu Hongsheng Fine Chemical Co.Ltd, AR grade 99.9 %).The working electrodes are cleaned substrates, and the counter electrode is high purity graphite. These substrates are masked partially with kapton tape before deposition to achieve a step difference between the bare and coated areas.

3.1.2 Electrolyte Preparation

Both aqueous and non-aqueous electrolytes are used in this study for electrodeposition of the different layers including methanol, water and DMSO. Non-aqueous solvents such as methanol and dimethyl sulfoxide (DMSO) are used for copper and gallium, & ZnO and AZO films respectively. CdS, ZnS, and Indium, thin films are however, deposited in an aqueous electrolyte. The resistivity of the DI water used for electrolyte preparation is approximately 18Ω. The chemicals used are of the highest quality (99.99 %).

3.1.3 Electrodeposition

CV or LSV experiments are performed prior to any thin film deposition to study the redox reactions, and a range of voltages are applied accordingly for the electrodeposition. All electrodepositions are carried out using a two-electrode system, which has advantages over the traditional three-electrode system, such as ease of deposition and elimination of potential contaminants from the reference electrode. The depositions are carried out with a Dynatronix (DuPR-10-3-6) pulse power supply at ambient temperature for CIGS, CdS, and ZnS, and at high temperatures for ZnO and AZO.

3.2 Theory of Electrodeposition

Electrodeposition of thin films is the most effective approach for the PV industry. The main benefits are scalability, cost-effectiveness, and an environmentally friendly processing. A bath containing a metal ion-based electrolyte, a conducting substrate (cathode) on which the deposition occurs. A counter electrode (anode), and a reference electrode are generally used for a 3-electrode system while it omits reference in the 2-electrode system. Electrochemical reactions occur when a suitable potential is applied between these electrodes, and metal ions are reduced onto the cathode to deposit and form thin films. Electrodeposition is mainly done by two deposition approaches: two-electrode system and three-electrode system. The traditional three-electrode system includes anode, cathode, and reference electrodes. Standard Hydrogen Electrode (SHE), Saturated Calomel Electrode (SCE), and Ag/AgCl electrodes are the most commonly used references electrodes. In general, a reference electrode is used to measure the potential across the working electrode interface in relation to the third electrode. The two-electrode system, on the other hand, does not use a reference electrode. Using a two-electrode system is advantageous because it prevents Na^+ and K^+ ions diffusing from the reference electrode to the electrodeposited thin film material (2, 3).

For spontaneous reaction during electrodeposition, $\Delta G < 0$, where ΔG is the Gibbs free energy of formation. Thermodynamically, it is defined as the chemical potential that is minimized when a system reaches equilibrium at constant pressure and temperature. This can be related to the activity of the species present in the electrolyte or electrical cell potential as follows (4)

$$\Delta G = \Delta G^o + RT \ln\left(\frac{a_M}{a_{M^{z+}}}\right) \tag{3.1}$$

Where ΔG^o is the standard Gibbs free energy of the metal reduction reaction, R is the universal gas constant, T is the absolute temperature, a_M is the activity of the element, $a_{M^{2+}}$ is the activity of the elemental species. The activity of an element is usually 1 and in dilute solutions with no complexation therefore equation (3.1) becomes

$$\Delta G = \Delta G^o + RT \ln\left(\frac{1}{[M^{z+}]}\right) \quad (3.2)$$

ΔG is also related to electric potential:

$$\Delta G = -n F E \quad (3.3)$$

Where n is the number of moles of electrons involved, F is Faraday's constant and E is the electric potential. On substitution of equation (3.2) to equation (3.3), it gives the Nernst equation relating electric potential E, to the concentration of elemental species $[M^{z+}]$:

$$E = E^o - \frac{RT}{nF} \ln\left[\frac{1}{M^{z+}}\right] \quad (3.4)$$

From this equation, E^o is the standard electrode potential, E is the deposition potential that can be regulated by adjusting the concentration of the species at specific temperature.

Metal ion electrodeposition from liquid phase to solid thin film necessitates transformation. This transformation process involves nucleation and growth mechanism. Ionic transport, diffusion of metal ions towards the electrode, ligation of solvated metal ions, and then formation of ad atoms and nuclei all occur prior to the nucleation step, favoring the growth process (5).

3.2.1 Nucleation and Growth

The growth of semiconductors is influenced by substrate morphology, and the majority of substrates are polycrystalline in nature with ideal grain boundaries that are not smooth. The first step in nucleation is surface diffusion of ions, which discharge and desolvate before attaching to the surface of the electrode to form an ad atom. These ad atoms reach favorable kink sites and continue to grow with another ad atom until a monolayer is formed. This can occur as clusters of critical nuclei and provides kinks and steps that act as nucleation sites for the subsequent ad atoms. Nucleation occurs in two stages: progressive nucleation and instantaneous nucleation. The formation of nuclei occurs concurrently with growth and time in a progressive nucleation, as shown in **Figure 3.1**. The rate of nucleation is much faster than the rate of new site propagation.

The nucleation rate is slower than the rate of nuclei formation in the case of instantaneous nucleation. The nuclei form and grow quickly, forming a monolayer. Several mathematical models are used to investigate this mechanism, including Scharifker-Hills model (6), Scharifker-Mostany model(7), Heerman-Tarallo model(8), Sluyters-Rehbach model(9) and Mirkin-Nilov model(10). In the case of diffusion –controlled reactions, the Scharifker-Hills model is the most widely used.

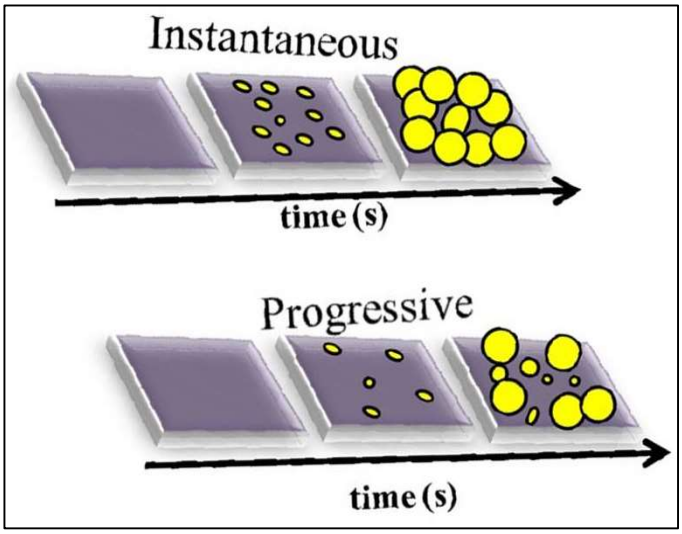

Figure 3.1: Schematic representation of instantaneous and progressive nucleation

Factors affecting the electrodeposition of binary, ternary and quaternary compounds include

- The reduction potentials of the different elements in the electrolyte
- Concentration of metal ions in the electrolyte
- Cathodic polarization due to differences in deposition potentials

Aside from these, the deposition is influenced by the deposition parameters such direct current electrodeposition, pulse electrodeposition, temperature, and pH.

3.2.2 Direct Current Electrodeposition

As shown in **Figure 3.2**, in direct current deposition, the plating unit is connected to DC power, and electrons from the circuit are supplied continuously without interruption. The only parameter that can be changed in this deposition is the current density. During deposition, the off-time is set to zero, indicating a 100 % duty cycle. As a result, the average current density in this deposition equals the peak current density.

3.2.3 Pulse Current Electrodeposition

In the case of pulse current deposition, the current is applied constantly with a relaxation time that produces rectangular pulses and aids in the control of electrocrystallization as shown in **Figure 3.2**. A number of independent variables such as pulse on, and pulse off time, current density, frequency, and so on, can be changed. When compared to DC deposition, this variation favors the optimization of films that can be uniform and compact. Besides, during the pulse condition, high current densities are observed, which could be due to the accumulation of metal ions near the electrode during the relaxation time, increasing the concentration of metal ions for deposition.(11).

$$\text{Duty cycle (\%)} = \frac{T_{on}}{T_{on}+T_{off}} \tag{3.5}$$

$$\text{Frequency} = \frac{1}{T_{on}+T_{off}} \tag{3.6}$$

3.2.4 Pulse Reverse Electrodeposition

Similarly, another approach is to use pulse reverse electrodeposition, in which an anodic pulse current/potential is applied to remove excess metal deposited or impurities, leading to the formation of high-quality thin films, as shown in **Figure 3.2**. This periodic switching of anodic and cathodic pulses aids in the removal of impurities, resulting in higher quality materials.

$$\text{Duty cycle (\%)} = \frac{T_C}{T_{AA}+T_C} \tag{3.7}$$

where Tc is the cathodic (forward) time, TAA is anodic (reverse) time.

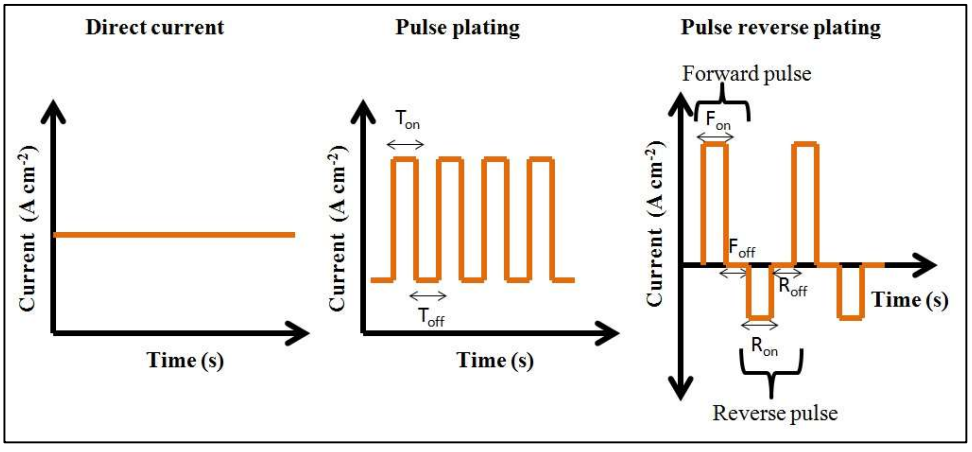

Figure 3.2: Schematic of direct current, pulse and pulse reverse electrodeposition

3.3 PART B: Electrodeposition of Semiconductor Thin Films by Modified Electrolytes

3.3.1 Electrolyte for Deposition of CIGS Layer

Cu, In, and Ga are sequentially deposited from three different electrolytes, and the films are finally selenized in an inert atmosphere using rapid thermal processing (RTP) to obtain large grains for device fabrication. In the case of copper deposition, the electrolyte is 44 mM $CuCl_2.5H_2O$, 170 mM sodium dodecyl sulphate ($NaC_{12}H_{25}SO_4$), 250 mM LiCl dissolved in 100 ml methanol based non-aqueous solvent, and the final pH is adjusted to 1.0 using dilute HCl. Aqueous electrolyte containing 45 mM $InCl_3$, 170 mM sodium dodecyl sulphate (SDS) ($NaC_{12}H_{25}SO_4$), and 250 mM LiCl dissolved in 100 ml DI water as electrolyte is used for indium deposition. The individual gallium electrolyte is then prepared by dissolving 11 mM $GaCl_3$, 170 mM sodium dodecyl sulphate ($NaC_{12}H_{25}SO_4$), and 250 mM LiCl in 100 ml of methanol based non-aqueous electrolyte. Using dilute HCl, the pH of the indium and gallium solutions is adjusted to 2.0.

$$Cu^{2+} + 2e^- \leftrightarrow Cu_{(s)} \qquad E^0 = +0.34\,V\ vs\ SHE \qquad (3.8)$$

$$In^{3+} + 3e^- \leftrightarrow In_{(s)} \qquad E^0 = -0.34\,V\ vs\ SHE \qquad (3.9)$$

$$Ga^{3+} + 3e^- \leftrightarrow Ga_{(s)} \qquad E^0 = -0.55\,V\ vs\ SHE \qquad (3.10)$$

$$HSeO_2^+ + 4H^+ + 4e^- + OH^- \leftrightarrow H_2SeO_3 + 4H^+ + 4e^- \rightarrow Se + 3H_2O\ E^0 = +0.74\,V\ vs\ SHE \qquad (3.11)$$

$$Cu^{2+} + In^{3+} + 2SeO_3^{2-} + 9e^- + 12H^+ \rightarrow CuInSe_2 + 6H_2O \qquad (3.12)$$

$$Cu^{2+} + In^{3+} + Ga^{3+} + 2SeO_3^{2-} + 12e^- + 12H^+ \rightarrow CuInGaSe_2 + 6H_2O \qquad (3.13)$$

3.3.2 Electrolyte for CdS Deposition

A two-electrode system is used for pulse electrodeposition of CdS. The electrolyte is made by dissolving 2 mM $CdSO_4$ (Alfa Aesar, 99 % purity) and 158 mM $Na_2S_2O_3$ (Fisher Scientific, 99 % purity) in 100 ml DI water and adjusting the pH to 2.5 with 1M Tartaric acid. The deposition takes place at room temperature.

3.3.3 Electrolyte for ZnS Deposition

An electrolyte containing 700 mM zinc sulphate heptahydrate ($ZnSO_4.7H_2O$, 99 %, SRL) sodium thiosulphate anhydrous ($Na_2S_2O_3$ extra pure SRL AR grade, 99.5 %) glycerol ($C_3H_8O_3$,

anhydrous SRL extra pure 99 %) dissolved in 100 ml DI water is used for pulse electrodeposition of ZnS. 1 M Tartaric acid ($C_4H_6O_6$, Fisher Scientific (+) 99 %) is used to adjust the final pH to 2.2.

3.3.4 Electrolyte for ZnO and Al:ZnO Depositions

Zinc chloride (SRL, anhydrous, 99.9 %), lithium chloride (SRL, anhydrous, 99.9 %), dimethyl sulfoxide (DMSO, Fisher scientific, SQ grade 99.7 %), aluminum foil (domestic, 0.016 mm thick), were procured and used without further purification.

Potentiostatic pulse electrodeposition of Al: ZnO was performed in DMSO electrolyte containing 0.01 M $ZnCl_2$ and 0.015 M LiCl at a potential of – 3.0 V with a 25% duty cycle. Depositions were carried out with Dynatronix pulse power supply at a temperature of 90 °C. Inserting an Al foil into the electrolyte and bubbling oxygen gas throughout the experiment was used to incorporate Al. The pH of the electrolyte was kept at 7.0, and the AZO films were deposited using a simple two-electrode system with FTO/glass as the working electrode and high purity graphite plate as the counter electrode. Prior to deposition, the FTO/glass was cleaned for 10 minutes each with soap solution, acetone, ethanol, and de-ionized (DI) water, followed by drying in N_2gas. The electrodeposited AZO films were then rinsed with DI water, dried with N_2 gas, and annealed in air at 300 °C. Al doping is carried out using Al metal foil which is used for the first time in the electrodeposition process. The insertion temperature of Al foil is vital to obtain precise doping concentration of the metal into the ZnO films. Therefore, its optimization is carried out at different temperatures and examined for EDS and structural aspects confirming the formation of AZO.

3.4 PART C: Instrumentation and Characterization

This section describes various tools and techniques for characterizing and evaluating the properties of electrodeposited thin films. The thin films are examined using a variety of advanced analytical techniques. Characterization is essential for understanding the properties of materials and, as a result, aids in their development with novel properties. Thin films are generally distinguished by their composition, morphology, and structure elucidation, as well as their optical and electrical properties. This section discusses all of the techniques used to characterize the properties listed above.

Various techniques involved in the characterization of thin films

Electrochemical analysis

Scanning Electron Microscopy (SEM)

X-Ray Diffraction (XRD)

Raman Spectroscopy

UV-VIS-NIR spectroscopy

Stylus Profilometry

I-V measurements

3.4.1 Techniques for Characterization

3.4.1.1 *Electrochemical Analysis*

The electrochemical work station is used for electrochemical studies such as Cyclic Voltammetry (CV), Linear Sweep Voltammetry (LSV), Electrochemical Impedance Spectroscopy (EIS), Photoelectrochemical Characterization (PEC), and Mott-Schottky analysis (MS). All of these experiments are carried out with a three-electrode system that includes a counter electrode of high purity graphite, a bare substrate in the case of CV and LSV, a deposited film in the case of EIS, PEC, and MS as working electrodes, and a saturated calomel electrode (SCE) as a reference electrode. To investigate the redox potentials of the deposited elements, CV and LSV are performed.

In CV measurements, at a constant scan rate the voltage applied oscillates between two different voltages V1 and V2. The current response is plotted as current vs voltage, revealing both oxidation and reduction reactions of the electrolyte under consideration. The increase in the current peak in the positive potentials corresponds to oxidation, while the decrease in the negative potentials corresponds to reduction. LSV provides information on only the reduction reactions taking place in the solution, allowing one to study and identify the reduction potentials of the elements of interest.(12).

Figure 3.3: Electrochemical analyzer (Parstat 4000A)

EIS studies are commonly used to assess the electrical properties of thin films. In the current study, for example, all of the thin films electrodeposited are tested for resistance behavior, and EIS plays an important role. It provides information on the resistance between the electrode and the electrolyte, which is equivalent to the series resistance, as well as the transport properties within the coating, which elaborates the recombination paths of the film and is important for solar cell applications (13). Another important method for understanding the light absorption property of a thin film in the presence of artificial incident light that is equivalent to sunlight energy is photoelectrochemical characterization (PEC) (AM 1.5G). When two semiconducting materials are brought together in a solid-state device, a *pn* junction is formed. In contrast, the interface between the semiconductor and the electrolyte in a PEC cell acts as a *pn* junction. Its photo response is determined by the current in relation to the applied voltage in both dark and light conditions (14). In this manner, the desired properties of thin films can be evaluated prior to the fabrication of a full solid-state device. Mott-Schottky analysis (MS) is a method for interpreting the semiconductor's electrical conductivity, flat band potential equation (3.5), carrier density (equation3.6) and band edges (equation 3.7,3.8). The interfacial capacitance of the semiconductor/electrolyte liquid junction is plotted as a function of applied voltage vs reciprocal of capacitance ($1/C^2$) (V). This produces a linear curve, the slope of which is used to calculate the donor carrier density and the intercept of the curve to its x-axis, which gives the built-in potential/flat band potential. These values allow for the calculation of band levels in relation to the reference potential of the reference electrode (15).

$$\frac{1}{C^2} = \frac{2}{\varepsilon\varepsilon_0 A^2 e N_D}\left(V - V_{fb} - \frac{k_B T}{e}\right) \quad (3.14)$$

Where C is the space charge capacitance, ε_o is the permittivity in a vacuum, ε is the dielectric constant of semiconductor, A is the active surface area of semiconductor, e is the electron charge, V is the applied potential, N_D is the donor density of semiconductor, V_{fb} is the flat-band potential, k_B is the Boltzmann constant and T is the absolute temperature.

$$N_D = \frac{2}{\varepsilon\varepsilon_0 eslope} \quad (3.15)$$

$$N_c = \frac{C_{sc}^2}{\varepsilon\varepsilon_o e_0^2} \quad (3.16)$$

$$E_C - E_{fb} = -k_B T \, In\left(\frac{N_D}{N_C}\right) \quad (3.17)$$

In the present work, PARSTAT 4000A electrochemical workstation is utilized for CV, LSV, EIS, and MS studies. The photoelectrochemical measurements are done by electrochemical work station PARSTAT 2000 attached with a light source Newport AM 1.5 G lens (100 mW/cm^2).

3.4.1.2 Scanning Electron Microscopy (SEM) /Energy Dispersive X-ray Spectroscopy (EDS)

The morphology and elemental composition of thin films are studied using scanning electron microscopy. It operates in vacuum with a high-energy electron beam directed through a series of apertures that interact with the sample under investigation, as shown in **Figure 3.4**. These incident electrons generate secondary electrons from the sample, which form an image and are partially reflected. These secondary electrons are referred to as back-scattered electrons. An electron gun, condenser, objective lens, sample, and electron collector are all part of the microscope. When combined with EDS, this aids in determining the elemental composition of the sample. The accelerating electron beam has a wavelength of 5-20 KeV and is produced by the slow heating of the filament in the electron gun. In general, lower incident energy is preferred because it limits the penetration volume and increases image resolution. Thus, Field Emission Scanning Electron Microscopy (FESEM) is used, which operates at a lower energy of 5 KeV emitted from a sharp Tungsten wire using cold cathode emission

Figure 3.4: Scanning Electron Microscope (Gemini SEM 500)

As a result, electrons from the inner shells of the atoms in the sample are ejected during the interaction process. Because of radiative recombination, electrons from the outer shells replace the shells, producing characteristic X-rays of that element and allowing composition to be determined (16).

In this study, a Hitachi SEM-S4300 and attached EDX system with a 20 KeV electron beam was used for compositional analysis, and a Zeiss Gemini 500 FESEM with a 5KeV electron beam was used for surface and cross-sectional analysis of thin films.

3.4.1.3 *X-Ray Diffraction (XRD)/ Glancing Angle X-Ray Diffraction (GIXRD)*

The crystallography of thin films is determined by XRD, a non-destructive method that uses an X-ray source such as copper to generate a Kα X-ray beam with a single wavelength using apertures. When this monochromatic radiation strikes the sample, the beam is diffracted, as determined by Bragg's law:

$$2d \sin\theta = n\lambda \qquad (3.18)$$

Where d is the distance between the lattice planes, n is an integer, λ is the wavelength, and θ is the diffraction angle.

The angle of incidence is adjusted for thin film analysis, which limits X-ray penetration and thus allows for better analysis of extremely thin coatings. This method is known as glancing incidence angle (GIXRD). The sample with thin coating is fixed at a small incident angle of 0.5° in the current work, and the X-ray detector is rotated. This causes diffraction near the surface from the grains, which obeys Bragg's law (17).

The lattice parameters, material structure, and crystallite size are all revealed by this method of characterization. The obtained patterns are collected and identified by comparing them to a massive database of diffraction results known as the International Centre for Diffraction Data (ICDD) with Powder Diffraction Database (PDF) files.

Figure 3.5: Powder X-Ray Diffractometer

The XRD analysis in this work is performed on a D8 advance Bruker with Cu- Kα radiation (λ=1.5Å) and a range of 2θ ~ 10 to 70° as shown in **Figure 3.5**. In addition, the crystallite size (D) is calculated using Debye Scherrer's equation and the Full Width Half Maximum (FWHM) of the pattern's prominent peak.

$$D = \frac{K\lambda}{\beta cos\theta} \qquad (3.19)$$

Where D is the crystallite size, K is the constant, λ is the wavelength of X-rays used for the analysis, β is the full width half maximum value of the intense peak and θ is Bragg's angle.

3.4.1.4 Raman Spectroscopy

Raman spectroscopy is used to investigate the vibrational frequency modes of the chemical phases within the material. This technique is applicable to gaseous, liquid, and solid samples. It is based on the inelastic scattering of atoms in materials when they are exposed to a laser beam. When the incident beam interacts with the atoms/defects of the materials, the molecules scatter light and shift up or down, thereby changing the polarizability. The modes of vibration caused by the inelastic scattering process indicate this shift in energy. The spectra are plotted as a frequency shift versus intensity. The relative intensities of the peaks are used for qualitative analysis, and the spectral database is used for interpretation. A standard optical microscope, an excitation laser, a monochromator, and a sensitive Charge Coupled Device (CCD) detector are the main components of the spectrometer (18).

Figure 3.6: Raman Spectrometer

The chemical phases of the samples in this work are investigated using a Horiba Jobin Yuon-Lab Ram HR-800 Raman spectrometer as shown in **Figure 3.6** with an Ar ion laser of 514 nm as an excitation source in the spectral range of 100-900 cm^{-1}.

3.4.1.5 Ultra Violet-Visible-Near Infra-Red (UV-VIS-NIR) Spectroscopy

The optical properties of thin films, such as absorption, reflection, and transmission, are measured with a UV-VIS-NIR spectrophotometer shown in **Figure 3.7**. These properties aid in calculating the bandgap of the material, which indicates the part of the solar spectrum that the material actually uses. It is a non-destructive and quick technique for process optimization of thin films. In the case of transparent thin films, electromagnetic radiation (EMR) is passed through the sample, and a portion of the light is absorbed while the remaining portion is transmitted. The transmitted light is measured, and this method is known as "specular transmittance mode." In the case of opaque thin films, a portion of the EMR light is reflected and the remaining portion is absorbed. This measurement technique is known as "Diffuse Reflectance Spectroscopy (DRS)." A light source, a monochromator, a sample holder, and a detector are the various components of a spectrophotometer (19).

Figure 3.7: UV-Visible Spectrophotometer

The absorption and transmission spectra in this study are captured using a Varian Cary UV-VIS-NIR Spectrophotometer. The bandgap of various thin films is calculated using Tauc's plot of $(\alpha h\upsilon)^2$ vs $h\upsilon$ that gives the direct bandgap of a semiconductor with the following equation.

$$\alpha h\upsilon = A(h\upsilon - E_g)^m \quad (3.20)$$

where A is a constant, $h\upsilon$ is the incident photon energy, α is the absorption coefficient, E_g is the band-gap energy of the film, m is equal to ½ for the direct allowed transition.

3.4.1.6 Stylus Profilometry

The thickness of a thin film is an important parameter that determines its various properties. In this work, the thickness is measured at a film edge with a Dektek stylus Profilometer. This Profilometer has a diamond-tipped stylus that directly contacts the surface with a force of 5 mg, causing no significant damage to the sample. This measurement typically necessitates a clear, sharp difference between the bare and deposited areas, which serves as a step (20). The sharp difference is created when the substrate is masked prior to material deposition. This causes height variations during the stylus scan, which are converted to electrical signals which used to create a profile. The thickness of the deposited film is determined by the step profile.

3.4.1.7 Current – Voltage (I-V) Measurements

The fully assembled device is assessed by measuring its I-V data, which evaluates the electrical properties of the solar cells. It serves as an indicator of device performance, which eventually aids in the improvement of experimental parameters. For the I-V measurements, the current work employs an Oriel Instruments model 94123A solar simulator connected with a Newport AM 1.5 G lens. The solar simulator is made up of a tungsten halogen lamp that has been pre-calibrated with a standard Si solar cell with a power of 100mW/cm^2 equal to AM1.5 G. The open-circuit voltage (V_{oc}), short-circuit current density (J_{sc}), fill factor (FF), and power conversion efficiency (η) of the device are the most important parameters evaluated from these measurements. In the dark, the measurements yield the rectification factor (RF), diode ideality factor (n), and barrier height (φ_b) (21). Figure 3.8 shows the ideal I-V characteristics of a solar cell under dark and light conditions.

The current obtained under illumination is given per area under light as below

$$J_{sc} = \frac{I_{sc}}{A} \tag{3.21}$$

Then the open-circuit voltage (V_{oc}) is termed as the maximum voltage obtained when there is no current flow in the external circuit and is given as

$$V_{oc} = n_2 \left[\varphi_b + \frac{kT}{e} ln\left(\frac{J_{sc}}{AT^2}\right)\right] \tag{3.22}$$

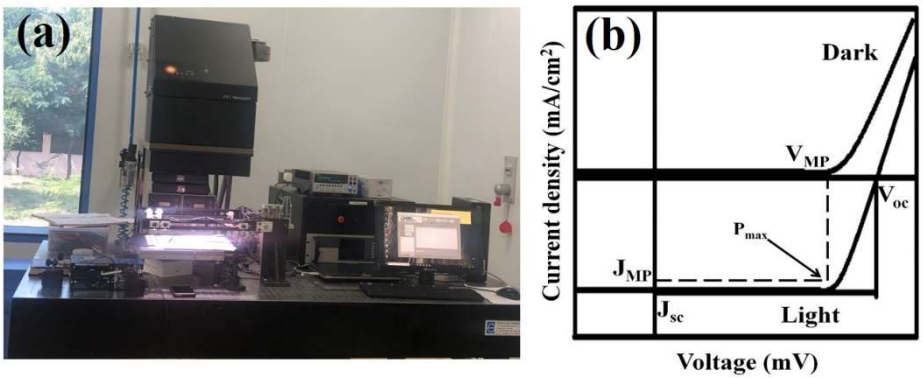

Figure 3.8: (a) Solar cell tester with simulator (b) Typical I-V characteristics of a solar cell

Where A is the area of the cell, *k* is the Boltzmann constant (1.81×10^{-23} J/K), T is the absolute temperature, and *e* is the electron charge (1.602×10^{-19} C)

The efficiency is calculated from the fill factor which is defined as the squareness of the area under the curve obtained from dark and light conditions.

$$FF = \frac{V_m I_m}{V_{oc} I_{sc}} \tag{3.23}$$

The efficiency is the ratio of power out to the input power (100 mW/cm^2) which is given as

$$\eta = \frac{output\ power}{input\ power} = \frac{V_{mp} J_{mp}}{P_{in}} = \frac{V_{oc} J_{sc} FF}{P_{in}} \tag{3.24}$$

3.5 Summary

The development of CIGS based solar cell can be achieved by simultaneous characterization of thin films using different analytical instrumentation. SEM-EDAX is utilized to understand the composition of film during its development and also examines the surface coverage of the grains at varied experimental conditions. Then the structural aspects are elucidated using XRD and Raman spectroscopic techniques. The optical properties such as absorbance and transmittance are studied using UV-VIS-NIR spectrophotometer. While the pn junction formation can be interpreted using electrochemical characterization such as Mott-Schottky analysis even before depositing the actual CdS or ZnS n-type semiconductor. Device performance is checked using the solar simulator which helps to understand the behavior of the device before this actual utilization in the direct sunlight.

References

1. A. C. Badgujar, S. R. Dhage and S. V. Joshi, *Thin Solid Films*, **589**, 79 (2015).
2. I. M. Dharmadasa, *Advances in thin-film solar cells*, CRC press (2012).
3. S. Mandati, B. V. Sarada, S. R. Dey and S. V. Joshi, *Materials Letters*, **118**, 158 (2014).
4. F. Nasirpouri, *Electrodeposition of Nanostructured Materials* (2017).
5. M. P. a. M. SCHLESINGER, *FUNDAMENTALS OF ELECTROCHEMICAL DEPOSITION*, NJ (2006).
6. B. Scharifker and G. Hills, *Electrochimica Acta*, **28**, 879 (1983).
7. J. Mostany, J. Mozota and B. R. Scharifker, *Journal of Electroanalytical Chemistry and Interfacial Electrochemistry*, **177**, 25 (1984).
8. L. Heerman and A. Tarallo, *Journal of Electroanalytical Chemistry*, **470**, 70 (1999).
9. M. T. M. Koper and J. H. Sluyters, *Journal of Electroanalytical Chemistry and Interfacial Electrochemistry*, **303**, 73 (1991).
10. O. Brylev, L. Roué and D. Bélanger, *Journal of Electroanalytical Chemistry*, **581**, 22 (2005).
11. M. S. Chandrasekar and M. Pushpavanam, *Electrochimica Acta*, **53**, 3313 (2008).
12. E. M. Espinoza, J. A. Clark, J. Soliman, J. B. Derr, M. Morales and V. I. Vullev, *Journal of The Electrochemical Society*, **166**, H3175 (2019).
13. D. D. MACDONALD, *Transient Techniques in Electrochemistry*, NEW YORK AND LONDON (1977).
14. R. C. Valderrama, P. J. Sebastian, J. Pantoja Enriquez and S. A. Gamboa, *Solar Energy Materials and Solar Cells*, **88**, 145 (2005).
15. a. G. J. E. Charles F. Windisch, *Journal of Vacuum Science & Technology A*, **18**, 1677 (2000).
16. T. K. Daniel Abou-Ras, and Uwe Rau, *Advanced Characterization Techniques for Thin Film Solar Cells*, Federal Republic ofGermany (2010).
17. K. S. Yoshio Waseda, Eiichiro Matsubara, *X-Ray Diffraction Crystallography*, Springer Heidelberg Dordrecht, London New York (2011).
18. Z. Xu, Z. He, Y. Song, X. Fu, M. Rommel, X. Luo, A. Hartmaier, J. Zhang and F. Fang, *Micromachines (Basel)*, **9** (2018).
19. M. Picollo, M. Aceto and T. Vitorino, *Physical Sciences Reviews*, **4** (2019).
20. A. Goudarzi, A. D. Namghi and C.-S. Ha, *RSC Adv.*, **4**, 59764 (2014).
21. C. E. N. a. B. I. A. Hafeez Y. Hafeez, *Journal of the Nigerian Association of Mathematical Physics*, **34**, 331 (2016).

CHAPTER 4

PULSE ELECTRODEPOSITION OF CISe AND CIGSe ABSORBERS

CHAPTER 4
PULSE ELECTRODEPOSITION OF CISe AND CIGSe ABSORBERS

4.1 Introduction

CIGS or CISe are the tetragonal chalcopyrite semiconductor materials. CISe is the basic structure in which In atoms are replaced by Ga atoms for the formation of CIGSe material. In the case of thin film solar cells, the absorption coefficient is very high that about 90 % of the photons from the solar spectrum are absorbed for the films having thickness > 1μm. This infact indicates that most of the photons absorbed and therefore 2-3 μm thick absorber is enough (1). This material exhibits both n-type and p-type semiconductor nature. However, copper poor films make it p-type with longer electron diffusion length. This conductivity can be achieved by varying the doping concentrations of Ga into the CISe lattice. The band gap varies between 1.0 eV to 1.67 eV between CISe and CIGSe with Ga content. The Cu/In ratio lies between 0.8 to 0.9 which is most acceptable for the formation of stoichiometric films. Among the thin film technologies, CIGSe and CISe absorber based solar cells are most advantageous due to their direct band gap and presence of minimal toxic metals when compared with CdTe solar cells. Another important advantage is the scope to fabricated the device in both substrate and superstrate configurations. While CdTe devices are available only in superstrate configuration. The commercialized CIGS solar cells are made using vacuum-based methods such as co-evaporation or co-sputtering of copper, indium, and gallium metals, followed by thermal treatment in the presence of selenium vapor to form CIGS. As a result, the fabrication cost is high, which raises the price of modules. Therefore, a method that can produce high-quality films that mimic the quality of films while outperforming their vacuum analogues is required.

Electrodeposition is the most cost-effective non-vacuum method available, with a high degree of material utilization that improves manufacturing cost benefits. The electrodeposition process for the preparation of CISe and CIGSe absorber layers is described in this chapter. The primary goal is to fabricate highly crystalline CISe and CIGSe absorbers for the fabrication of all

electrodeposited CIGS solar cells. It primarily makes use of acidic solutions of individual electrolytes or a single electrolyte containing salts of the Cu, In, Ga, and Se salts. The present utilizes methanol as electrolyte for the deposition of Cu and Ga that allows to deposit faultless films at more cathodic potentials. This is due to the fact that use of non-aqueous solutions increases the potential window for the metal reduction. The films are also evaluated for their morphological, structural, and optical properties. Using the knowledge gained from the literature review, the experimental conditions such as potential, pulse parameters, pH, and the preparation of different precursors using complexing agents for the electrodeposition of In and Ga metals are varied. The current study used a two-electrode system without the third reference electrode, to avoid impurities into the films. The obtained results are carefully interpreted in order to optimize the conditions for producing higher quality absorber layer for device fabrication. The electrodeposition is done by sequential electrodeposition process.

4.2 Sequential pulse electrodeposition of CIS and CIGS

4.2.1 Cyclic voltammetry

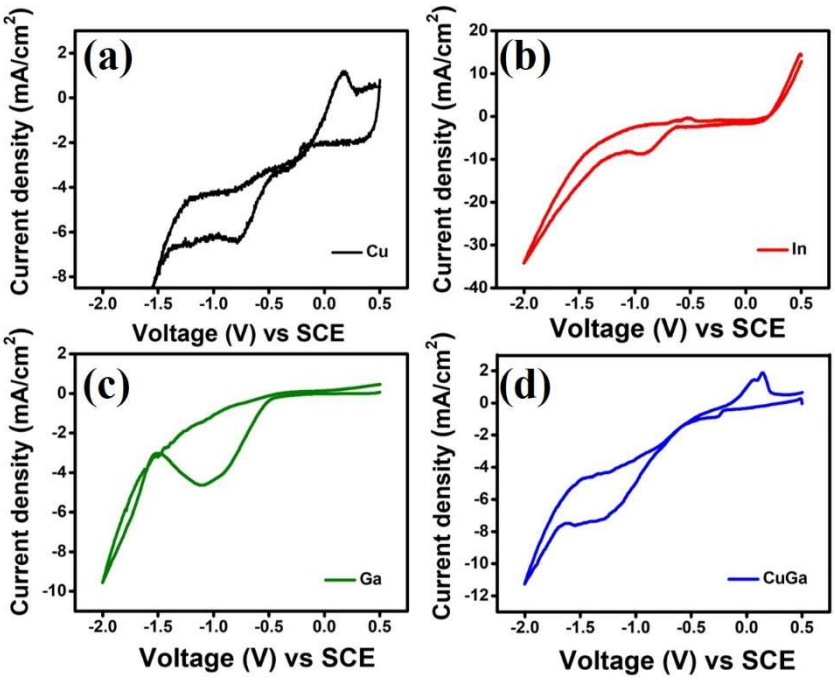

Figure 4.1: Cyclic voltammograms of (a) Cu, (b) In (c) Ga and (d) CuGa from methanol electrolyte; In from aqueous electrolyte with SDS as additive

Cyclic voltametric studies are performed in order to obtain the reduction potentials. Metal reduction and oxidation potentials are mainly interpreted using the cyclic voltammetry technique at a scan rate of 10 mVs^{-1} using 3-electrode system. Cu and Ga metal precursors are dissolved in methanol electrolyte while In in DI water, along with 170 mM sodium dodecyl sulphate (SDS) as a surfactant and LiCl as a supporting electrolyte. **Figure 4.1** shows cyclic voltammograms of metals Cu, In and CuGa, and it can be observed that (**Figure 4.1**a) that the CV obtained from a methanol electrolyte with 5 mM $CuCl_2$+ 170 mM SDS +70 mM LiCl reveals a Cu (II) to Cu reduction potential of -0.76 V vs SCE. There is only one peak corresponding to Cu (II) to Cu, indicating that there are no intermediates or complex formation. Furthermore, the presence of cross-over during its anodic scan indicates nucleation and crystallization. H_2 evolution is observed as a result of HER at more negative potentials, higher than -1.5 V vs SCE There is a broad peak at +0.14 V vs SCE in the anodic area, which corresponds to oxidation of excess Cu.

The cyclic voltammogram in **Figure 4.1**b obtained from an aqueous electrolyte comprising 45 mM $InCl_3$ + 170 mM SDS + 70 mM LiCl shows a cathodic peak at -0.9 V with no anodic peak, indicating irreversible reaction. In the case of Ga, **Figure 4.1**c, voltammogram is obtained from a methanol electrolyte containing 12 mM $GaCl_3$+ 170 mM SDS+ 70 mM LiCl. There is a noticeable reduction peak around -1.0 V versus SCE, which corresponds to the Ga reduction (2, 3). Ga is well-known for its affinity to oxide production in aqueous solutions. While, the use of methanol as electrolyte extends the potential window, while SDS surfactant slows down the HER, as seen by the emergence of a single peak in the cathodic area(4). Similarly, when the electrolyte containing both Cu and Ga is used for CuGa alloy deposition, there is a linear increase in cathodic current with a broad peak having maximum current at -1.3 V due to CuGa alloy deposition as seen in **Figure 4.1**d. The absence of any other cathodic peaks in the voltammogram suggests that the Cu and Ga are deposited as an alloy rather than as distinct metals (5). There is a shoulder peak in the anodic area at +0.03 V and +0.1V, indicating the oxidative response of the excess Cu redissolving into the electrolyte. It can be observed from the cathodic reactions of individual elements (Cu -0.7 V and Ga -1.0 V) and the CuGa alloy, that the reduction potential shifts towards greater negative values to -1.5 V due to gallium deposition along with Cu, showing the alloy deposition (5).

Furthermore, the crossover in the curve during the scan from cathodic to anodic potentials indicate improved nucleation and growth(6). In all cases, the current density increases rapidly above -1.5 V due to the HER reaction, although no H_2 bubbles are visible in the electrolyte during the CV measurements. Cathodic depositions of Cu are thus accomplished at -1.5 V, whereas In, Ga, and CuGa are performed at -2.0 V. Furthermore, the surface morphology and composition of the films are tuned by adjusting the deposition time and pulse parameters during the precursor deposition followed by a selenization treatment to form CIGS.

4.2.2 Experimental

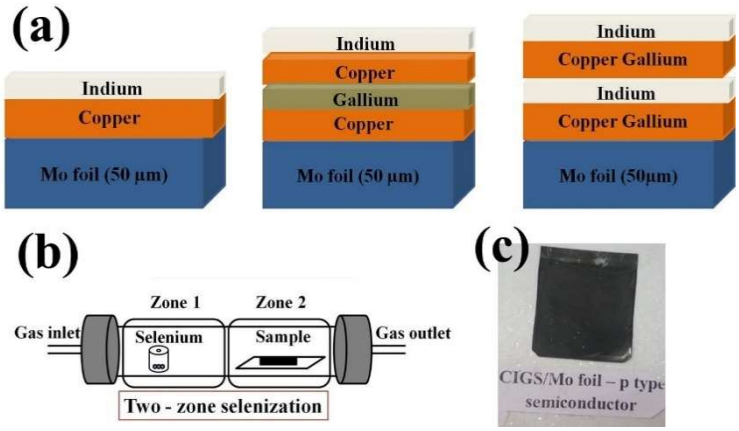

Figure 4.2: Schematic of different approaches in the multilayer deposition of metal precursors, (b) selenization process (c) visual appearance of CIGS film

The CISe and CIGSe thin-films in this study are produced by selenizing the electrodeposited metallic stacks over Mo substrate (**Figure 4.2**), as described in chapter 3.3.1. Similar method of nonaqueous electrolyte is previously explored by Fei Long et al, where alcohol is utilized as an electrolyte and deposited CIGS in single step and produced phase-pure CIGS with post- thermal annealing at 550ºC (7). While Pin-Kun Hung et al. deposited CIGS from an aqueous electrolyte using a single step deposition with SDS surfactant to avoid secondary phase formation (8). In both the approaches, the deposition is done in a single step that includes all the four elements using a three-electrode system. However, in the current work, the depositions of individual metals Cu, Ga are investigated in methanol +SDS+LiCl containing electrolyte while Indium from an aqueous electrolyte along with SDS as surfactant and LiCl as a supporting electrolyte that is carried out using a 2-electrode system. This method is developed following a series of experiments

attempting to deposit Cu (at -1.5 V) and Ga (-2.0 V) as stack layers from individual methanol containing electrolytes. Moreover, sequential deposition of metals failed to incorporate stoichiometry Ga and resulted in a porous Cu layer. Therefore, in order to incorporate good amount of Ga into the films, an electrolyte containing both Cu and Ga are used to deposit CuGa alloy at -2.0 V potential at 50 % duty cycle. Following that, In is deposited from an aqueous electrolyte.

Figure 4.2a depicts the schematic of metal deposition and the selenization process. In approach 1, single Cu and single In layer are deposited sequentially. The Cu layer at -1.5 V for 10 minutes, followed by the In layer deposition at -2.0V for 4 minutes. Both the metals are deposited at 50% duty cycle. In approach 2, a gallium layer is deposited at -2.0 V at 50% duty cycle between two copper layers, followed by an indium layer. In approach 3, Cu and Ga are deposited as CuGa alloy at -2.0 V at 50% duty cycle for 10 minutes, followed by In at -2.0 V at 50% duty cycle for 4 minutes. Finally, all the films are selenized in a two-zone furnace, where the samples are placed in a zone different from the selenium source. These two zones are kept at different temperatures and allowed to evaporate the selenium. The sample kept at 550°C reacts with the selenium vapor evaporated from its metallic pellets held at 230-260°C (9). This promotes recrystallization of the CIGS or CISe phase, as shown in the schematic **Figure 4.2**b. Further, **Figure 4.2**c depicts the visual appearance of the films that are tested for morphological, structural, and optical properties. This indicates that the reduction potentials of the corresponding metals, as well as their alloys, play a significant role in the deposition mechanism.

4.2.3 Composition and Surface Morphology

The prepared CIG precursor films are examined for their composition and morphology. The films from approach 1, deposition of copper is done at -1.5 V for 10 min followed by In deposition at -2.0 V for 5 min at 50 % duty cycle at room temperature. The films are investigated using Scanning Electron Microscopy with EDS for the composition of Cu, In, Ga, and Se content in atomic percent and morphology utilizing the aforementioned procedures in **Figure 4.2**a. **Table 4.1** shows the composition of the electrodeposited films after selenization using three processes. In approach 1, the films are prepared by sequentially depositing In/Cu layers on Mo, followed by selenization which resulted in a Cu+In/Se ratio of 0.9, indicating slightly copper-rich films. In addition, when the films are deposited using approach 2 as described in section **Figure 4.2**a, the Ga is integrated between layers of Cu and In. The composition in this case was indium-rich with

very small concentrations of copper, indicating non-stoichiometry. Though the multilayer method makes individual element deposition easier, integration of gallium into CIS films remains difficult. Then, a third approach described in section **Figure 4.2**a is used to deposit copper and gallium together as an alloy (In/CuGa/Mo). When compared to approach 2, the composition of the films in this technique revealed a superior Cu/In+Ga ratio of 0.8 and a better Ga/In+Ga ratio (**Table 4.1**).

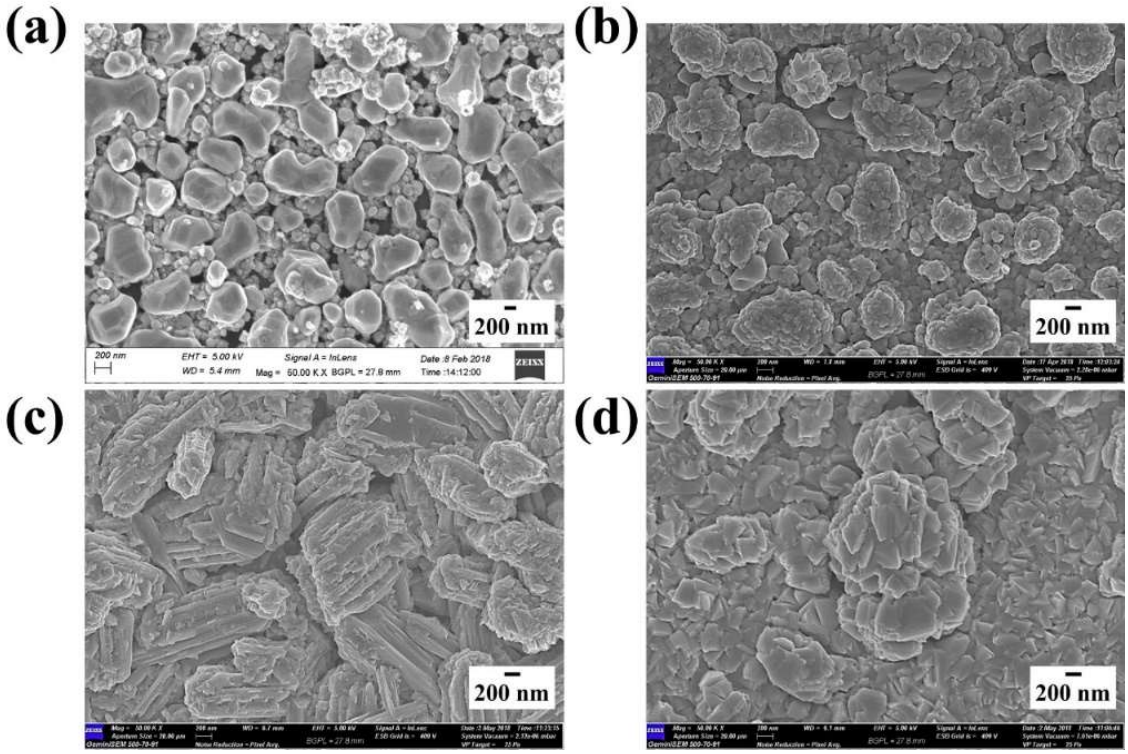

Figure 4.3: Surface morphology of (a) as-deposited In/Cu/Mo (b) CISe/Mo (c) In/Ga/Cu/Mo (CIGSe) (d) In/CuGa/Mo (CIGSe)

The surface morphology of as-deposited films containing In/Cu/Mo, In/Ga/Cu/Mo, or In/CuGa/Mo grains consists of similar grain structure due to the top In layer covering the beneath precursor layers. In all the cases, In layer has a grain size of about 96 nm, as shown in **Figure 4.3**a. All of the precursor films are post-treated under identical selenization conditions. It is observed that in **Figure 4.3** b the grains of CISe are rough due to island growth of indium but are still possess uniform coverage. **Figure 4.3** c depicts the planar view of CIGSe appeared to have highly rough and twinned grains developed when Ga layer is deposited between Cu and In layers. This

could be due to uneven gallium layer which thereby led to uneven growth of In topmost layer. . However, when Ga is deposited along with Cu as an alloy (CuGa) the morphology of grains is much better as shown in **Figure 4.3**d, with less island CIGSe grains and showed uniform grains when compared to approach 2 (10).

Furthermore, a closer look at the images in **Figure 4.3**b and **Figure 4.3**d, reveals that the roughness of the grains by approach 3 is significantly lower than those prepared through approach 2. These findings are consistent with the CV study, which shows that Ga deposition involves higher H_2 evolution than CuGa alloy deposition due to formation of pure Cu phase along with alloy formation (5).. As a result, the deposition potential is an important parameter, and thus methanol in the current technique increases the reduction potential window for the metal deposition while SDS retards the HER reaction. As a result, this is a big step forward in the use of SDS additive in the non-aqueous electrolyte for CuGa alloy deposition.

Table 4.1: Composition of as-deposited Cu and In layers on Mo foil

Approach 1

Elements	CISe	
	As-deposited	Selenized
Cu	52.0	27.0
In	48.0	21.0
Se	-	52.0
Cu+In/Se (1.0)	-	0.9

Approach 2

Elements	CIGSe	
	As-deposited	Selenized
Cu	34.5	8.2
In	51.0	30.5
Ga	14.5	6.3
Se	-	55.0
Cu/In+Ga (0.83-0.92)	0.5	0.2
Ga/In+Ga (0.26)	0.2	0.2

Approach 3

Elements	CIGSe	
	As-deposited	Selenized
Cu	44.0	22.0
In	53.0	26.0
Ga	2.0	3.0
Se	-	49.0
Cu/In+Ga (0.83-0.92)	0.8	0.8
Ga/In+Ga (0.26)	0.03	0.1

4.2.4 Structural Analysis

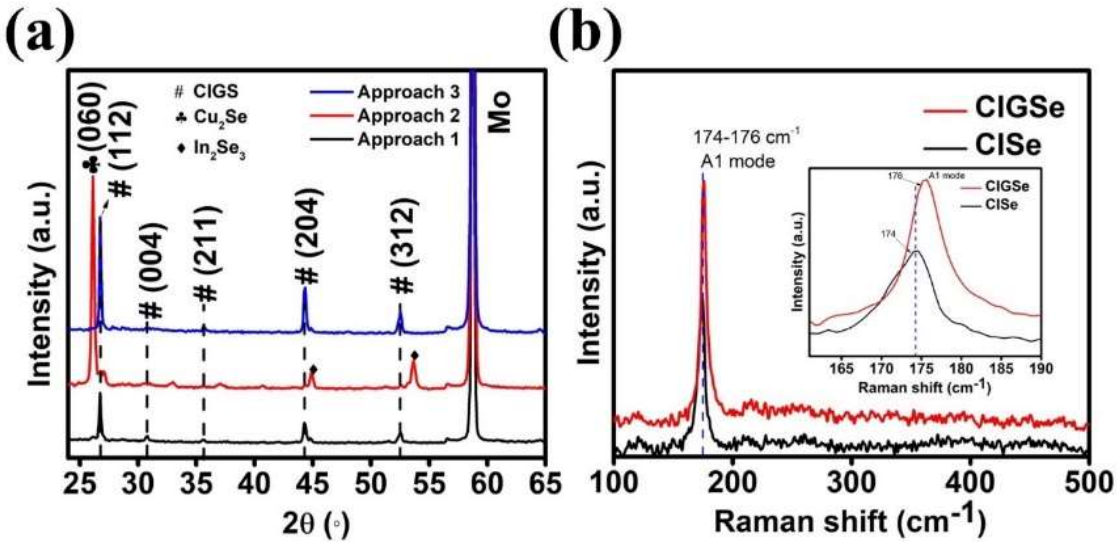

Figure 4.4: (a) XRD patterns (b) Raman spectra of CISe and CIGSe absorber developed from multilayer precursor (approach 1 and 3)

Figure 4.4a depicts the XRD pattern of CISe and CIGSe absorbers manufactured using various methods. 1st approach yielded phase-pure CISe with a strong peak at 2 theta values of 26.6 °, 44.1 °, and 52.4 ° corresponding to the (112), (204), and (312) planes of tetragonal phase (JCPDS file 01-083-4869). Secondary phases such as Cu_2Se (♣) and In_2Se_3 (♦) have been detected in films deposited using 2nd approach. Ga layer is sandwiched between two successive Cu and In layers, the top layers react with Se, resulting in the formation of these secondary phases due to incomplete reactivity. This is also consistent with the EDS composition shown in **Table 4.1**. As a result, the rough grains in **Figure 4.3**c are attributed to the In_2Se_3 phase that is also evident from the

stoichiometry of the film. When gallium is introduced along with Cu (CuGa/In) in the precursor film employing 3rd approach, however, significant heterogeneity in composition is seen. By using this method, there is a clear improvement in crystallinity with increased peak intensity but negligible variation in the 2 values, indicating a low gallium concentration to replace the indium atoms, as shown in **Figure 4.4**a.

Additionally, micro-Raman analysis has revealed strong peaks associated to CISe and CIGSe respectively. The peak for CISe is 173 cm^{-1}, and the peak for CGSe is 188 cm^{-1} (11, 12). the CIGSe peaks are generally be observed between 173 and 188 cm^{-1}, which is highly dependent on the amount of Ga introduced into the lattice to replace the In. The present spectra of the CISe and CIGSe films of **Figure 4.4**b reveal a considerable change in the values between 174-176 cm^{-1} for A1 mode due to Se atoms vibrating with the Cu,In,Ga atoms in the lattice. It is also evident from EDS results (**Table 4.1:** Composition of as-deposited Cu and In layers on Mo foil). It demonstrates that gallium is low in 3rd approach but still shows an upshift in wavenumber towards 176 cm^{-1} with gallium inclusion in the CISe films. Secondly, the absence of any secondary phases in the spectra indicates that this 3rd approach to producing phase-pure CIGSe thin films is effective. A detailed inspection of the composition and XRD results reveals that 2nd approach fails to produce high-quality films when compared to the 3rd one. As a result, the properties of the films are investigated further on identical films made using approaches 1 and 3 for CISe and CIGSe, respectively.

4.2.5 Optical Properties

The absorbance of the CIS and CIGS layers is measured using a UV-VIS-NIR spectrophotometer, and the optical bandgap is calculated using Tauc's plot relation, as shown in

$$\alpha h\upsilon = A(h\upsilon - E_g)^m \qquad (3.20).$$

Where A is a constant, $h\upsilon$ is the incident photon energy, α is the absorption coefficient, E_g is the band-gap energy of the film, m is equal to ½ for the allowed transition.

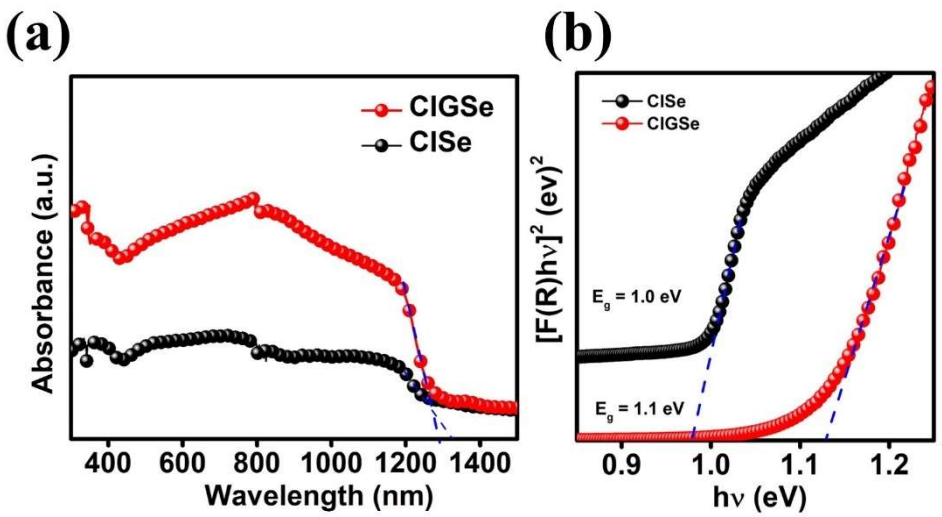

Figure 4.5: (a) Absorbance spectra and (b) Tauc's plots of CISe and CIGSe absorbers

Figure 4.5a depicts the absorbance of the films CISe and CIGSe measured in the wavelength range of 300-1500 nm. In both situations of CISe and CIGSe, there is a large range of absorption in the visible area between 500-1000 nm. The drop in the curve beyond 1000 nm represents a decrease in absorbance, which varies for CISe (1324 nm) and CIGSe (1286 nm). It is observed that CIGSe has higher absorption than CISe due to the addition of Ga, that widens the bandgap and thus has good absorption of sunlight and displays improved performance for solar cell applications. The shape of the curve increased gradually with flatten base with no elevations as shown in Figure 4.5b. This indicates that there is no change in the momentum while excitation of electron and thereby confirms the direct band gap. The band gap values are 1.0 eV for CISe and 1.1 eV for CIGSe films, respectively.

4.3 Variation of Deposition Parameters to Enhance the Thickness of the Absorber

Increasing the thickness of the absorber layer are being investigated as shown in **Figure 4.6**.

a) Extend the electrodeposition time to generate thicker layers of Cu(Ga)/In, followed by selenization to form CI(G)S.
b) Multiple layers of Cu(Ga)/In electrodeposited with varying pulse settings to generate a thick film of CI(G), followed by selenization

4.3.1 Scheme (a)

Figure 4.7a depicts a cross section of CISe deposited using approach (a) with extended copper layer deposition period and then that of indium layer. Non-uniform crystalline grains with an overall thickness of roughly 600 nm are seen. Figure 4.7b indicates that the thickness of the as – formed Cu/In layer is approximately 436 nm as measured with a stylus Profilometer.

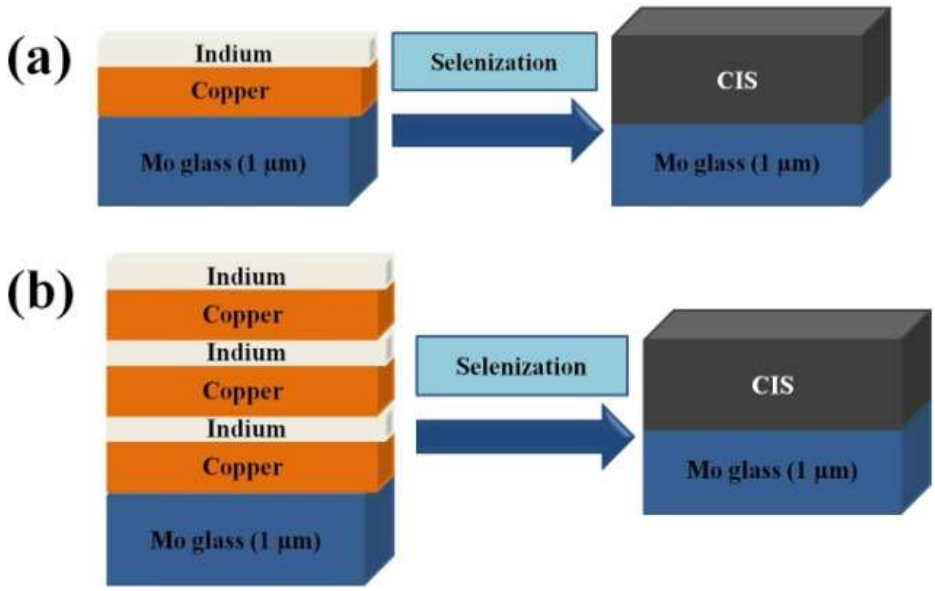

Figure 4.6: Schematic of different approaches to increase the thickness of the absorber layer

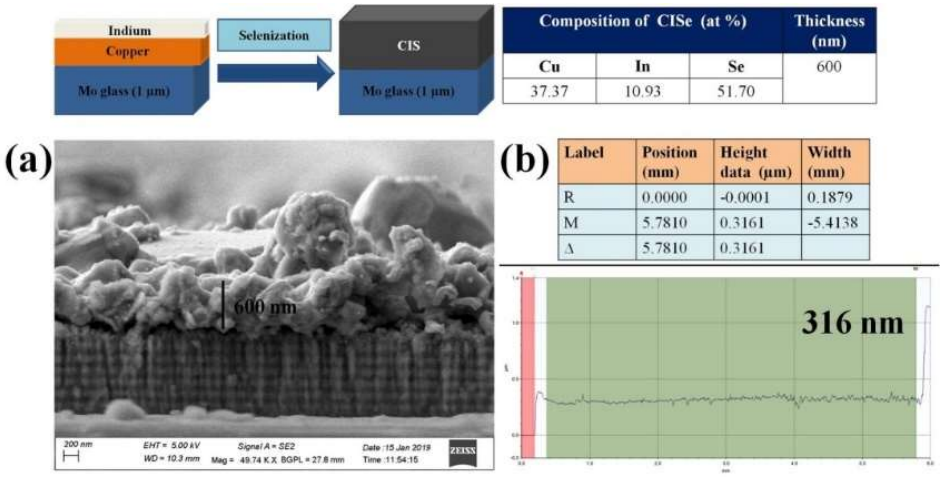

Figure 4.7: (a) Cross sectional analysis of CISe thin film (b) Thickness measurement using stylus Profilometer

According to the composition analysis of the layers, it is copper rich. This could be ascribed to the presence of a much thicker copper layer compared to indium, since copper is deposited for a longer period of time. Therefore, optimization of deposition parameters must be investigated in order to improve the stoichiometry of the films.

4.3.2 Scheme (b)

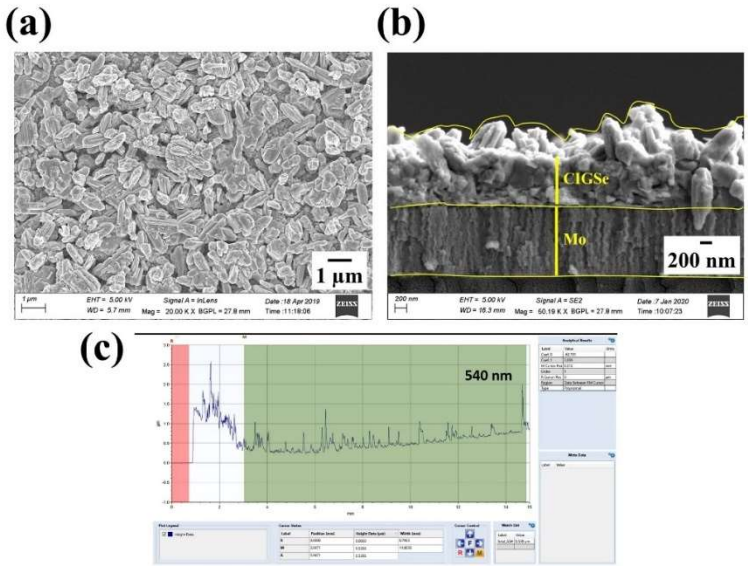

Figure 4.8: (a) Surface morphology of CIS on Mo (b) cross-section of CIGSe film on Mo substrate (c) Step profile of thickness measured using stylus profilometer

Thin layers of Cu and In are deposited in sequence to form a stack, which is then selenized to produce CISe absorber. Figure 4.8a shows the microstructure of CISe films deposited using various pulse parameters and investigated using FESEM. By changing the off-time (40% duty cycle) during the succeeding layers of Cu/In, the internal stress is reduced with uniform layers of Cu/In amounting to 6 layers Crystalline grains were formed as a result of the selenization of Cu/In layers. Figure 4.8b depicts the cross-sectional analysis revealing the thickness of CISe film. **Figure 4.8**c shows the step profile of as-deposited Cu/In layers of approximately 546 nm. It shows the smooth surface where the Cu/In layers are formed in sequence with different pulse settings. Similarly, CuGa alloy and In layers are sequentially deposited to form the CIGSe absorber. As per the EDS analysis, the composition of the CISe films is Cu 25.0 %, In 19.0 %, and Se 56.0 %, whereas the composition of the CIGSe films is Cu 28.6 %, In 28.2 %, Ga 1.2 %, and Se 42.0 %. The CIGSe films obtained with multiple layers of In/CuGa/Mo resulted in copper-rich films that

are detrimental to the device performance. Hence, only CISe films of this approach are utilized for the device fabrication.

The data on composition and thickness obtained using this method justify further development of the method. It can be noted that the pulse parameters are crucial in gaining better stoichiometry absorbers with optimal thickness. These absorbers are used to fabricate CIGSe and CISe solar cells employing electrodeposited CdS and ZnS thin films as buffer layers, which will be addressed in chapter 7.

4.4 Summary

CISe and CIGSe absorbers are successfully prepared by pulse electrodeposition using methanol as electrolyte. This electrolyte is modified by adding SDS that favored the grain refinement. The methanol electrolyte devoid of water is utilized for the Cu and Ga depositions that even facilitated the formation of CuGa alloy. The methanol electrolyte widens the deposition potential of the metals that enhance the alloy formation. However, when the films were made by sequential metal deposition, the absorbers had a better composition and crystallinity. Further, the change in pulse variables is investigated to generate CISe absorbers with a thickness of 500 nm by depositing multiple layers of metal stacks followed by selenization.

References

1. S. Sharma, K. K. Jain and A. Sharma, *Materials Sciences and Applications*, **06**, 1145 (2015).
2. J. C. Malaquias, D. Regesch, P. J. Dale and M. Steichen, *Physical chemistry chemical physics : PCCP*, **16**, 2561 (2014).
3. Y. Chung and C.-W. Lee, *Journal of Electrochemical Science and Technology*, **4**, 1 (2013).
4. W. Monnens, C. Deferm, J. Sniekers, J. Fransaer and K. Binnemans, *Chem Commun (Camb)*, **55**, 4789 (2019).
5. L. Ribeaucourt, G. Savidand, D. Lincot and E. Chassaing, *Electrochimica Acta*, **56**, 6628 (2011).
6. A. Sahari, A. Azizi, G. Schmerber and A. Dinia, *Surface Review and Letters*, **15**, 717 (2008).
7. F. Long, W. Wang, J. Du and Z. Zou, *Journal of Physics: Conference Series*, **152**, 012074 (2009).
8. P.-K. Hung, C.-H. Huang and M.-P. Houng, *Journal of Materials Science: Materials in Electronics*, **25**, 1848 (2014).
9. S. Mandati, P. Misra, D. Boosagulla, T. N. Rao, B. V. J. M. f. R. Sarada and S. Energy, **9**, 1 (2020).
10. Q. Huang, K. Reuter, S. Amhed, L. Deligianni, L. T. Romankiw, S. Jaime, P. P. Grand and V. Charrier, *Journal of The Electrochemical Society*, **158** (2011).
11. V. Izquierdo-Roca, E. Saucedo, J. S. Jaime-Ferrer, X. Fontané, A. Pérez-Rodríguez, V. Bermúdez and J. R. Morante, *Journal of The Electrochemical Society*, **158**, H521 (2011).
12. D. Papadimitriou, N. Esser and C. Xue, *physica status solidi (b)*, **242**, 2633 (2005).

CHAPTER 5

PULSE ELECTRODEPOSITED CdS AND ZnS LAYERS FOR CIGS DEVICES

CHAPTER 5
PULSE ELECTRODEPOSITED CdS AND ZnS BUFFER LAYERS FOR CIGSe DEVICES

5.1 Introduction

pn junction formation is most crucial aspect for the solar cells to work. Therefore, the properties of *p* type semiconductor and *n* type semiconductor play an important role in alignment of conduction bands between absorber and window layer. Till date, CdS with a bandgap of 2.4 eV deposited using CBD technique has shown appreciable efficiencies. However, from the environmental point of view it is recommendable to use non-toxic materials in the device construction. Therefore, among non-toxic and eco-friendly buffer materials ZnS is observed to possess better lattice match with the CIGS absorber. Also, it possesses wide bandgap varying between 3.0 eV to 3.8 eV that increases the power conversion as wide bandgap transmits more photons covering the solar spectrum.

This chapter presents an electrochemical process for the deposition of CdS and ZnS thin films without a post heat treatment for their use as buffer layers in the CISe and CIGSe devices. The present process for a room temperature electrodeposition of the buffer layers is reported for the first time. The films are deposited at room temperature using a two-electrode system. With an extensive survey on the electrodeposition of CdS and ZnS thin films, it is understood that the deposition is performed at higher temperatures due to the formation of colloidal sulfur in the electrolyte at ambient temperature, since it is necessary to suppress the colloidal sulfur while electrodepositing the films. It is well known, that the dissociation constants of organic acids are higher comparatively from the inorganic acids, thus the use of tartaric acid is used to reduce the formation of sulfide precipitation in the electrolyte. Hence, present study investigated the role of organic additives such as tartaric acid and glycerol in the formation of phase-pure thin films which will be discussed in detail.

5.2 PART A Electrodeposition of CdS Thin Films at Room Temperature

5.2.1 Linear Sweep Voltammetry of CdS Deposition

Linear sweep voltammetry (LSV) is used to determine the reduction potentials of individual cadmium (Cd) and sulfur atoms (S). LSV curves for cadmium and sulfur precursors, as well as the Cd-S system using a two-electrode system, are recorded in the potential regime of 0 to -1.5V. The precursor concentrations used for LSV measurement are the same in both the electrolytes with and without tartaric acid. CdS electrodeposition in the presence of tartaric acid aids in the formation of cadmium tartrate complex, when the Cd ions combine with the tartrate ions while leaving unreacted protons behind (1). Colloidal sulfur is formed when these available protons combine with thiosulfate ions from the sulfur precursor (reaction 5.2). However, the formation of colloidal sulfur in the current study is significantly slower because the higher tartaric acid dissociation constant, (pKa, ~ 2.98), compared to a conventional strong acid like H_2SO_4 (1.92) (2). The pH of the precursors is adjusted to 2.5 in each case. It is also well known that thiosulfate ion dissociation is significantly higher at pH values less than 5 (3, 4). Conventional strong acids, such as H_2SO_4 and HCl, dissociate quickly, releasing more protons that can be used to form excess colloidal sulfur. Here, tartaric acid acts as a pH adjuster as well as complexing agent during the electrodeposition of CdS, increasing the availability of sulfur ions for the formation of CdS.

Figure 5.1a depicts the LSV of 2 mM $CdSO_4$ with tartaric acid, revealing a well-defined reduction peak at -0.9 V for Cd and a potential regime of the reduction ranging from -0.6 to -1.0 V. Similarly, LSV of 158 mM $Na_2S_2O_3$ in tartaric acid, shown in 5.1b unveils the possible sulfur reduction window from of -0.68 to -1.2 V. However, a well-defined reduction peak appeared at -1.01 V, which is comparable to previously reported values (5). Figure 5.1c shows that CdS reduction begins at -0.6 V and has a pronounced reduction peak at -1.2 V, confirming CdS formation, which is further supported by the emergence of yellow films. Figure 5.1d shows the LSV of Cd-S with a three-electrode system, where SCE is used as a third electrode, exhibiting negligible difference compared to the two-electrode system on the growth potentials of CdS thin films.

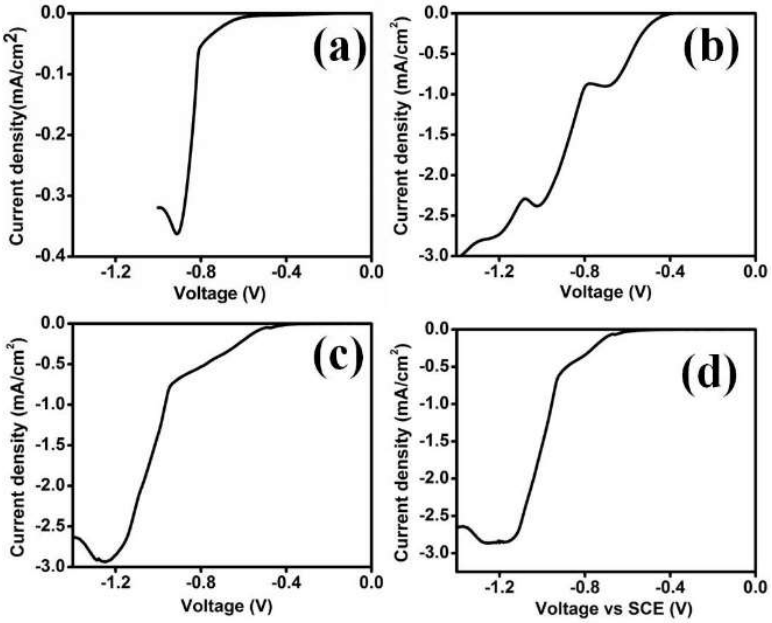

Figure 5.1: Linear sweep voltammogram curves recorded with a potential sweep rate of 10 mV/s for (a) $CdSO_4$ (b) $Na_2S_2O_3$ and (c) & (d) $CdSO_4$ + $Na_2S_2O_3$, using a two-electrode system and three-electrode system respectively, with tartaric acid as complexing agent

5.2.2 Growth Mechanism of Pulse Electrodeposited CdS with Tartaric Acid

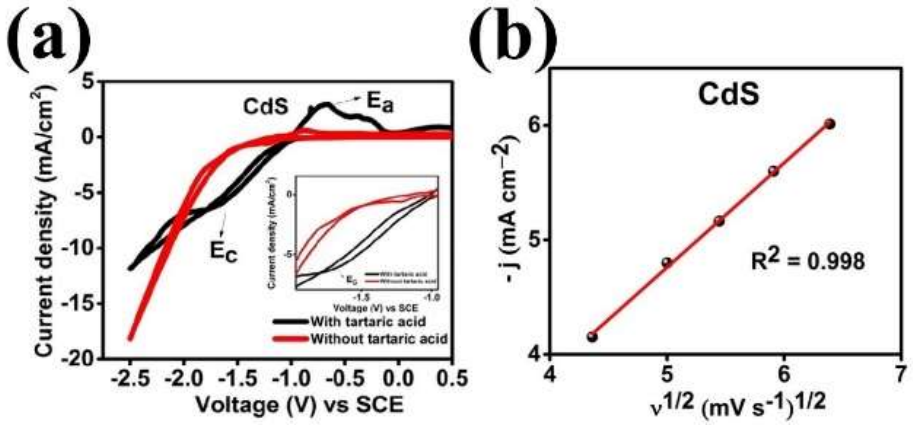

Figure 5.2: Cyclic voltammograms of (a) $CdSO_4$ + $Na_2S_2O_3$ in tartaric acid (b) current density vs square root of sweep rates

Cyclic voltammograms (CV) are recorded to evaluate the electrochemical reduction mechanism of CdS in the presence and absence of tartaric acid. **Figure 5.2**a depicts the CV acquired with a scan rate of 50 mVs^{-1} in an electrolyte containing $CdSO_4$ + $Na_2S_2O_3$ with and

without tartaric acid at pH 2.5 and pH 6.2, respectively. The large difference in the anodic and cathodic peak potentials (ΔE_p) ($\Delta E_p = \left|E_{pa} - E_{pc}\right|$) of the CV, as shown in **Figure 5.2**a, illustrates the irreversibility of the oxidation/reduction reactions for the electrolyte without tartaric acid (6).

In the absence of tartaric acid, no noticeable reduction peaks are detected due to the susceptible production of $Cd(OH)_2$ at pH 6.2, which may lead to colloidal sulfur accumulation at the cathode, resulting in low CdS generation (7). The observed CV conduct (without tartaric acid) is consistent with the atomic composition shown in Table 5.1, where the film is found to contain only sulfur due to adsorbed sulfide species. During the cathodic scan in the presence of tartaric acid at pH 2.5, the current increases in the potential range between -1.0 and -1.7 V versus SCE (**Figure 5.2**a), with a significant reduction of cadmium and sulfur precursors. As demonstrated in reaction, the reductive reaction involves the creation of an intermediate complex (cadmium tartrate) (reaction 5.1). The Cd^{2+} ions in the complex breakdown and react with the adsorbed sulfide reactions (reactions 5.2,5.3) and form CdS (reaction 5.4). Thus, tartaric acid plays a major role in the complexation of metal ions because it affects the kinetics of thiosulfate dissociation, controls sulfide precipitation, and accelerates deposition. During the anodic scan, a crossover for the germination of nuclei with three-dimensional (3D) nucleation is observed (8), promoting the formation of crystalline CdS films (9). Following that, shoulder peaks noticed in the anodic curve at -0.68 V and -0.38 V vs SCE (E_a) linked with the dissolution of excess Cd (10) (11). Thus, the addition of tartaric acid affected the composition of the film, identifying both Cd and S elements in accordance with the CV investigation. The peak current densities of reduction are displayed against the square root of the different sweep rates obtained at the optimal potentials -1.1 V to further analyze the deposition process. **Figure 5.2**b shows the peak current density (j) vs the square root of the sweep rate (υ) plot for CdS, which shows a linear increase and confirms that the depositions involve are diffusion-controlled process (12).

$$Cd^{2+} + C_4H_6O_6 + 2OH^- \leftrightarrow [CdC_4H_4O_6]^{2+} + 2H_2O + 2e^- \quad (5.2)$$

$$S_2O_3^{2-} + 2H^+ \rightarrow S_{(\downarrow)} + H_2SO_3 \quad (5.3)$$

$$S_{(\downarrow)} + H_2SO_3 + 2e^- \rightarrow H_2S_{(ads)} + SO_3^{2-} \quad (5.4)$$

$$Cd^{2+} + H_2S_{(ads)} \rightarrow CdS + 2H^+ \quad (5.5)$$

Table 5.1: Composition of CdS and ZnS films deposited during cyclic voltammetry with and without tartaric acid at room temperature

Composition of films from cyclic voltammetry (at %)		
CdS	Cd (%)	S (%)
Without tartaric acid	0	100
With tartaric acid	26	74

Voltammetric studies reveal that Cd, S, and CdS can be deposited in a common potential window of -0.8 to -1.2 V, which is consistent with prior observations (13). The conclusions derived from the CV and LSV tests are then used to define the deposition potential for the electrodeposition of CdS films. Figure 5.3a depicts the visual appearance of as-deposited CdS films at various deposition potentials, indicating that deposition of CdS may not occur at potentials less than -1.0 V using a two-electrode system, whereas for potentials more negative than -1.0 V, the transparent FTO substrate turned yellow, indicating CdS formation. while the relative contents of Cd and S change in films formed at higher cathodic potentials. It is widely known that crystalline CdS films with n-type conductivity require a slightly lesser Cd content with a Cd/S ratio smaller than one. CdS films deposited at -1.1 V have Cd and S compositions such that the Cd/S ratio is 0.91, demonstrating the desired stoichiometry. Furthermore, increasing the deposition potential to -1.2 V resulted in non-uniform films due to dominant H2 evolution. A deposition potential of -1.1 V is now considered ideal for pulse electrodeposition of CdS films. In addition, the interpretation of the nucleation and growth mechanism is evaluated using current-time curves produced from chronoamperometry.

Table 5.2 shows the composition of pulse electrodeposited CdS films with varying deposition potential. Cd and S are not present in films deposited at potentials less than -1 V, . while the relative contents of Cd and S change in films formed at higher cathodic potentials. It is widely known that crystalline CdS films with n-type conductivity require a slightly lesser Cd content with a Cd/S ratio smaller than one. CdS films deposited at -1.1 V have Cd and S compositions such that the Cd/S ratio is 0.91, demonstrating the desired stoichiometry. Furthermore, increasing the deposition potential to -1.2 V resulted in non-uniform films due to dominant H_2 evolution. A deposition potential of -1.1 V is now considered ideal for pulse electrodeposition of CdS films. In

addition, the interpretation of the nucleation and growth mechanism is evaluated using current-time curves produced from chronoamperometry.

Table 5.2: Composition of as-deposited CdS thin films with variation in deposition potential determined using energy dispersive X-ray spectroscopy

Deposition Potential (V)	Composition (at. %)		Cd/S
	Cd	S	
-1.0	43.35	56.65	0.76
-1.1	47.86	52.14	0.91
-1.2	42.75	57.25	0.74

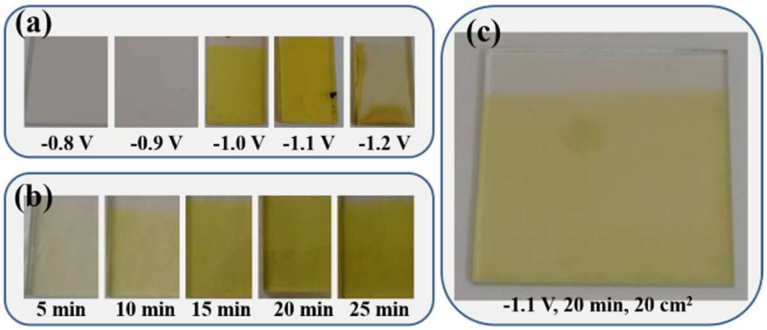

Figure 5.3: Visual appearance of pulse electrodeposited CdS thin films on FTO with variation in (a) deposition potentials, (b) deposition time and (c) large area (~ 20 cm^2) CdS films electrodeposited using optimum condition, at -1.1 V for 20 min

5.2.3 Chronoamperometric Studies

Chronoamperometric studies are conducted to have a better understanding of the nucleation and growth mechanisms of the CdS films on FTO substrates using electrolytes containing Cd + S precursors in tartaric acid. Figure 5.4a depicts the j-t curves corresponding to the CdS deposition potentials. As shown in Figure 5.4a, the current corresponding to the deposition of CdS is insignificant at voltages of -0.8 V and -0.9 V.

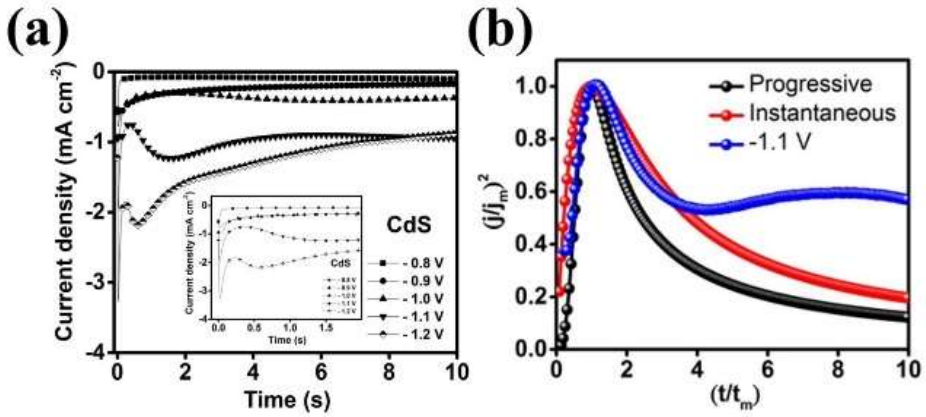

Figure 5.4: Chronoamperometric curves of (a) CdS at various deposition potentials (b) dimensionless curves of $(j/j_{max})^2$ vs (t/t_{max}) of CdS at -1.1 V along with the theoretical plots corresponding to the progressive (black curve) and instantaneous nucleation (red curve)

Furthermore, there is an increase in current at potentials -1.0, -1.1, and -1.2 V as a result of the CdS deposition. As an inference from the EDS data in while the relative contents of Cd and S change in films formed at higher cathodic potentials. It is widely known that crystalline CdS films with n-type conductivity require a slightly lesser Cd content with a Cd/S ratio smaller than one. CdS films deposited at -1.1 V have Cd and S compositions such that the Cd/S ratio is 0.91, demonstrating the desired stoichiometry. Furthermore, increasing the deposition potential to -1.2 V resulted in non-uniform films due to dominant H2 evolution. A deposition potential of -1.1 V is now considered ideal for pulse electrodeposition of CdS films. In addition, the interpretation of the nucleation and growth mechanism is evaluated using current-time curves produced from chronoamperometry.

Table 5.2 , the growth mechanism studies of the deposition at an optimum potential (-1.1 V) is done. The nucleation process causes a peak in current density, which is followed by a dip, indicating that diffusion-controlled growth is prevailing. Initially, a substantial declining current is observed due to adsorption-desorption processes following the results published by Scharifker and Hills (14).

The dimensionless plots $(j/j_m)^2$ vs (t/t_m) obtained from experimental data for CdS are compared with the theoretical curves calculated using equations (5.5) and (5.7) for instantaneous and progressive nucleation proposed by the Scharifker-Hills model for a more accurate

interpretation of electrocrystallization (14). Figure 5.4b depicts the $(j/j_m)^2$ vs (t/t_m) curves of CdS at -1.1 V, revealing that the rising component of the experimental curves is in strong connection with the theoretical progressive nucleation (black line) for CdS, consistent with previous findings (15, 16). Using equation (5.8), the number density of active sites AN_0 for CdS is calculated to be 1.6×10^{13} $cm^{-2}s^{-1}$.

For instantaneous nucleation:

$$\frac{j^2}{j_{max}^2} = 1.9542 \left(\frac{t_{max}}{t}\right)\left[1 - exp\left(-1.2564\frac{t}{t_{max}}\right)\right]^2 \quad (5.6)$$

Diffusion coefficient $D = \frac{j_m^2 t_m}{0.1629\ (ZFC)^2}$

Number density of nucleation active sites

$$N_0 = \frac{1}{k}\left(\frac{j_m}{0.64ZFDC}\right)^2 \quad (5.7)$$

$$k = \sqrt{\frac{8\pi CM}{\rho}}$$

For progressive nucleation:

$$\frac{j^2}{j_{max}^2} = 1.2254 \left(\frac{t_{max}}{t}\right)\left[1 - exp\left(-2.3367\frac{t^2}{t_{max}^2}\right)\right]^2 \quad (5.8)$$

Number density of nucleation active sites

$$AN_0 = 0.2898 \left(\frac{\rho}{8\pi M}\right)^{\frac{1}{2}} C^{\frac{3}{2}} \frac{z^2F^2}{j_m^2 t_m^3} \quad (5.9)$$

Diffusion coefficient $D = \frac{j_m^2 t_m}{0.2598(ZFC)^2}$

where z is the electron transfer; F is the Faraday's constant (96500 C/mol); C is the bulk concentration in the electrolyte (molar); ρ is the density of the deposit(g/cm^3), and M is the molar mass of the deposits (g/mol).

5.2.4 Morphological Studies

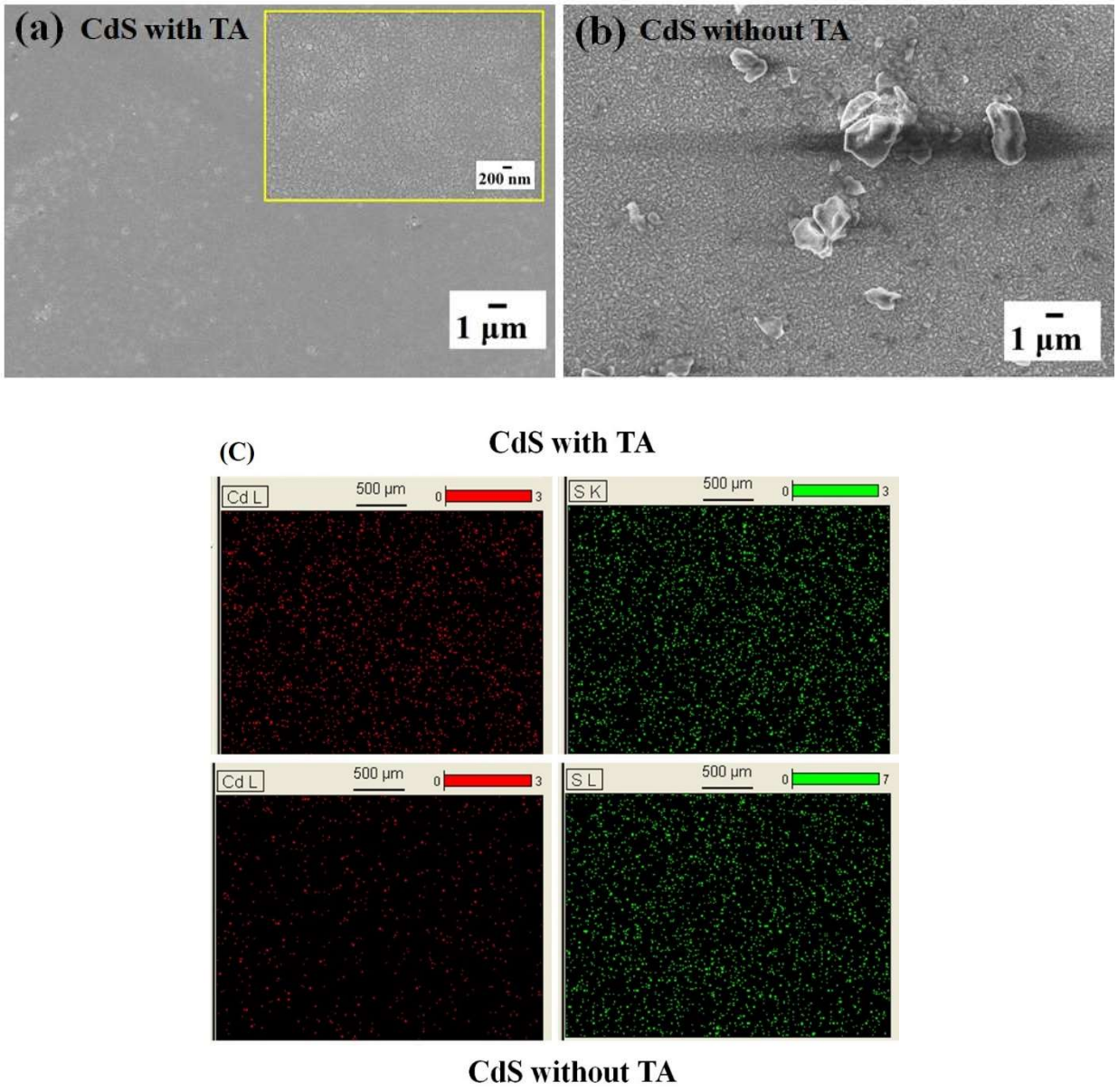

Figure 5.5: Surface morphology of (a) CdS deposited at -1.1 V with (inserted high magnification image) and (b) CdS deposited at -1.1 V without TA on FTO substrates (c) EDS mapping of CdS film with and without TA

Figure 5.5 depicts the surface morphology of CdS thin films deposited at -1.1 V and investigated using FESEM. The morphology of the films deposited in the presence of tartaric acid at greater magnification is depicted in the insets of Figure 5.5a for CdS. It clearly demonstrates aggregated flakes of CdS resembling flower-like structures with conformal coverage over the FTO

substrate. The occurrence of such grains deposited with tartaric acid at ambient temperature without post-heat treatment is intriguing, while previous research showed electrodeposited CdS with spherical grains (3). Similar morphology with cabbage-like features has been observed; however, deposited at 55-65°C with additional post-deposition heat treatment (17). Furthermore, the films formed in the absence of tartaric acid, as shown in Figure 5.5b, exhibit the underlying FTO substrate grains with distributed clusters of CdS.

Further, the results are consistent with the EDS map (**Figure 5.5**c) generated for the films deposited with and without the tartaric acid. It can be seen that in the absence of tartaric acid only adsorbed sulfur with little Cd. The elemental map of films then shows uniformly distributed CdS after addition of tartaric acid into the electrolyte, indicating a significant improvement in film composition. This is largely due to the tartaric acid-controlled pH dependence of film deposition, as well as its complexing ability with metal ions.

5.2.5 Impedance Measurements

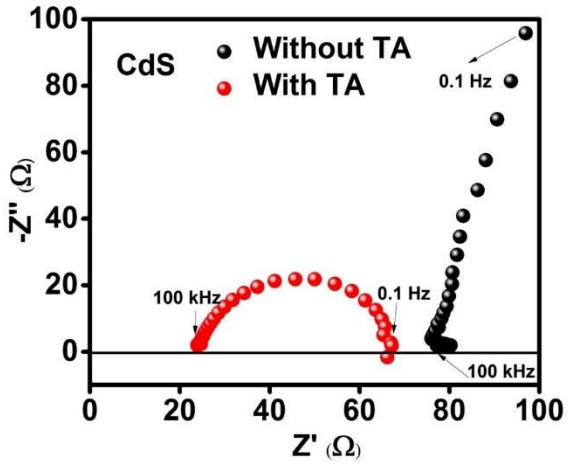

Figure 5.6: Nyquist plot measured during the deposition of (a) CdS at – 1.1 V with $CdSO_4$ + $Na_2S_2O_3$ + tartaric acid

CdS deposition is evaluated by electrochemical impedance spectroscopy (EIS) using $CdSO_4$ + $Na_2S_2O_3$ in tartaric acid. The study used a three-electrode system with an amplitude of 5 mV and a frequency range of 100 kHz to 0.1 Hz. The impedance data collected in this work is useful in assessing the interfacial events that occur during the deposition of CdS from a tartaric acid electrolyte. The Nyquist plots with real (Z') and imaginary parts (Z'') of CdS at the optimal

deposition potential with and without tartaric acid are shown in Figure 5.6. The curve obtained for CdS without tartaric acid had a twist at higher frequencies and then a straight line due to rapid diffusion and adsortion of the ions. This result is consistent with the morphological and EDS findings, which demonstrated that in the absence of tartaric acid, only adsorbed sulphur was present.

While there is a semicircle at a higher frequencies and an inductive loop due to relaxation at a lower frequencies for the tartaric acid assited electrodeposited CdS film. This sheds light on the creation of the metal complex, which has been discussed in previous studies (18). The presence of this curl indicates that CdS is formed via an intermediary metal tartrate complex. As a result, the complex's dissociated metal ions react with the sulfide ions to generate CdS. Furthermore, the plausible phenomenon underlying crystallisation may be attributed to the carboxylic groups detached from the metal tartrate complex serving as new active sites in addition to the existing ones, promoting nucleation and coalescence to form a crystalline thin film, as evidenced by previous works (15, 19).

5.2.6 Scanning electron microscopy (SEM)

Figure 5.7 depicts the surface morphology of CdS thin films deposited at -1.0 and -1.1 V, wherein Figure 5.7a and Figure 5.7e shows the surface morphology of as-deposited CdS films at -1.0 V, respectively. On the FTO substrate, as-deposited CdS films exhibit conformal coverage and uniform sized particles. High magnification FESEM images of as-deposited CdS films demonstrate a flower-like particle growth with flakes (Figure 5.7). CdS films have previously been observed to have flower-like morphologies (20). Figure 5.7b and Figure 5.7f depicts the annealed films in lower and higher magnifications. The annealed films, in addition to the as-deposited films, have flower-like particle shape. The flower-like form is helpful in solar cell applications because it promotes increased current carrier concentration, electron transmission, and hence photocurrent generation (21). Similarly, Figure 5.7c and Figure 5.7g show the surface grains of as-deposited films at -1.1 V, whereas Figure 5.7d and Figure 5.7h show the surface grains of annealed films. The morphology of both films formed at -1.0 V and -1.1 V deposition potentials shows comparable grains. In addition, homogeneous surface coverage of CdS films is obtained, which is critical for use in thin-film solar cells where the growth of top window layers is frequently impacted by the underlying buffer layer.

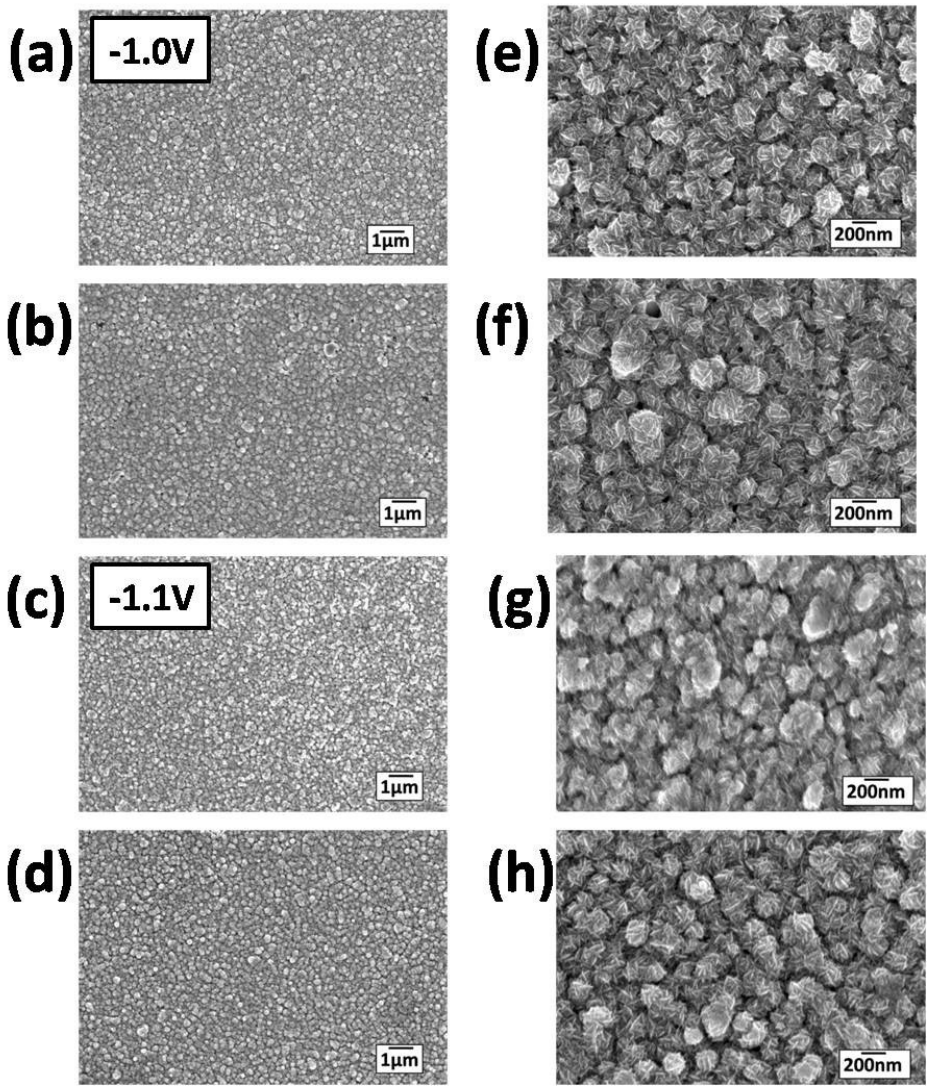

Figure 5.7: Surface morphology of CdS films deposited at various deposition potentials figure (a) & (e) shows the morphology of as deposited CdS films at -1.0V and fig (b) & (f) are the annealed samples at -1.0V figure (c) & (g) shows the morphology of as deposited CdS films at -1.1V and fig (d) & (h) are the annealed samples at -1.1V

The uniform pulse electrodeposited CdS films are predicted to aid in the smooth growth of window layers, reducing interfacial effects. The flower-like morphology establishes the junction between the internal flakes and electrolyte, thereby allowing to enhance the junction area and result in effective charge carrier generation and transport in photoelectrochemical water splitting, where CdS is one of the most attractive choices. Previously, similar morphologies for several materials were observed, which resulted in better photocurrent (22). It is also well known

that CdS films are frequently developed at higher temperatures (60 – 90 ºC) using various solution-based approaches to facilitate film growth. However, the pulse electrodeposition approach used herein has a larger throwing power, which increases the deposition rate while achieving uniform conformal coverage. Furthermore, the off-time in pulse electrodeposition works as relaxation time between succeeding periodic depositions, assisting in the re-arrangement of adatoms, resulting in the formation of new nucleation sites and uniform and adherent coatings. As a result, to make stoichiometric homogeneous CdS films with flower-like particle shape, a pulse electrodeposition technique with an appropriate deposition potential, duty cycle, and deposition time is applied.

5.2.7 Structural Analysis

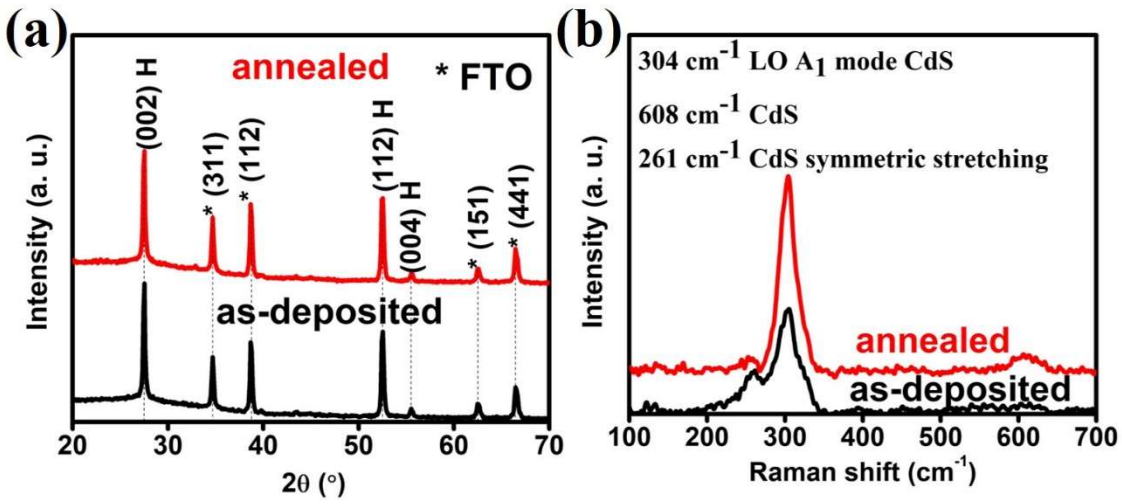

Figure 5.8: (a) XRD patterns (b) Raman Spectra for as-deposited & annealed CdS films deposited at -1.1V for 20 min

Figure 5.8a shows the XRD patterns of as-deposited and annealed pulse electrodeposited CdS thin films deposited for 20 minutes at a potential of -1.1 V. XRD patterns show a main peak with a preferred orientation to (002) and additional peaks for (112) and (004) planes, which match to hexagonal polycrystalline CdS. (JCPDS file 04-014-1049). Peaks at 2θ values of 34.6, 38.7, 62.5, 66.5 with planes (311), (112), (151) and (441), indicates the underlying FTO substrate (JCPDS diffraction file 04-014-0699). From **Figure 5.8**a, the as-deposited and annealed CdS films exhibit similar XRD patterns, with the ratio of prominent (002) peak intensity being nearly equal to one. This fact confirms that as-deposited films compete with annealed films in nature and are extremely crystalline. An interesting aspect, is the detection of a pure hexagonal phase for CdS,

as opposed to prior reports, which frequently reported mixed hexagonal and cubic phases. Murali et al reported cubic CdS in as-deposited films employing pulse plating, which was converted to the hexagonal phase when annealed at high temperatures (70-80 °C) (23). In the current study, the complexation effect of metal ions is demonstrated by carboxylic groups trapped between the electrolyte and deposited species, which act as kink sites for grain nucleation, resulting in grain refining to form nanostructured grains and hexagonal phase formation at room temperature without any further heat treatment.

Micro-Raman analysis is another qualitative characterization technique for identifying phases that can be used to support the XRD results. In Raman analysis, microscopic focusing with a spatial resolution less than1 μm^2 aids in the detection of any surface dispersed undesirable phases while also determining the crystallinity of films. Specifically, due to the small variance in 2θ values of CdS and FTO planes in XRD, distinguishing phases in CdS films deposited on FTO substrates is relatively challenging. In such instances, Raman spectroscopy is an effective tool for differentiating and identifying the phases. **Figure 5.8**b, shows micro-Raman spectra of pulse electrodeposited and annealed CdS films with well-defined CdS peaks at a Raman shift of 261 cm^{-1} corresponding to CdS symmetric stretching mode and 304 cm^{-1} assigned to longitudinal optical (LO) A1 mode (24). In addition, the second harmonic of the A1 mode may be seen at 608 cm^{-1}. Thus, Raman analysis confirmed the presence of hexagonal CdS phase in as-deposited and annealed pulse electrodeposition samples, corroborating with XRD investigations.

5.2.8 Optical and Electrical Properties

UV-VIS-NIR spectrophotometry is used to investigate the optical characteristics of pulse electrodeposited CdS films. Figure 5.9a, reveals the transmittance spectrum of optimized pulse electrodeposited CdS films of 70 nm thickness, revealing an average transmittance of 79 % in the visible range, which satisfies the criteria for application in solar cells (25). The bandgap of pulse electrodeposited CdS films is obtained from Tauc's plot using equation

$$\alpha h\upsilon = A(h\upsilon - E_g)^m \quad (3.20)$$

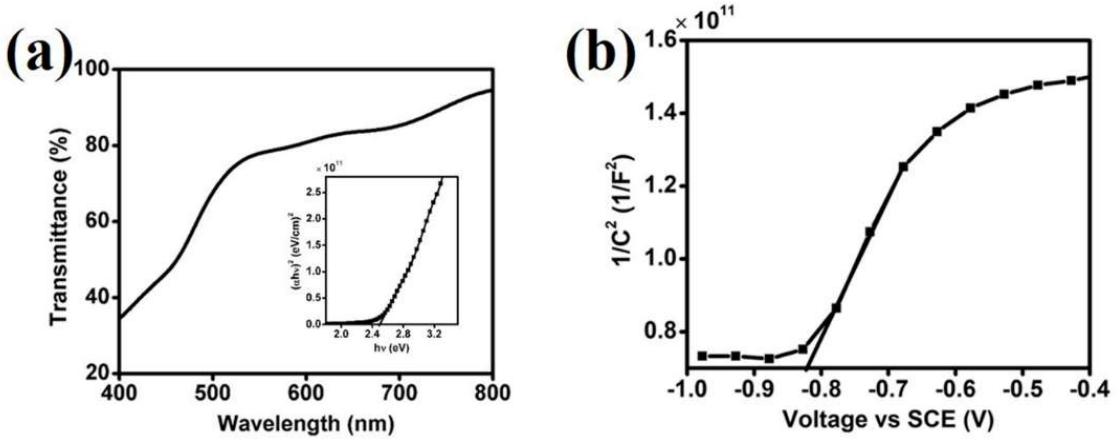

Figure 5.9: (a) Transmittance spectrum (Inset: Tauc's plot) and (b) Mott-Schottky curve of the CdS thin film at -1.1 V deposition potential for 20 min

The bandgap is calculated by extrapolating the linear section of the curve to the x-axis from Tauc's plot (inset of Figure 5.9a), to be ~ 2.4 eV, which agrees well with earlier values reported for CdS films used in thin films solar cells (26). It is observed from other studies that most as-deposited films possess narrow bandgap due to excess sulfur as impurity. While higher bandgap such as 2.8 eV is observed for films with excess oxygen as impurity forming CdS:O (27). In the work presented here, promising results are achieved where the as-deposited films showed 2.4 eV indicating pure CdS formation without secondary phases.

The Mott-Schottky (MS) study of pulse electrodeposited CdS thin films is performed using electrochemical impedance investigations to identify the nature of conductivity, flat-band potential, and carrier density. The following Mott-Schottky equation relates capacitance and applied voltage across a semiconductor in an electrolyte:

$$\frac{1}{C^2} = \frac{2}{\varepsilon\varepsilon_0 A^2 e N_D}\left(V - V_{fb} - \frac{k_B T}{e}\right) \tag{3.14}$$

where ε_o is the permittivity in vacuum, ε is the dielectric constant of semiconductor, A is the active surface area of semiconductor, e is the electron charge, E is the applied potential, N_D is the donor density of semiconductor, E_{fb} is the flat-band potential, k is the Boltzmann constant and T is the room temperature. Figure 5.9b shows the MS plot of pulse electrodeposited CdS films which are recorded in 0.5 M Na_2SO_4 electrolyte at a scan rate of 10 mV/s at frequency of 10 kHz in dark. The positive slope of the curve indicates n-type conductivity in CdS films, but extrapolating the

linear fit of the region seen in Figure 5.9b to the x-axis yields the flat-band potential, which is calculated to be -0.82 V vs SCE. The slope of the curve indicates that the carrier density of CdS films is approximately 8.5×10^{18} cm^{-3}. The flat-band potential and carrier density found herein are consistent with previous values reported for CdS films (27).

5.2.9 Photoelectrochemical Performance of CdS Deposited at Various Durations

5.2.9.1 Composition and Surface morphology of CdS Thin Films

Table 5.3: Composition and thickness of as-deposited CdS thin films deposited using a potential of -1.1 V with variation in deposition time obtained from energy dispersive X-ray spectroscopy and stylus profilometry

Deposition time (min)	Composition (at. %)		Cd/S	Thickness (nm)
	Cd	S		
5	33.5	66.5	0.50	20
10	46.7	53.3	0.87	40
15	44.4	55.6	0.79	60
20	47.0	53.0	0.88	70
25	43.4	56.6	0.76	90

The thickness of the films deposited is observed to be proportional to the deposition duration. Further, it is necessary to consider the thickness of CdS films in addition to their stoichiometry because it is an important aspect for use in thin-film solar cells. It is commonly known that for high efficiency solar cells, thickness is in the range of 60 – 70 nm. Hence, in the current work, thickness is controlled by altering the deposition time while maintaining the deposition potential constant at -1.1 V. Figure 5.3b depicts the visual appearances of CdS films deposited at -1.1 V with different deposition durations, and

Table **5.3** displays the relative compositions of CdS films.

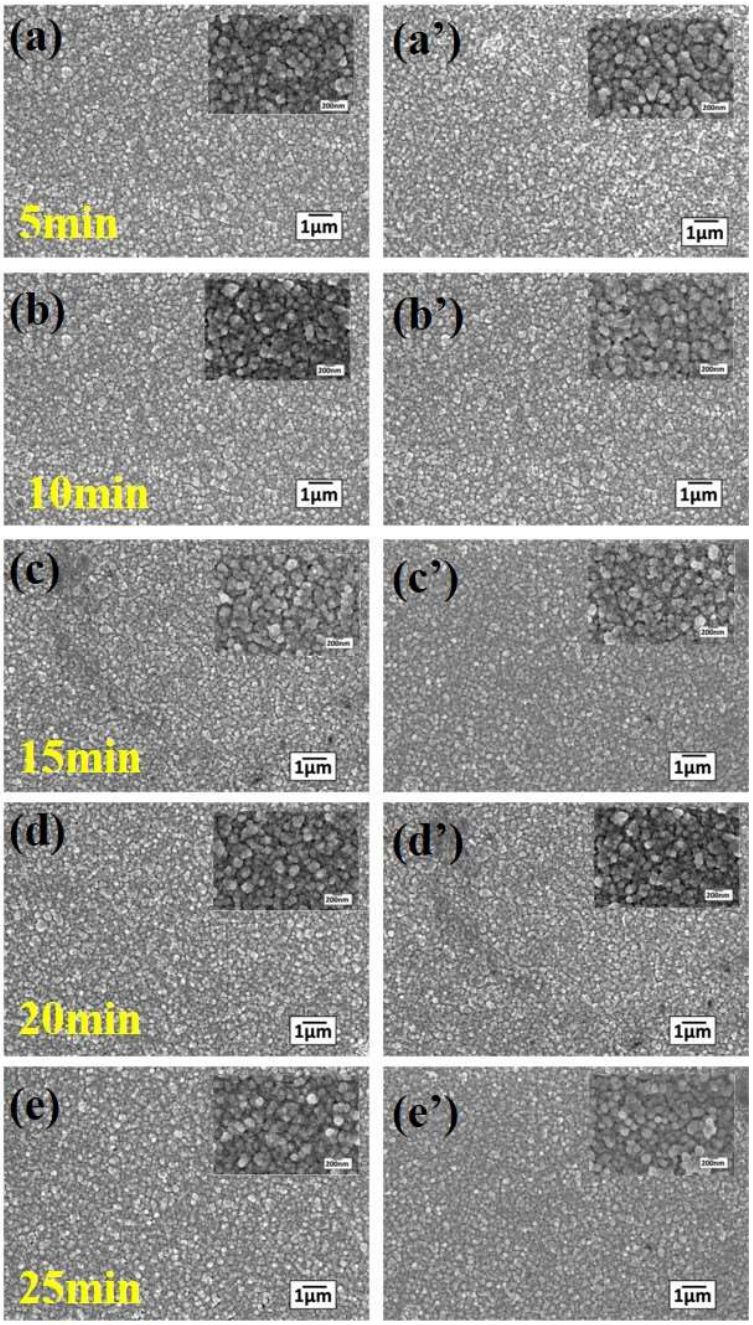

Figure 5.10: Surface morphology of (a) to (e) as-deposited CdS films (a') to (e') annealed films at -1.1 V at various durations

An intriguing component of the compositional investigations is the increased sulfur content for shorter deposition times compared to Cd, showing that cathodic reduction of sulfur occurs prior to Cd electroreduction, which is consistent with previous reports (28). The relative concentrations

of Cd and S appear to be close to the intended values for a deposition duration of 20 minutes, with a Cd/S ratio of 0.88.

Table **5.3** presents the thickness values of electrodeposited CdS films calculated using stylus profilometer. The thickness of CdS films increases with deposition time, as expected, and a value close to 70 nm is reported for films deposited for 20 minutes. Hence, a potential of -1.1 V and a duration of 20 minutes are found to be ideal for pulse electrodeposition of CdS films. However, as shown in **Figure 5.10** there is negligible difference in surface shape for films produced at varied deposition durations. Figure 5.3c a photograph of CdS films deposited on a large area (~ 20 cm^2) FTO substrate, demonstrating the feasibility of the pulse electrodeposition technique for large area CdS film deposition.

5.2.9.2 Optical and Electrical Properties

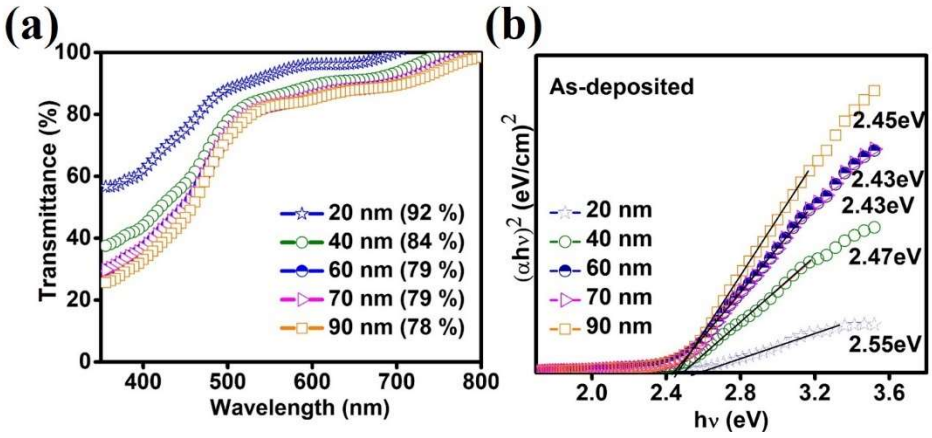

Figure 5.11: (a) Transmittance (b) Tauc's plot of CdS films with various thickness

The results presented above suggest profound changes in transmittance values with increase in thickness of the films. The reduction in the transmittance is observed with increase in the thickness of the CdS as shown in **Figure 5.11**a. However, negligible variation is observed in the band gap with the increase in the thickness of the films as seen in Tauc's plot of **Figure 5.11**b. At 20 nm thick film the bandgap is higher than theoretical value 2.4 eV which is indicative that the grain size could be extremely smaller as observed in quantum dot formation (29). This can also be the reason for higher transmittance of the film compared to other films.

Table 5.4: Variation of flat band potential and carrier density with different thickness of CdS thin films

Thickness (nm)	Flat band potential (V) vs SCE	Carrier density ($\times 10^{18}$ cm^{-3})
20	-0.63	7
40	-0.63	4
60	-0.63	7
70	-0.82	8
90	-1.0	10

It is also pertinent to note that flat band potential increases linearly with the thickness of CdS films as given in Table 5.4. As discussed in the optical properties the formation of extremely smaller grains resulted in higher carrier density in the very thin films such as 20 nm. Duty cycle of electrodeposition play an important role in depositing extremely thin films with smaller grains. The rearrangement phenomenon of adatoms during pulse off time favors in producing uniformly distributed flawless grains (30). The increment in the flat band potential is indicative of providing excess number of electrons as carriers for the pn junction formation. The formation of CdS nanocrystals favors in increasing the surface area for the photoelectron's separation and transfer.

5.2.9.3 Photoelectrochemical Measurements

CdS thin films are tested in 0.03 M sodium sulfite + 0.1 M sodium sulfide for their photoelectrochemical properties. The PEC study indicates the formation of pn junction between the thin film and the electrolyte which is the solid-liquid pn junction. This phenomenon helps in understanding the ability of the thin film to form the pn junction prior to its usage in the device fabrication (31). This electrolyte combination is a potent hole scavenger for photogenerated holes, reducing the effect of photocorrosion (32). PEC J-V characteristics for as-deposited CdS films are shown in Figure 5.12a using a scan rate of 10 mV/s under dark and light conditions. The shape of the curves indicates n-type conductivity of CdS, whereas the difference between dark and under illumination conditions indicates photoactivity. During the measurements in dark, an interfacial zone forms between the electrode and electrolyte where the Fermi levels are equilibrated, resulting in very little dark current. However, in this scenario, dark current increases in the positive potential zone, which is attributed to corrosion of electrode due to photogenerated charge carriers. Under

illumination, excited electrons from CdS conduction band reach the electrode-electrolyte interface, where they are devoured by protons and converted into hydrogen via photoelectrochemical water splitting, resulting in enhanced photocurrent.

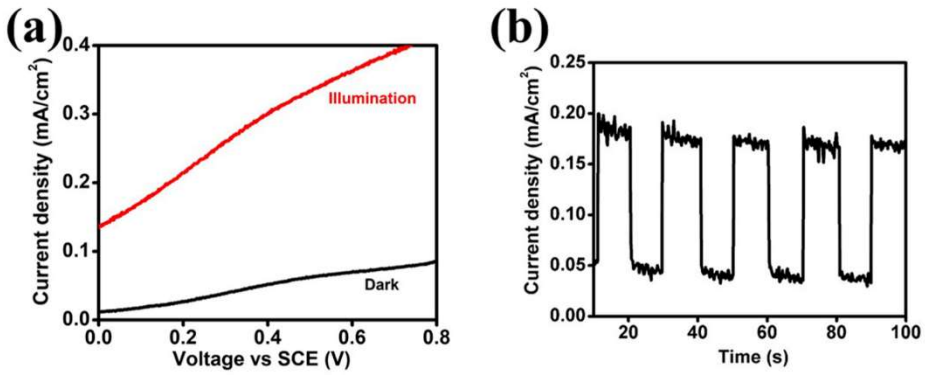

Figure 5.12: (a) J-V curves of as-deposited 70 nm thick CdS thin film under dark and illumination conditions (b) J-t curve shows the photocurrent of as-deposited CdS thin film at -1.1 V for 20 min

The photoresponse of as-deposited CdS films begins at a potential of -0.98 V, which is close to the semiconductor's flat-band potential, and a photocurrent density of 0.2 mA/cm^2 is recorded at 0.2 V versus SCE. The photocurrent density measured here for as-deposited CdS film of thickness 70 nm is equivalent to the values previously reported for annealed CdS films of higher thicknesses (100 – 200 nm) (33), showing that CdS performs very efficiently in the present study. The improved photoresponse is ascribed to the stoichiometric single phase hexagonal CdS with no cubic phase achieved by appropriately regulating pulse parameters during pulse electrodeposition with Tartaric acid as the complexing agent. the flower-like morphology with conformal coverage is advantageous in increasing optoelectronic properties such as current carrier concentration, electron transmission, and photocurrent production, leading in increased photoresponse (34). Obtaining amperometric J-t curves under chopped illumination confirms the photocurrent density of CdS films. The chronoamperometric J-t curve of as-deposited CdS films of 70 nm thickness measured at a constant potential of 0.2 V is shown in Figure 5.12b. The J-t curve confirms the photocurrent density of ~ 0.2 mA/cm^2 at 0.2 V vs SCE.

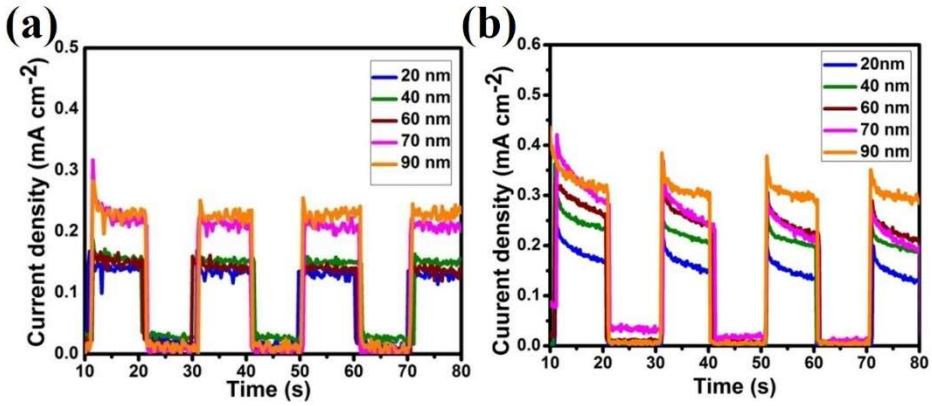

Figure 5.13: Photocurrent densities of CdS thin films deposited at -1.1 V varying deposition time (a) as-deposited (b) annealed

Figure 5.13a and Figure 5.13b shows the J-t curves of as-deposited and annealed CdS films, respectively. There is a surge in photocurrents as the thickness increases, indicating an increase in photon absorption at higher thickness. In addition, PEC analysis was used to analyze the annealed pulse electrodeposited CdS films, which showed similar photocurrent density values to as-deposited films, demonstrating the usefulness of as-deposited CdS films for use in thin film solar cells and photoelectrochemical cells.

5.2.10 Characterization of Electrodeposited CdS over CIGS/Mo

The buffer layer is essential in the creation of the *pn* junction for the solar cell. Chemical bath deposited CdS is most commonly employed as a buffer layer in CIGS thin film solar cells. Because they are thin film modules, the buffer layer that is deposited must be extremely thin while maintaining outstanding homogeneity and optical qualities. This characteristic is critical for forming a better pn junction, which improves device performance. The CIGS device is fabricated using electrodeposited CdS in this study.

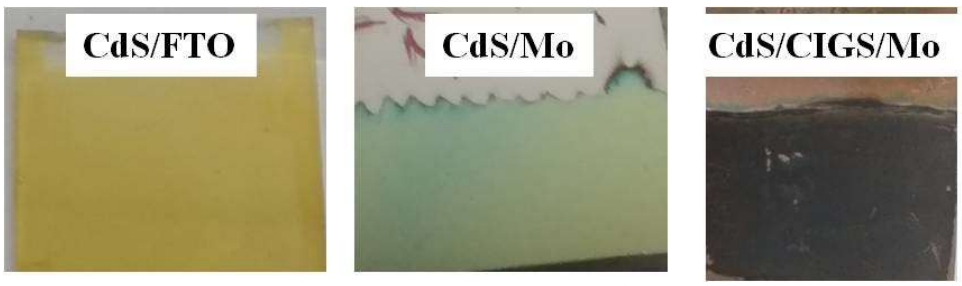

Figure 5.14: Visual appearance of CdS films on different substrates

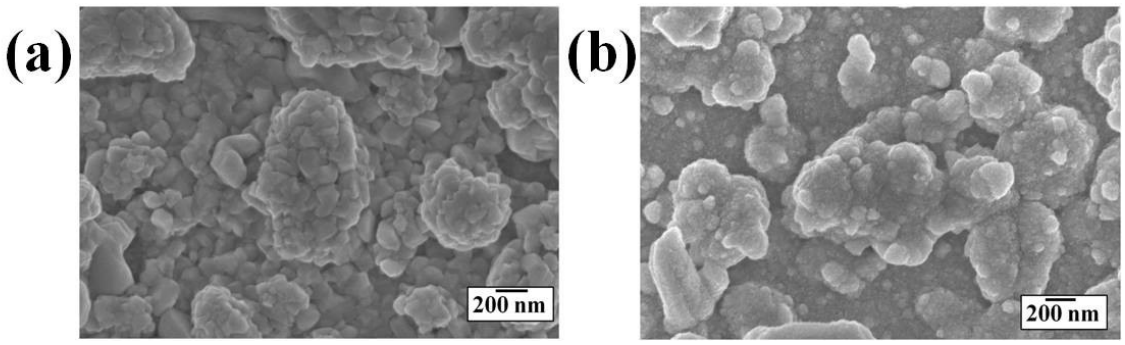

Figure 5.15: Surface morphology of (a) bare pulse electrodeposited CIGS/Mo (b) pulse electrodeposited CdS/CIGS/Mo

As seen from the physical appearance of the CdS films on FTO, Mo and Mo/CIGS (**Figure 5.14**), the films are uniformly coated with fine distribution at room temperature deposition. Further, Figure 5.15 shows the surface morphology of CIGS absorber before and after the electrodeposition of CdS. Figure 5.15a shows bare CIGS/Mo with grain sizes of around 160-200 nm and roughness is caused by the larger grains growing as the next layer on the compact grains. Figure 5.15b depicts the electrodeposited surface of CdS over CIGS/Mo, which is found to have conformal surface coverage with CdS grains of a few nanometers in size, resulting in a very little variation in surface morphology between CIGS and CdS/CIGS morphology. This demonstrates the potential utility of as-deposited CdS as a buffer layer in thin-film solar cell construction.

The interaction of ED-CdS film is explored under illuminated conditions and compared to typical CBD CdS prior to its insertion into the CIGS device. Figure 5.16a shows a photocurrent of 0.052 mA cm^{-2} with bare CIGS and Figure 5.16b shows an increase in photocurrent from (bare CdS/FTO) 0.186 mA cm^{-2} to (CdS/CIGS/Mo) 0.511 mA cm^{-2} at 0.2 V due to the creation of a pn junction. Under illumination, the photocurrent 0.511 mA cm^{-2} for ED-CdS and 0.636 mA cm^{-2} for CBD-CdS is detected from the J-V curves in Figure 5.16c indicating that electrodeposited CdS has photocurrent values similar to the typical CBD technique. Both films clearly demonstrated anodic current under illumination, which can be attributed to the films n-type behavior. The flat band potential calculated from the J-V curves is -0.8 V vs SCE. The electrodeposited CdS value agrees with the Mott-Schottky analysis result, and the CBD-CdS value is -0.7 V vs SCE. This demonstrates the advantages of employing as-deposited CdS thin films for device manufacturing, which are of comparable quality to those made by the CBD approach (35).

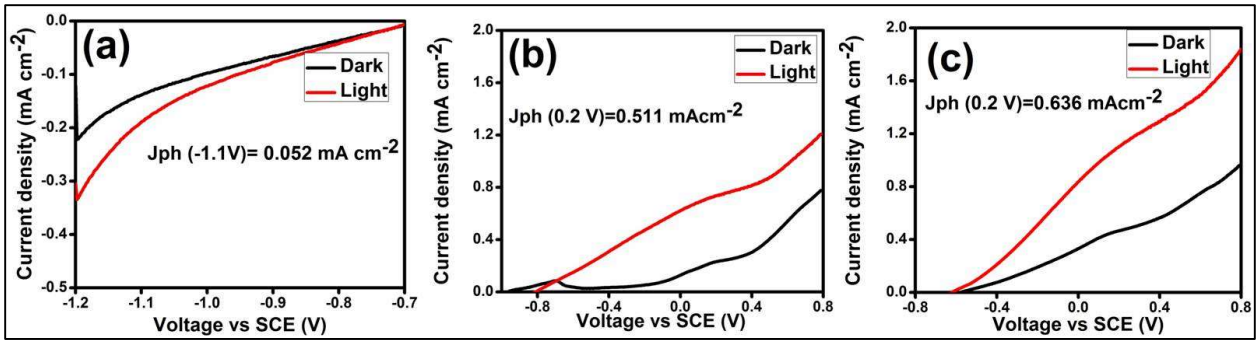

Figure 5.16: J-V curves of (a) bare CIGS (b) ED-CdS/CIGS (c) CBD-CdS/CIGS

5.2.11 Pn Junction Formation of CIGS/CISe Absorbers with Electrodeposited CdS

The fabrication of the CIS device is fabricated using successive layers in which 60nm of CdS deposited using electrodeposition and approximately 900-1000 nm of AZO/ZnO is deposited via RF sputtering. When compared to single layers of Cu/In deposited, the thickness of the absorber layer is significantly increased with multiple layers. The sequential deposition of Cu/In in multiple layers with increased off-time during pulse plating tends to be a diffusion controlled deposition process. In this scenario, the relaxation time increases the metal ions concentration in the diffusion layer of the electrode, facilitating the formation of large grain size with fewer grain boundaries(6).

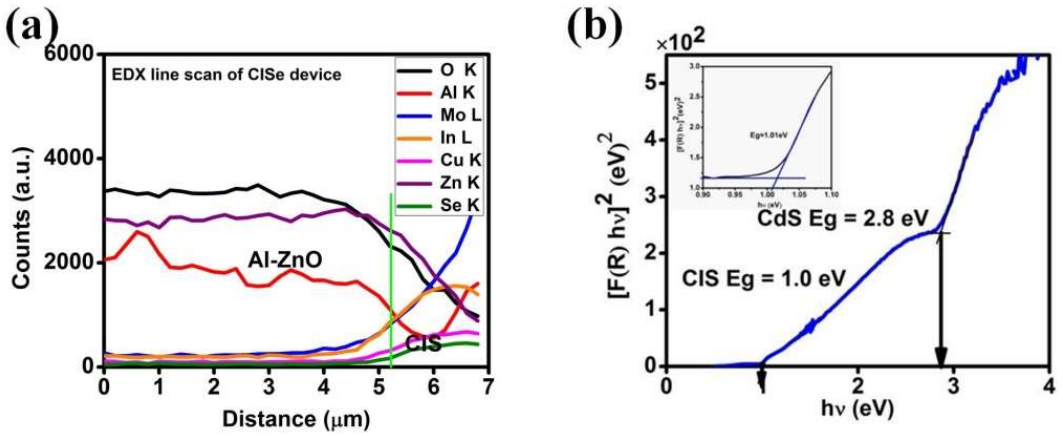

Figure 5.17: (a) Line scan of CIS device (b) Tauc's plot of ED-CdS/ED-CIS/Mo

The line scan data of the CIS device revealed that the CIS generated is slightly indium rich, as shown in Figure 5.17a, with high indium counts towards the molybdenum substrate. The counts, however, dropped to zero in the TCO layer region. Figure 5.17b depicts a Tauc's plot of ED-

CdS/ED-CIS, exhibiting the absorption edges of both layers with a band gap of 1.0 eV for CIS and 2.8 eV for CdS.

5.3 PART B: Electrodeposition of ZnS Thin Films at Room Temperature

Zinc sulfide (ZnS) is one of the most versatile semiconductor materials, with a wide bandgap (3.3 – 3.8 eV), due to its exceptional luminous characteristics. LEDs, Bio-LEDs, electroluminescence devices such as backlights in gadgets, soft robotics, artificial skin actuators, wearable electronics, are other applications (36, 37). Because of its catalytic properties, ZnS is also a promising choice for the removal of toxic waste from polluted water and the degradation of ethanol for fuel cells. Its optoelectronic properties, which have been extensively researched in the literature, are particularly intriguing, and include flat panel displays, infrared windows, sensors, and lasers (38). With an emphasis on Cd-free CIGS solar cells, ZnS is the best choice among thin-film photovoltaics due to its large bandgap compared to CdS, which has a tiny bandgap of ~ 2.4 eV. Although CdS is the most commonly utilized buffer layer, the chemical bath deposition (CBD) procedure used to deposit it produces a large amount of waste containing Cd, which is toxic and carcinogenic, posing a risk to the environment. As a result, it is vital to reduce/replace Cd in electronics as a preventative measure to safeguard the environment (39, 40). Furthermore, the most dependable technique to improve the power conversion efficiency of CIGS thin-film solar cells is to construct a heterojunction with negligible absorption losses. This can be performed by replacing CdS with a semiconductor material having a broad bandgap, such as ZnS, SnS, ZnSe, and In_2S_3 (41). Among these, ZnS is regarded as an environmentally acceptable semiconductor composed of earth-abundant and non–toxic components. Due to its wide bandgap, it exhibits a large increase in photon transmission in the visible (400-500 nm) range, resulting in a rise in short-circuit current density, and hence is a better alternative to replace CdS (42).

Fundamentally, ZnS crystallizes in cubic and hexagonal configurations, and it is worth noting that cubic ZnS has a lattice parameter of 5.4 A°, which corresponds well with that of CIGS (5.6 A°), and is thus more suitable for CIGS thin film solar cells (43). For the deposition of ZnS thin films, many known technologies such as chemical bath deposition (CBD) (42), spray pyrolysis (43, 44), RF sputtering (45), atomic layer deposition (46), electrodeposition (ED), and others are used (35, 47, 48). CBD is a popular choice among them, and the production of Zn (O, S) has been observed. Despite the presence of oxygen, the devices created have demonstrated

outstanding efficiency due to their 3.2 eV bandgap. Nakada et al investigated CBD-ZnS and found an efficiency of 18.6 % for CBD-ZnS(O, OH) and 18 % for CBD-ZnS employing CIGS absorbers made using the co-evaporation process (42, 49). Motoshi et al. recently achieved the best efficiency of 23.35 % for Cd –free CIGSSe solar cells by replacing CdS/ZnO layers with Zn(O, S, OH) formed using CBD (50). Aside from the CBD technique, electrodeposition is a low-cost method for producing ZnS films. There are, however, very few studies on electrodeposited ZnS films for solar cell applications (35, 51). It is worth noting that electrodeposition is a practical method for producing crystalline, smooth, and uniform thin films by effectively managing the growth conditions.

In several cases, electrodeposition is a low-temperature method that reduces metal interdiffusion and controls the thickness and characteristics of the deposited films using pulse parameters as well as deposition potential/current, temperature, agitation, and complexing agents (52, 53). Sanders et al. are the first to report the electrodeposition of ZnS using glycerol in acidic solutions, resulting in ZnS films with an irregular grain distribution and cubic phase (200) orientation on an ITO substrate (54). A duty cycle effect study revealed variations in the bandgap of ZnS films formed by galvanostatic pulse electrodeposition at room temperature (55). Other publications on pulse electrodeposition at high temperatures have revealed cubic (200) and hexagonal (002) ZnS, with sodium thiosulfate serving as a sulfur precursor (56, 57). On the other hand, depositions at elevated temperatures utilising ammonium thiosulfate as a sulfur precursor resulted in ZnO impurities (58). Therefore, it is concluded that the choice of precursors can have an adverse influence on the formation of phase pure ZnS. Alkaline electrolytes are also being investigated in order to minimise the quick precipitation of sulfides, which has resulted in the creation of ZnO in addition to ZnS. As a result, it is clear that deposition in acidic solutions increases the synthesis of ZnS while suppressing the oxides (59). Another interesting study examined the effect of precursor concentrations on n-type ZnS from zinc-rich electrolytes and p-type ZnS from sulfur-rich electrolytes with extra heat treatment (60). Thus, the post-deposition treatment had a good impact on the optical and electrical properties of these ZnS films (58, 61). Dharmadasa et al attempted to use electrodeposited ZnS in thin film solar cells, wherein 3-layered graded-bandgap CdTe solar cells (Au/CdTe/CdS/ZnS/FTO/glass) improved the J_{sc} and were more productive than the traditional ones (Au/CdTe/CdS/FTO/glass) due to a broad and healthier depletion area (35). CIGS solar cells, on the other hand, are substrate-configured and so require

extreme caution in producing a good pn junction by electrodeposition. However, previous research on ED-ZnS has relied on either high temperature (~ 80-90 °C) during deposition or a post-annealing process to achieve the requisite characteristics.

In this context, the current method proposes a pulse electrodeposition method for ZnS at room temperature by conveniently modulating the pulse parameters as well as tartaric acid's complexing ability and glycerol's inhibitor property in order to achieve desired structural, optical, and photoelectrochemical properties. The significance of pulse plating in achieving higher optical characteristics is explored. The beneficial role of glycerol in restraining impure phases and favoring pure ZnS at room temperature is discussed. For the first time, the deposited films are used to build Cd-free CIGS devices, and the device demonstrates photovoltaic activity.

5.3.1 Pulse Electrodeposition of ZnS

5.3.1.1 Linear Sweep Voltammetry Studies

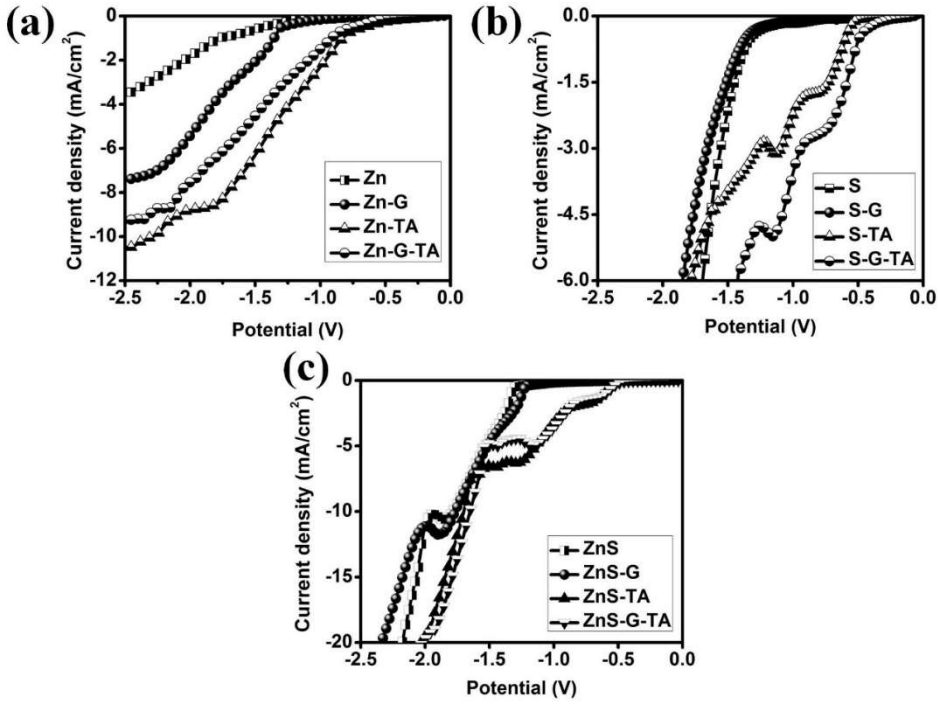

Figure 5.18: LSV curves of (a) Zn precursor (b) sulfur precursor (c) Zn + S precursors with and without tartaric acid and glycerol

Linear sweep voltammetry (LSV) is used to examine electrochemical reactions by understanding the range of elemental reduction potentials. Scanning is carried out in this study with potentials between 0 and -2.5 V at a sweep rate of 10 mV s^{-1}. The current-potential curve reveals details regarding the electron transfer process, adsorption events, and the effect of complexing agents. Thus, the current – potential curves aid in determining the multi-element system's reduction potentials. Figure 5.18 depicts a linear sweep voltammogram recorded with a two-electrode system to investigate the electrochemical behavior of Zn, S, and Zn-S in the presence and absence of tartaric acid (TA) and glycerol (G). Unless otherwise specified, the precursor concentrations used for LSV are the same as those used for depositions. The LSV curves for Zn precursor ($ZnSO_4.7H_2O$) with and without glycerol and tartaric acid are shown in Figure 5.18a. The current response of a bare Zn electrolyte with a pH of 6.7 is modest, indicating a negligible reduction of Zn^{2+} at higher pH or due to the electrolyte's poorer ionic conductivity. When glycerol is added to Zn precursor (Zn + G) (pH 4.5), a broad peak form between -1.5 and -2.2 V due to strong H_2 evolution and a weak reduction of Zn^{2+} ions. When tartaric acid is added to the bare Zn electrolyte (pH 2.5), the current density increases dramatically due to the complexation process between the Zn^{2+} ions dissociated from the precursor, as shown in (5.9 reaction), and tartaric acid, suggesting the creation of zinc tartrate, as shown in reaction 5.10 (62).

Furthermore, adding glycerol to the zinc precursor ($ZnSO_4.7H_2O$ + glycerol + tartaric acid) (pH 2.3) changes the reaction process in which glycerol combines with excess hydroxyl ions to create propane-1,2,3 triolate, as illustrated in reaction 5.11, avoiding the creation of the $[Zn(OH)_2]$ complex. The concentration of Zn^{2+} ions at the diffusion layer rises as a result of this event (63). The LSV curves of $Na_2S_2O_3$ (S), with and without glycerol (G), and tartaric acid are shown in Figure 5.18b (TA). At pH 7.0, the LSV response of S and S + G exhibits hydrogen reduction with no noticeable conversion of thiosulfate to sulfide ions and no increase in peak current even after the addition of glycerol (pH ~7.3), showing that the dissociation of sulfide ions from thiosulfate is low. However, the LSV response of the electrolyte to thiosulfate + tartaric acid (S + TA) and thiosulfate + glycerol + tartaric acid (S + G + TA) (pH~ 3) reveals an increase in peak current due to the disproportionate conversion of $S_2O_3^{2-}$ to H_2S at potentials -0.7 V and -1.1 V in both cases. As seen in Equations 5.12, 5.13, this suggests that the reaction is a two-step process. As a result, at lower pH, the dissociation of $S_2O_3^{2-}$ rises, providing enough sulfide ions for ZnS formation. However, the precipitation of sulfides is also rapid in acidic pH which is limited in this case due

to tartaric acid as its dissociation constant (pK_a ~ 3.0) is comparatively higher than that of the strong acids (47).

Figure 5.18c depicts the reaction kinetics associated with Zn and S precursors in the presence and absence of glycerol and tartaric acid. The current response for the bare Zn + S and Zn + S + G electrolytes is comparable, with notable reduction peaks at - 2.0 V correlating to zinc deposition at higher cathodic potentials. The small increase in peak current observed following the addition of glycerol to the Zn + S (pH 6.4) indicates the synthesis of propane-1,2,3 triolate (63). This is illustrated in Figure 5.19 where the production of $Zn(OH)_2$ is suppressed by the consumption of excess hydroxyl ions present in the electrolyte. This event promotes the concentration of Zn^{2+} ions at the electrode's diffusion layer. Moreover, when tartaric acid was added, the pH of the solutions (Zn + S + TA and Zn + S + G + TA) was substantially decreased to 2.5, with notable peaks between -1.2 V and -1.5 V for ZnS formation, which colored the substrates brown during the LSV. Although sulfide precipitation is quick at acidic pH, it is slowed in this case by tartaric acid, whose dissociation constant (pKa 3.0) is higher than that of the strong acids (19). The overall deposition involves a two-step electrochemical process that involves the creation of zinc tartrate complexes as indicated in the reaction mechanism of **Figure 5.19** and subsequently the formation of ZnS as described in 5.14 by the reaction of Zn^{2+} with the available sulfide ions. Thus, the mixture of Zn + S + G + TA not only regulates the rapid dissociation of thiosulfate to sulfide ions, but it also promotes ZnS formation at low cathodic potentials (64). The broad peaks indicate adsorption-induced underpotential deposition, and a little rise in negative potentials causes phase change. The reason for this could be that the drop in acidic pH favors tartrate ion adsorption and desorption in both cases of Zn + S + TA and Zn + S + G + TA. **Figure 5.19** depicts the action of tartaric acid in the deposition of ZnS schematically.

$$ZnSO_4.7H_2O \rightarrow Zn^{2+} + SO_4^{2-} + 7H_2O \quad (5.10)$$

$$Zn^{2+} + C_4H_6O_6 + 2OH^- \leftrightarrow [ZnC_4H_4O_6]^{2+} + 2H_2O + 2e^- \quad (5.11)$$

$$C_3H_8O_3 + 3OH^- + 3e^- \rightarrow [C_3H_5O_3]^{3-} + 3H_2O \quad (5.12)$$

$$S_2O_3^{2-} + 2H^+ \rightarrow S_{(\downarrow)} + H_2SO_3 \quad (5.13)$$

$$S_{(\downarrow)} + H_2SO_3 + 2e^- \rightarrow H_2S_{(ads)} + SO_3^{2-} \quad (5.14)$$

The overall reaction of ZnS deposition follows as

$$Zn^{2+} + S_2O_3^{2-} + 2e^- \rightarrow ZnS + SO_3^{2-} \quad (5.15)$$

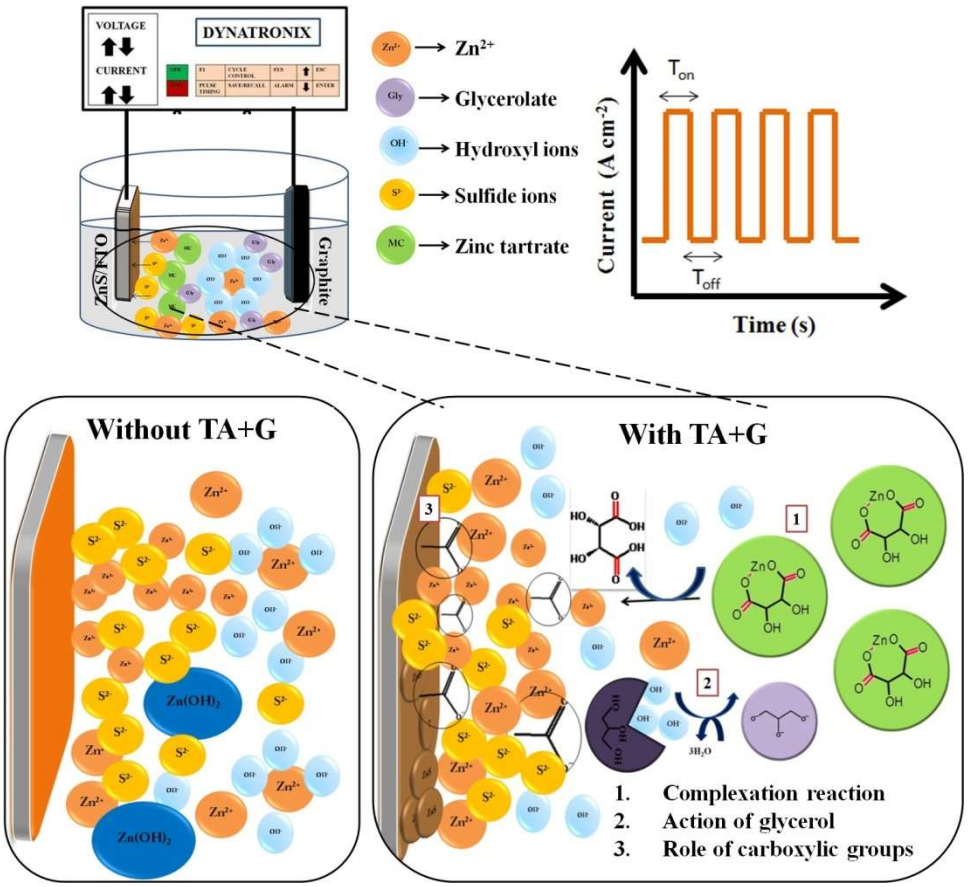

Figure 5.19: Schematic of reaction mechanism during ZnS deposition

5.3.1.2 Nucleation and Growth Mechanism of ZnS with the Aid of Tartaric Acid

The voltammogram of an electrolyte comprising $ZnSO_4$ + $Na_2S_2O_3$ + glycerol with and without tartaric acid at pH 2.5 and pH 6.4 is shown in

Figure **5.20**a. In the absence of tartaric acid, a distinct cathodic peak at -1.6 V is detected, which is expected due to the dominant Zn metal deposition. This is due to glycerol, which also controls the formation of $Zn(OH)_2$ and aids in the deposition of Zn. The atomic composition results in Table 5.5, support a higher incidence of Zn metal deposition. Further, in the presence of glycerol+tartaric acid, a shoulder peak at -0.9 and -1.7 V vs SCE appears, corresponding to the 2-step electrochemical process involving the metal complex 5.10 reaction generated with the Zn^{2+}

ions separated from the precursor reaction 5.9. Glycerol assures that excess OH- ions are reacted with OH- ions during this complexation process, avoiding the development of oxide impurities as seen in reaction 5.11. Moreover, as shown in reactions 5.12 and 5.13 the thiosulfate precursor reduces to sulfide ions, and as a result, when the potential scan is done beyond -1.3 V versus SCE, the substrates have turned brown, indicating the synthesis of ZnS.

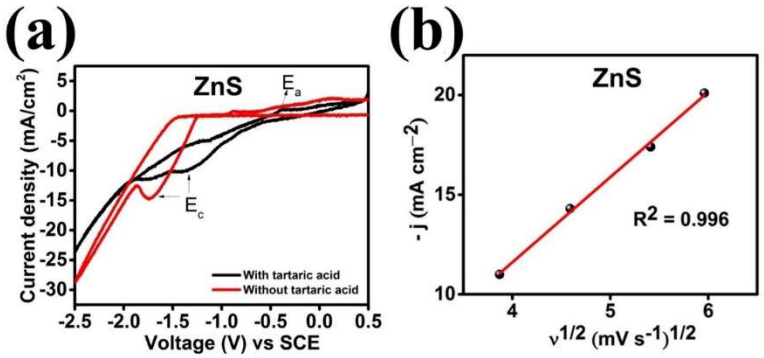

Figure 5.20: (a) Cyclic voltammograms of ZnS with and without Tartaric acid (b) Plot of square root of scan rate vs current density

Further, when the voltage was scanned to higher cathodic potentials, the substrate turned grey, possibly due to excess zinc deposition between -1.5 and -1.7 V vs SCE during the CV measurements (65). Although H_2 evolution coexists along the reduction peaks in the current study, it is found that the rate of hydrogen evolution is attenuated at the deposition potential window and is noticeable at higher cathodic potentials in both CdS and ZnS (66). It is also worth noting (**Figure 5.20**a) that in the anodic regime, there is a broad peak at -0.4 V vs SCE (Ea) due to the dissolution of excess zinc.(62). The measured elemental data of ZnS film deposited using tartaric acid (**Table 5.5**) revealed a Zn-rich composition, which is consistent with the above hypothesis. Based on these findings, pulse electrodeposition is used to adjust the stoichiometry of the films for both CdS and ZnS deposition. As previously stated, ZnS depositions are carried out with varying potentials (-1.1 V to -1.5 V). According to the compositional study performed by EDS measurements, the films deposited at - 1.4 V for ZnS had a near stoichiometric composition with a Zn/S ratio of 0.7, as shown in Table 5.6

Table 5.5: Composition of CdS and ZnS films deposited during cyclic voltammetry with and without tartaric acid at room temperature

Composition of films from cyclic voltammetry (at %)		
ZnS	Zn (%)	S (%)
Without tartaric acid	93	7
With tartaric acid	65	35

5.3.1.3 Optimization of Deposition Parameters

The elemental composition of ZnS films formed at various deposition potentials is determined by EDS measurements and presented in Table 5.6. At -1.3 V, there is a comparatively reduced Zn concentration with a Zn/S ratio of 0.5, resulting in insufficient ZnS formation at this potential. A significant rise in Zn content is noted at -1.4 V, with a Zn/S ratio of 0.7 obtained with an increase in zinc content as deduced from the LSV curves. This means that ZnS deposition is assumed to be caused by the combined effect of tartaric acid and glycerol, with increased availability of Zn ions, which agrees with the LSV data, where ZnS deposition is shifted to lower cathodic potentials when glycerol is added. Further at -1.5 V, deposition is slowed with a Zn/S ratio of 0.6 due to the dominant disproportionate reaction of thiosulfate, as well as presiding H_2 evolution, resulting in higher sulfur content. As a result, it is reasonable to choose -1.4 V as the appropriate potential for pulse electrodeposition of ZnS films, resulting in a greater Zn/S ratio (64).

Table 5.6: Elemental composition and optical properties of ZnS films deposited at various potentials

Deposition Potential (V)	**Composition (at. %)**		**Zn/S**	**Transmittance (%)**
	Zn	S		
-1.3	33.0	67.0	0.5	67
-1.4	42.0	58.0	0.7	58
-1.5	37.0	63.0	0.6	50

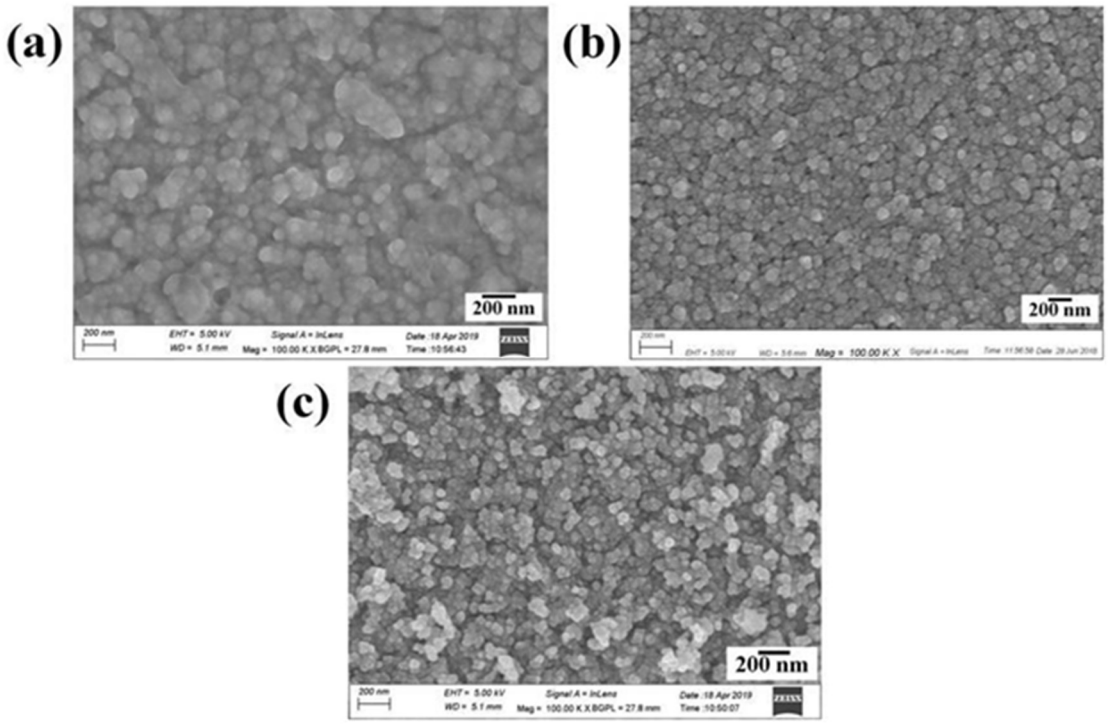

Figure 5.21: Surface morphology of ZnS/FTO (a) -1.3 V (b) -1.4 V(c) -1.5 V

Figure 5.21 illustrates the surface morphologies of ZnS films deposited at various deposition potentials. At -1.3 V, the agglomeration of grains is viewed. Excess sulfur deposition caused smaller grains scrambling to form clusters (**Figure 5.21**a). When the potential is increased to -1.4 V, the morphology of the film (**Figure 5.21**b) is found to be moderately smooth and compact, with spherical and well-defined grains and conformal surface coverage. Subsequently, the planar view of a -1.5 V ZnS film (**Figure 5.21**c) contains agglomerates of nanoscale particles with an uneven distribution, resulting in a rough surface. This could be because of excessive sulfur adsorption at extremely high cathodic potentials. Further, because ZnS is being made for a specific application as a buffer layer in thin-film solar cells, it is critical to monitor the transmittance in the visible region of solar spectrum. Therefore, **Table 5.6** provides the T % values determined for ZnS films deposited at various deposition potentials. It should be noted that films deposited at -1.3 V have a high T % of 67 %, indicating that they lack the requisite Zn/S ratio for use in solar cells.

Table 5.7: composition and optical results of ZnS thin films deposited at -1.4 V with varied duty cycles

Duty cycle (%)	Composition (at. %)		Zn/S	Transmittance (%)
	Zn	S		
85	64.4	35.6	1.8	75
75	55.7	44.3	1.2	71
66	39.1	60.9	0.6	69
60	20.6	79.4	0.2	65

The films formed at -1.4 and -1.5 V, on the other hand, have low T % values, which are not suitable. Therefore, further investigation into process parameter optimization is required to create ZnS with the necessary composition and optical characteristics. The results shown in **Table 5.7** disclose that altering the duty cycle (from 85 to 60 %) during pulse electrodeposition influenced both the composition and the transmittance of the films. It is observed that at 85 % duty cycle, the Zn/S ratio is around 1.8, indicating zinc-rich films, because the dissociation of zinc tartrate complex is quick due to high. $T_{on} >> T_{off}$. The film deposited at 75 % duty cycle with a slight increase in T_{off} had a higher sulfur content and a Zn/S ratio of 1.2. When the duty cycle is reduced further to 66 and 60 %, the deposited films are sulfur-rich, with Zn/S ratios of 0.6 and 0.2, respectively, as expected due to the prolonged relaxation time of the pulse plating, which facilitates colloidal sulfur accumulation at the diffusion layer.

In extension, **Figure 5.22** depicts the surface morphology of the pulse electrodeposited ZnS films at various duty cycles. As is seen in **Figure 5.22**a, the films at 75% duty cycle resulted in tightly packed grains with no voids or cracks and excellent surface coverage. In conjunction with the deposition at -1.4 V and a duty cycle of 75%, the available relaxation period contributes to metal ion buildup at the electrode and results in a significant reduction in grain size. The film exhibits spherical grains and porosity due to fast Zn deposition and strong H_2 development at 85 % duty cycle, with $T_{on} >> T_{off}$ (**Figure 5.22**b).

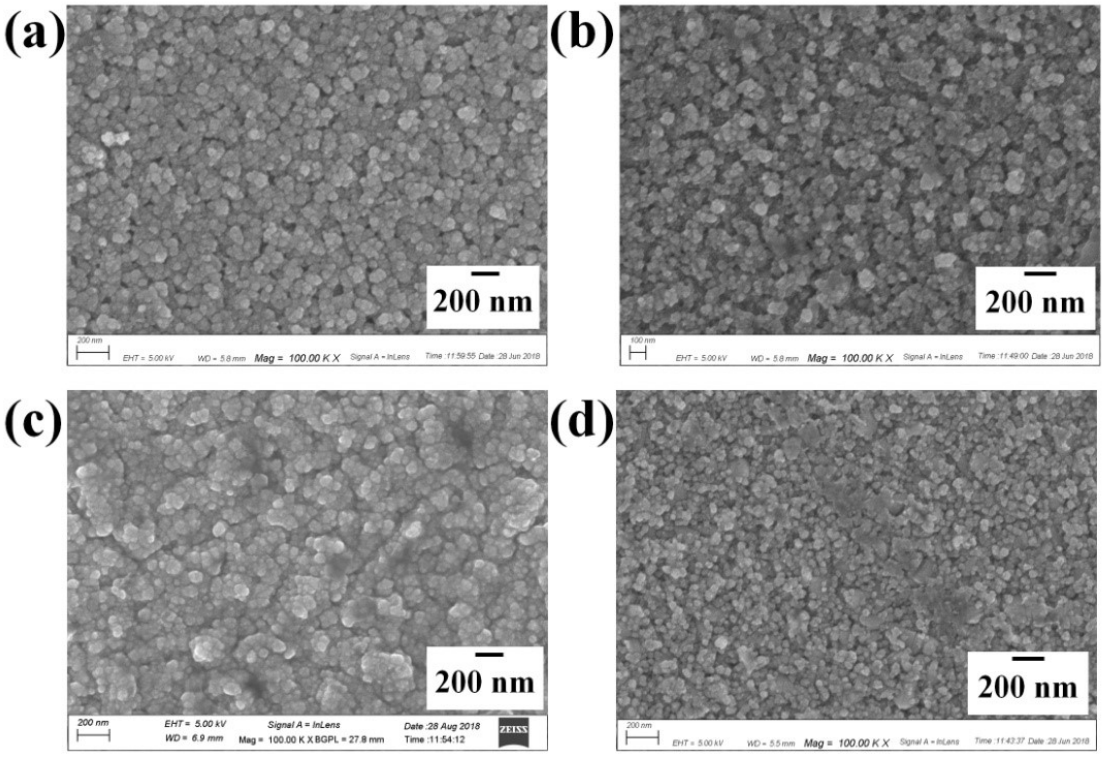

Figure 5.22: Surface morphology of ZnS/FTO thin films deposited at various duty cycles (a) 75 % (b) 85 % (c) 66 % (d) 60 %

The effect of duty cycle on grain growth is also investigated. Reduced duty cycle to 66 % (**Figure 5.22**c) resulted in a decrease in film smoothness due to increased sulfur deposition. Further, at 60 % duty cycle, there is an apparent uneven grain distribution in the films (**Figure 5.22**d) which is largely due to excess sulfur deposition. The films, however, are crack-free and moderately adherent even at greater cathodic potentials due to the pulse relaxation period, which promotes adatom rearrangement as compared to DC depositions (67). This implies that the role of duty cycle cannot be ignored in achieving films with optimal properties, and the observations from these results show that the film deposited at 75% duty cycle has significantly increased transmittance (71%) while maintaining the desired composition, as shown in **Table 5.6**

5.3.1.4 Chronoamperometric Studies.

It is imperative to understand the process of nucleation and growth of the ZnS for which the chronoamperometry studies are performed as an inference from the CV and LSV studies. At different deposition potentials, the J-t curves as seen in Figure 5.23a, revealed negligible currents

for the potentials at -1.1V and -1.2 V as no deposition occurs agreeing with the CV and LSV studies.

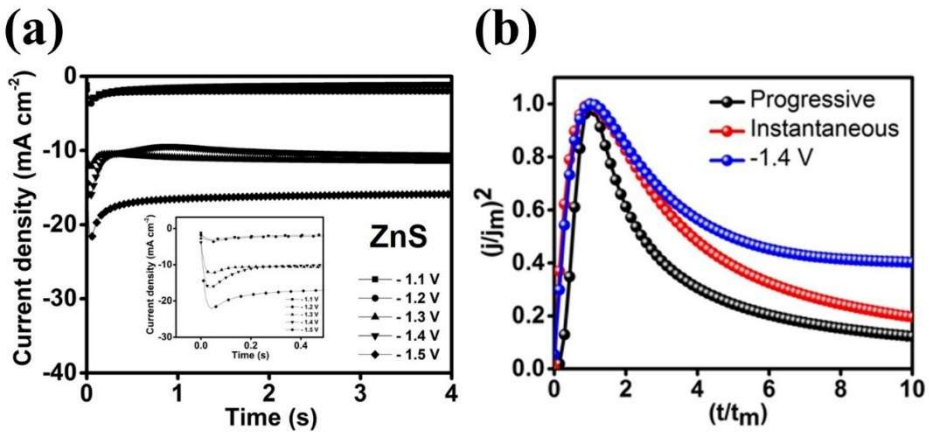

Figure 5.23: Chronoamperometric curves of (a) ZnS at – 1.4 V and dimensionless curves of $(j/j_{max})^2$ vs (t/t_{max}) of (b) ZnS at – 1.4 V along with the theoretical plots corresponding to the progressive (black curve) and instantaneous nucleation (red curve)

The increment in the currents is observed from -1.3 V to -1.5 V as seen in the magnified plot of Figure 5.23a. This is due to initial of deposition of ZnS at -1.3 V which is still non-stoichiometry as presented in **Table 5.6**. However, at the optimized deposition potential -1.4 V, it is observed that there is a raise in the current due to nucleation and reached a peak current and then, a drop in the current indicating the growth process. The electrocrystallization of the films is studied from the dimensionless plots of $(j/j_m)^2$ vs (t/t_m) obtained for ZnS at the optimized potential of -1.4 V. Further when the potential is more negative at -1.5 V, there is steady increase in current due to adsorption of excess sulfur in the films. The experimental curve obtained is compared with that of theoretical curves calculated from the section 5.2.3 for both the progressive and instantaneous nucleation where it is in good correlation with the instantaneous one. This indicates that the ZnS deposition growth occurs via rapid nuclei generation and growth simultaneously. From equation 5.6 the number density of active sites (N_0) for the ZnS is calculated and is observed to be 1.4×10^5 $cm^{-2}s^{-1}$.

5.3.1.5 Surface Morphology and Elemental Mapping of ZnS Films

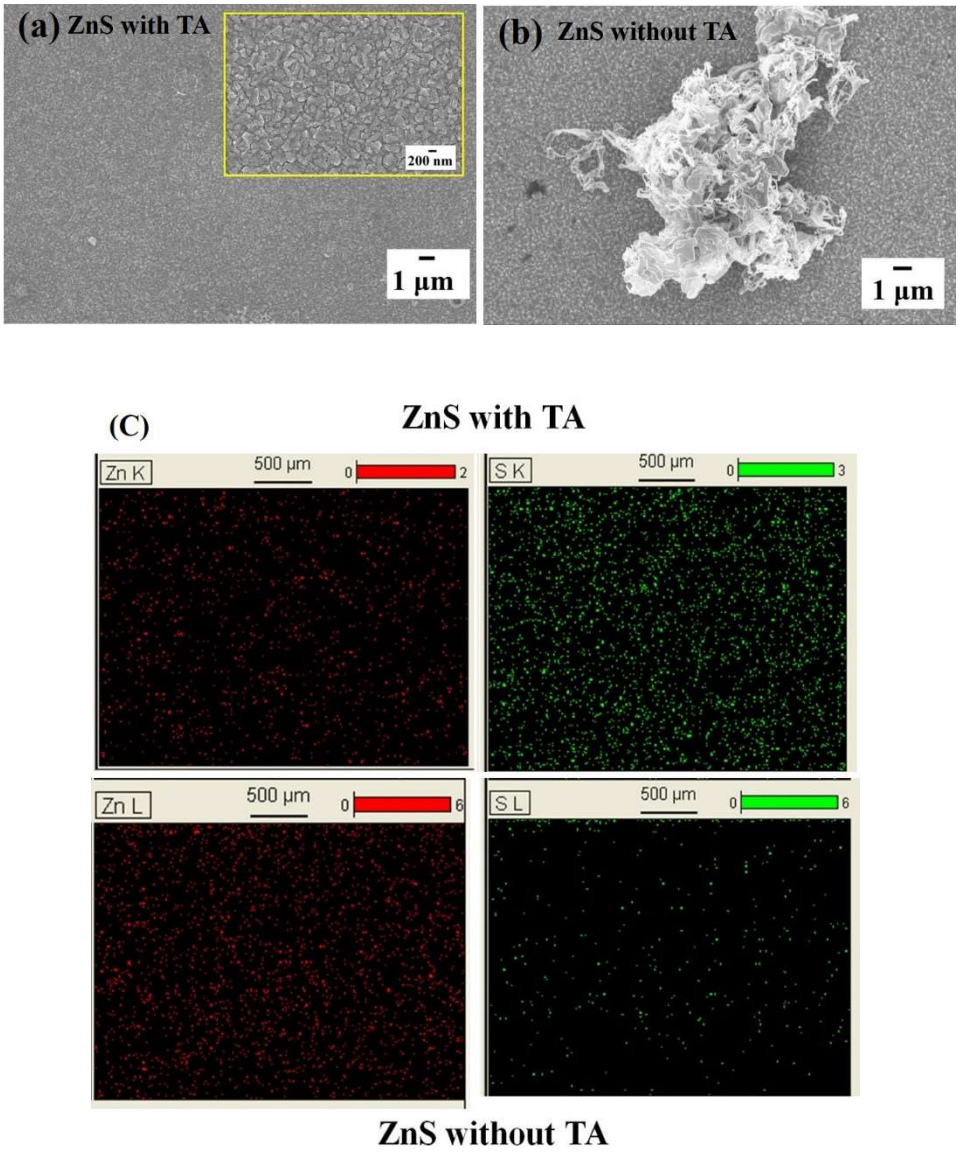

Figure 5.24: surface morphology of ZnS films deposited (a) with tartaric acid (b) without tartaric acid (c) elemental mapping of ZnS films with and without tartaric acid

The FESEM analysis is used to explore the morphological aspects of ZnS films in the presence and absence of tartaric acid. Figure 5.24a depicts the grain distribution of ZnS films deposited at -1.4 V with tartaric acid and glycerol. Figure 5.24a, this film with more uniform grain distribution and greater surface coverage than the film deposited without tartaric acid, where the substrate FTO grains are exposed due to scattered ZnS grains with incomplete growth, as illustrated in Figure 5.24b. The composition of the elemental mapping is investigated, and it is

observed that the film formed in the presence of tartaric acid has a better Zn and S ratio than the film deposited without tartaric acid, which has only zinc deposits, as shown in Figure 5.24c. Based on the facts above, it is possible to deposit better stoichiometry films with homogeneous nanostructured grains, where tartaric acid plays a significant role in the deposition mechanism of ZnS thin films. Therefore, the structural, optical, and photoelectrochemical properties of tartaric acid-based films are being studied further.

5.3.1.6 Impedance Measurements

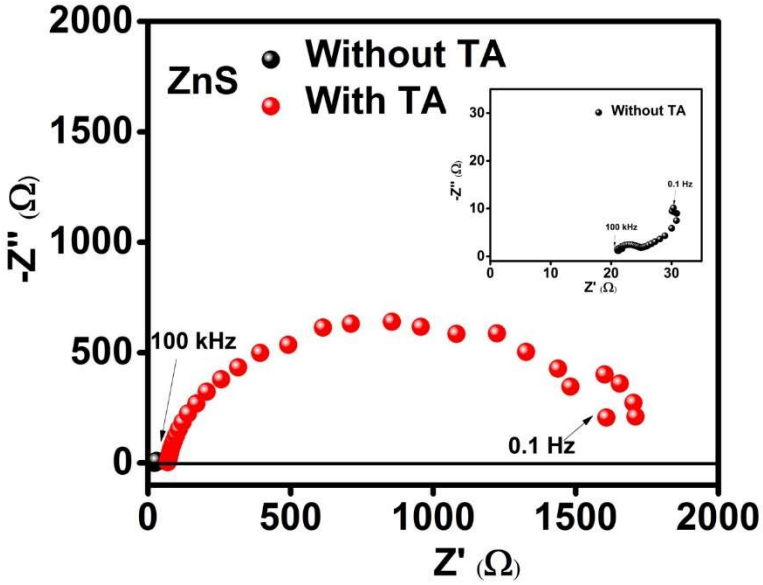

Figure 5.25: Impedance plots of ZnS with and without tartaric acid

Figure 5.25 shows the corresponding EIS data of ZnS with and without tartaric acid at pH 2.5 and pH 6.2, respectively. In the absence of tartaric acid, the development of ZnS is weak, resulting in a capacitance curve showing porosity and non-uniformity in the deposition. The semicircle can be visible for the deposition in the presence of tartaric acid. This shows the production of the Zn-tartrate combination, as previously found (62, 68, 69). Therefore, as a result, the development of complexes aided in the production of higher-quality films at room temperature.

5.3.1.7 Structural Analysis

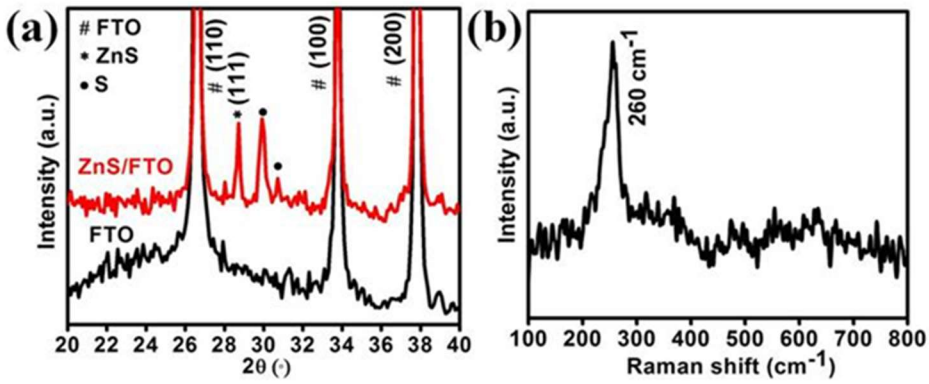

Figure 5.26: (a) XRD analysis (b) Raman Spectrum of electrodeposited ZnS on FTO

The crystal structure of thin films can be studied using XRD. The XRD peaks provide useful information about the crystallinity, structure type, crystallite size, and other properties of the material. The current work for the optimised ZnS thin film with a thickness of 30 nm shows no recognizable peaks. To investigate phase formation, a longer deposition time (two hours) is employed to develop a thicker ZnS coating of ~ 200 nm, which is then subjected to XRD analysis, as other researchers have done (70). Figure 5.26a depicts the diffraction peaks of as-deposited ZnS films, indicating the formation of cubic ZnS with dominant (111) orientation at a 2θ of 28.7°. (JCPDS 04-072-4841). In addition, there are peaks for FTO coated glass substrate (JCPDS 00-77-0452) and sulfur. These data show that long-term deposition resulted in additional sulphur as well as the desirable ZnS phase. Furthermore, the presence of glycerol in the electrolyte inhibits the competing phases ZnO or $Zn(OH)_2$, which plays an essential role in absorbing excess hydroxyl ions by producing glycerolate and boosting the concentration of Zn^{2+} ions in the electrode's diffusion layer. According to LSV study, this mechanism accelerates the reaction rate for ZnS formation. Furthermore, the cubic phase with (200) orientation has previously only been observed when deposited at elevated temperatures of about 70-80 °C (67, 71, 72). In the current study, however, the combination of glycerol and tartaric acid is important for the formation of the necessary cubic phase with (111) orientation. As previously observed, this might be due to tartaric acid carboxyl groups intercalated between the electrolyte and the deposited metal ions, which function as growth regulators leading to grain refining and the development of crystalline grains (19, 73). Tartaric acid has been extensively studied as a complexing agent during pure zinc

deposition, and it has been demonstrated to improve crystallinity while modifying structural characteristics (73). Using Debye Scherrer's equation 3.10, the crystallite size of electrodeposited ZnS films is determined to be 16 nm for the ZnS/FTO coated glass.

$$D = \frac{K\lambda}{\beta cos\theta} \quad (3.19)$$

where D is the crystallite size, K is the constant, λ is the wavelength of X-rays used for the analysis, β is the full width half maximum value of the intense peak, and θ is Bragg's angle.

In addition, a 514 nm Ar ion laser is used as an excitation source for a micro-Raman study of the electrodeposited ZnS thin films to detect different possible phases. Raman spectroscopy outperforms XRD for evaluating extremely thin films in order to obtain structural information by investigating the vibration modes of Zn and S atoms in the ZnS lattice. T_d^2 is the cubic ZnS space group, and Zn and S atoms occupy coordination number 4 sites in the face-centered cubic lattice (FCC). The Raman and infrared modes of ZnS transverse optical (TO) and longitudinal optical (LO) are both active. Figure 5.26b depicts the Raman spectra of a pulse electrodeposited ZnS thin film (thickness 30 nm), which includes a large peak at 260 cm^{-1} associated with the TO phonon. The TO phonon occurs around 275 cm^{-1} in general, but a redshift is noticed, which could be due to nanosized grains generating phonon confinement, which is consistent with previous results (74). The absence of secondary phases in the Raman spectrum is promising, indicating that a phase-pure ZnS film has been formed.

5.3.1.8 *Optical properties*

The transmittance and bandgap are well-known characteristics for the buffer layer in solar applications. In this context, the bandgap of the electrodeposited ZnS/FTO is computed using Tauc's plot using UV-VIS-NIR spectrophotometer transmittance data. Figure 5.27a depicts the average transmittance of ~ 71 % recorded in the wavelength range of 300-900 nm for the ZnS film deposited at -1.4 V at a duty cycle of 75 % for 10 minutes.

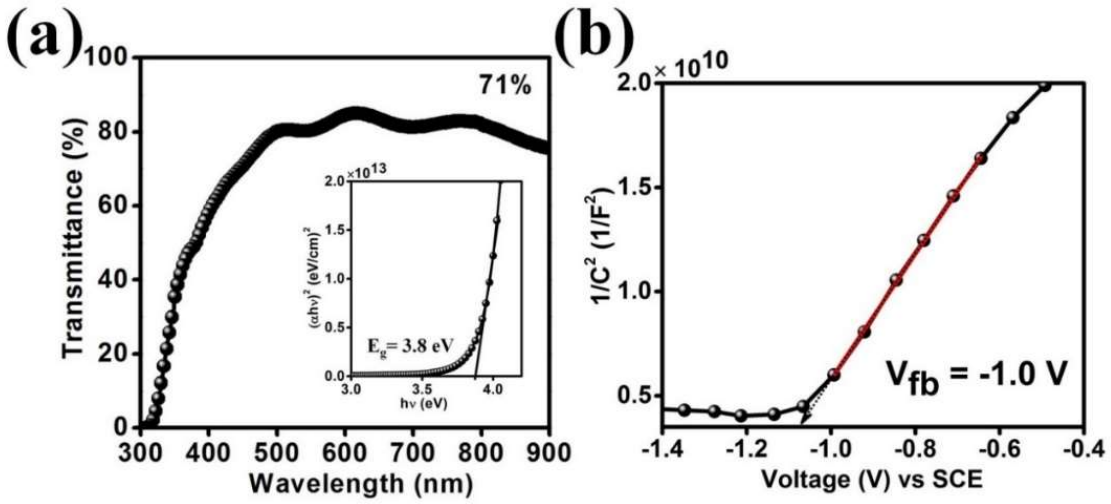

Figure 5.27: (a) Transmittance with an inset of Tauc's plot (b) Mott – Schottky plot of the ZnS film deposited at -1.4 V for 10 minutes

The lack of fringes in the transmittance curves suggests that the films are exceedingly thin over the substrate, as measured by stylus profilometry to be ~ 30 nm. According to Yu Cheng et al., the transmittance values of the ZnS buffer layer can vary between 75 and 85 % for solar applications (64, 75). The bandgap of ZnS is calculated using Tauc's plot, as shown in Equation 3.11.

$$E_g = 3.977 - 0.987\, E_u \tag{5.16}$$

where α is the absorption coefficient, $h\upsilon$ is the incident photon energy, A is a constant, E_g is the bandgap energy of the film, m is equal to ½ for the direct allowed transition, E_u is the Urbach energy.

The inset of Figure 5.27a depicts the Tauc's plot and the bandgap is determined to be 3.8 eV for the electrodeposited ZnS without any post heat-treatment, which agrees well with the reported value for annealed ZnS film (47). Glycerol plays a predominant role in regulating the phase formation and evades oxygen incorporation which is also confirmed from Urbach energy calculations for the films deposited with and without glycerol using equation 5.15 for ZnS semiconductor as reported previously (76). It is noticed that Urbach energy for the film deposited without glycerol is 0.8 eV (bandgap of 3.2 eV) while it is 0.2 eV (bandgap of 3.8 eV) for the films with glycerol. This reduction in the Urbach energy is obvious due to minimal defect states as

glycerol involves the consumption of excess hydroxyl ions and avoids oxygen incorporation into the films. Thus, the films produced in the present work with a wide bandgap tends to favor the transmission of photons from wavelengths of the most solar spectrum to the absorber layer of the device (42).

5.3.1.9 Mott Schottky Analysis

Mott – Schottky analysis is utilized to study the charge transfer reactions at the semiconductor electrode-electrolyte interface. The capacitance of this interface is comparable to that of the space charge region of the *pn* junction. Therefore, the $1/C^2$ vs voltage (V) follows Mott – Schottky relationship as given in 3.5.

Figure 5.27b depicts $1/C^2$ vs V obtained for ZnS films on FTO at 10 kHz with a scan rate of 10 mV s^{-1} using 0.5 M Na_2SO_4 electrolyte. The positive slope of the curve verifies the n-type semiconductor nature of the films. The intercept of the linear part of the curve to the x-axis gives the flat – band potential (V_{fb}) which is about -1.0 V vs SCE, following the reported values for ZnS films (77). The slope values are used to calculate the carrier density concentration using the following expression in 5.16

$$N_D = \frac{2}{\varepsilon\varepsilon_0 e \text{ slope}} \tag{5.17}$$

The donor concentration (N_D) is found to be 9.3×10^{19} cm^{-3} for ZnS/FTO which is similar to the previously reported values (56). The donor density of states (DOS) is calculated from the capacitance value which is about, 8.5×10^{18} $eV^{-1}cm^{-3}$ for ZnS as per 5.17.

$$N_c = \frac{C_{sc}^2}{\varepsilon\varepsilon_o e_0^2} \tag{5.18}$$

5.3.1.10 Photoelectrochemical Studies (PEC)

Prior to its implementation in solar cell, it is imperative to understand the response of ZnS under the light. For this, a preliminary photocurrent analysis is performed to interpret the photoactivity of the ZnS film from the charge transfer reactions between the electrode and electrolyte interface in the dark and illuminated conditions. The most important requirements for a semiconductor to use in the PEC applications, is to have a band gap > 1.2 eV and absorb effective photons in the UV-visible region of the solar spectrum. For a material to be used for both PEC and

photovoltaic applications, having greater insight on the absorption and transmission properties is required. The most efficiently used CdS as photoanode absorbs visible light (< 550 nm) due to its narrow band gap 2.4 eV and therefore is the candidate of interest. However, ZnS is the one material that is explored and is the best alternative to its counterpart CdS due to non-toxicity of the elements.

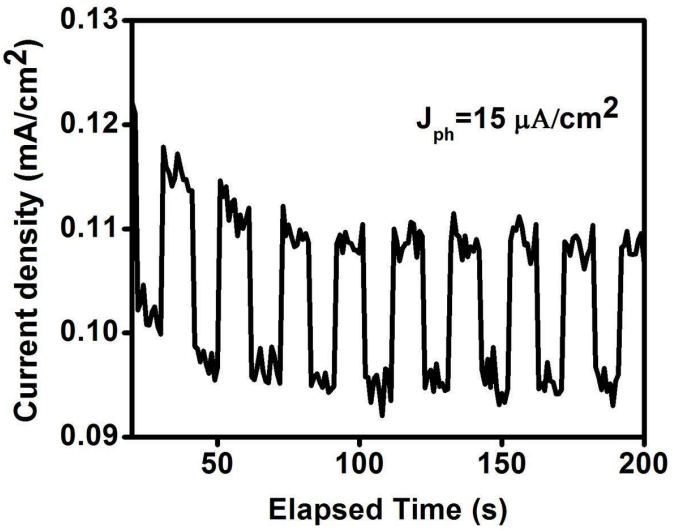

Figure 5.28: Chronoamperometric (J-t) curve of ZnS on FTO

In the present work, electrodeposited ZnS having a band gap of 3.8 eV allows the absorption of photons only in the UV region due to its extended transmission of photons in all the visible light wavelengths. The phenomenon of photoelectric property includes the diffusion of photogenerated minority charge carriers (holes) from the space charge region to the surface of the electrode and undergo an electrochemical reaction. While, the photogenerated electrons in the conduction band of the ZnS induce the reduction of water molecules to hydrogen under light conditions. This reaction accounts for the photocurrents obtained under chopped light and thereby correlates to the photo response of the deposited film under illumination.

The analysis is performed using a conventional three-electrode system with an electrolyte containing Na_2SO_3 + Na_2S. This electrolyte plays a supportive role that scavenges the photogenerated holes thereby reduces their recombination with the sulfide ions of photoanode and restricts the photo corrosion of the film (78). Figure 5.28 shows the amperometric current density-time (J-t) curve obtained at a fixed potential of +0.8 V vs SCE under chopped light where one can

observe the increment in current under the light due to photogenerated carriers. In the present work, ZnS films are found to be reasonable for the photovoltaic application with demonstrated photoactivity, and the obtained photocurrent is higher compared to the previously reported value (79). Moreover, it is also vital to note that ZnS as a wide bandgap semiconductor is transparent to all the visible wavelengths and absorbs only the UV spectrum. This is, in fact, beneficial for the buffer layer application which enhances the efficiency as it transmits all the visible light to the absorber layer.

5.3.2 Fabrication of Cd-free CIGS Solar Cell

The typical construction of Cd-free CIGS device includes electrodeposited CIGS and ZnS layers then, are the ZnO/AZO layers using DC sputtering without any metal grid. The electrodeposited CIGS absorber layer is prepared where (CuGa/In) stack is annealed with the elemental selenium vapor at 550 °C with Ar as the carrier gas. Then, the buffer layer ZnS is deposited at room temperature without a post heat treatment and finally, the ZnO/AZO layers are deposited by sputtering. Finally, the power conversion efficiency of the Cd-free CIGS device having ED-ZnS is studied from Oriel Instruments model 94123A solar simulator attached with the Newport AM 1.5 G lens.

5.3.2.1 *Surface Morphology of ZnS over Mo, and CIGS/Mo*

Figure 5.29 reveals the surface morphologies of the electrodeposited ZnS/Mo, CIGS/Mo and the surface of the electrodeposited of ZnS on CIGS and their physical appearance in Figure 5.30. The SEM images in Figure 5.29a exhibits compact ZnS deposited over Mo substrate with even distribution and similar fine ZnS grains on CIGS films as seen in Figure 5.29c which is quite rough compared to the bare CIGS in Figure 5.29b. From the magnified image in Figure 5.29d, it can be observed that the ZnS grains are very small. Interestingly, the present method deposited a 30 nm ZnS layer with the aid of pulse plating, enabling the deposition of thin films even on complex shapes. Hence, this method of depositing ZnS is advantageous for the Cd-free thin-film solar cells with no post-heat-treatment.

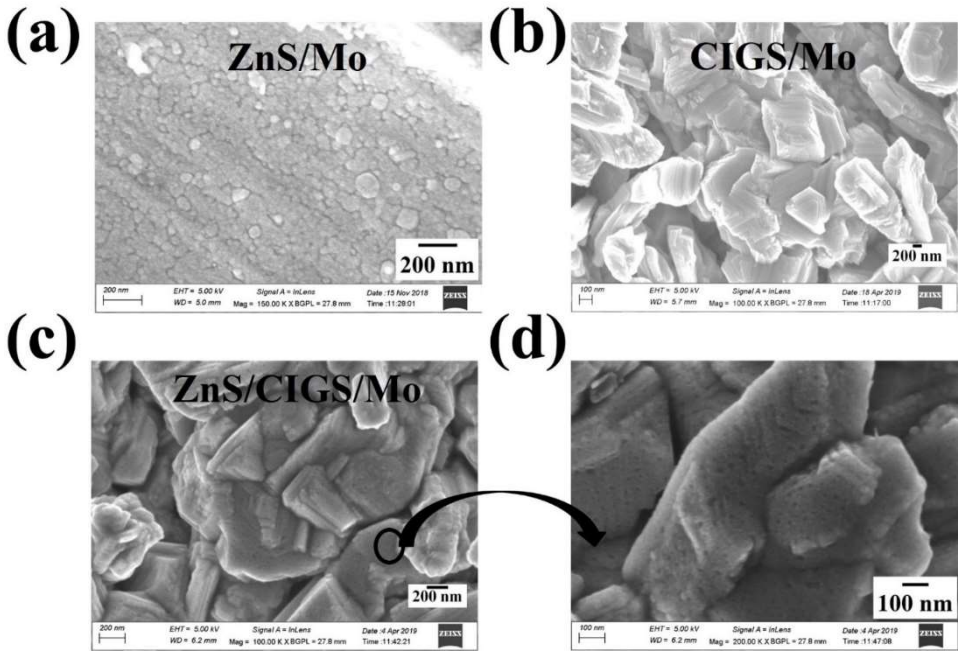

Figure 5.29: Surface morphology of (a) ZnS/Mo (b) CIGS/Mo (c) (d) ZnS/CIGS/Mo

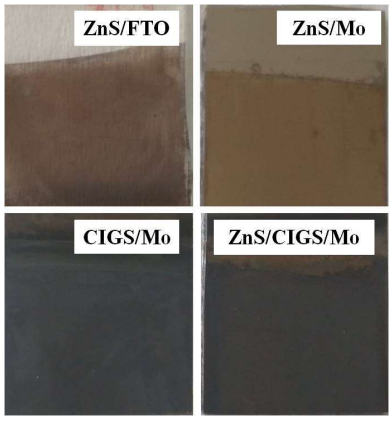

Figure 5.30: Visual appearance of ZnS on different substrates

5.3.2.2 Structural Analysis of ZnS over Mo, and CIGS/Mo

As the films deposited with optimized conditions are extremely thin in few nanometers the ZnS peaks in the XRD patterns retained within the background noise of the peaks. Hence, for the structural analysis thicker films are deposited of about 200 nm on Mo, FTO and CIGS substrates. The XRD analysis of as-deposited ZnS/Mo films as depicted in Figure 5.31 reveals cubic phase with (111) orientation at 28.7° at 2θ angle (JCPDS 04-072-4841). Further similar orientations of ZnS are observed on ZnS/CIGS/Mo along with tetragonal CIGS peaks with preferred orientation

(112) at a 2θ value 26.8° (JCPDS 01-079-7081). This indicates that the films with non – stoichiometry still forms the favorable phase which also agrees with the previous reports[26].

3.5

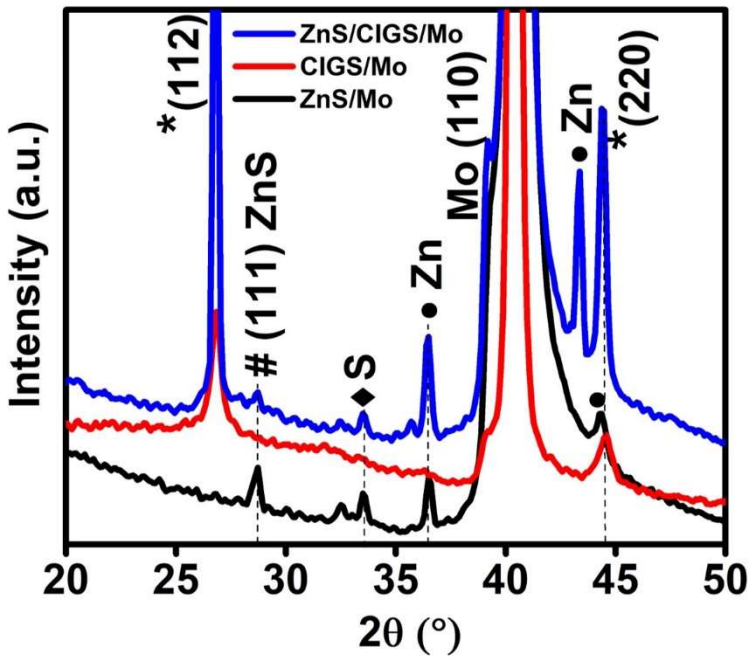

Figure 5.31: X-ray diffraction patterns of ZnS on Mo and CIGS/Mo

Apparently, there are no oxides formed such as ZnO or $Zn(OH)_2$ as glycerol plays an important role and interferes with the equilibrium of complex ion $Zn(OH)_2$ and increases the concentration of Zn^{+2} ions in the diffusion layer. As the deposition time is increased to obtain thicker films the impurity of Zn and S peaks are also observed from the XRD data. The available literature reported on electrodeposition of ZnS with cubic phase (200) preferred orientation[10], [21], [31]. However, it is for the first time to deposit cubic (111) ZnS on Mo and CIGS. The reason could be attributed to the role of tartaric acid in the phase transformation during deposition. This additive is widely studied in the deposition of pure zinc and reported the improvement in the crystallinity and thereby influencing the structural aspects (80). The crystallite size is calculated from the Debye Scherrer's equation $D = \frac{K\lambda}{\beta cos\theta}$ (3.19)

and is found to be 30 nm for the ZnS/FTO, 25 nm on ZnS/Mo and 23 nm for ZnS/CIGS/Mo. This indicates that the crystallite size decreases along with the thickness of the film as reported

previously (81) which is also correlating with the thickness measurement data where ZnS on FTO is 37 nm and on Mo it is 29 nm. The variation in the peak intensity also attributes to the crystallite size due to quantum confinement hence the ZnS over CIGS has the least intense broad peak as reported earlier (82). These results revealed that the ZnS layer deposited for 10min at room temperature possess crystalline quality. When compared to the conventional CBD method that requires 1-2 hr deposition at 80-90 °C to obtain good quality grains (74) the present method of ZnS electrodeposition forms device quality films within 10 minutes with the aid of pulse plating.

5.3.2.3 Optical properties of ZnS/CIGS/Mo

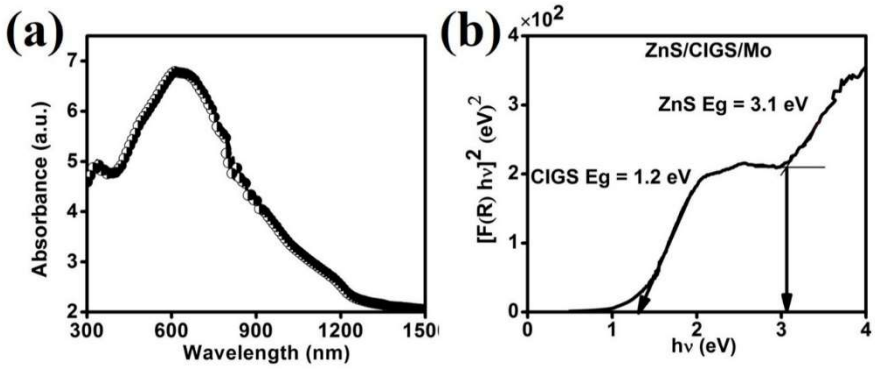

Figure 5.32: (a) absorption spectrum of ZnS/CIGS/Mo (d) Tauc's plot of ZnS/CIGS/Mo deposited at -1.4V for 10 minutes at 75% duty cycle

UV-VIS-NIR spectrophotometer is used to study the optical properties. The diffuse reflectance mode is utilized to calculate the bandgap of the ZnS thin film on the electrodeposited CIGS absorber layer. Figure 5.32a depicts the absorbance spectrum of ZnS deposited over electrodeposited CIGS absorber layer and Figure 5.32b shows the bandgap of the optimized ZnS films over CIGS/Mo calculated using the Tauc's plot of the equation

$$\alpha h\upsilon = A(h\upsilon - E_g)^m \qquad (3.20).$$

The absorbance spectrum clearly shows two different absorption edges at 400 nm and 1000 nm indicating the presence of ZnS and CIGS respectively. It is also observed that there is a decrease in the bandgap of ZnS over CIGS when compared to the ZnS deposited on FTO. The bandgap of the ZnS and CIGS using Tauc's plot. The ZnS film deposited over CIGS the bandgap

is found to be 3.1 eV and CIGS with 1.2 eV. The details of device performance and IV characteristics are discussed in chapter 7.

5.4 Summary

Phase-pure CdS and ZnS thin films are deposited at room temperature using pulse electrodeposition. The presence of tartaric acid and its role in promoting the formation of crystalline CdS and ZnS films at room temperature electrodeposition is discussed with no further heat treatment. CdS thin films showed polycrystalline hexagonal phase and ZnS revealed cubic phase. This higlights the potential usefulness of organic reagents in the thin film deposition. The nucleation and growth mechanism are validated at their respective deposition potentials using chronoamperometry. The experimental data obtained in the present study for CdS and ZnS are compared with the theoretical curves of nucleation extracted from the Scharifker-Hills model and realized that the CdS follow progressive and that of ZnS follow instantaneous nucleation. Further, the elemental mapping of the films has supported the findings demonstrating the role of tartaric acid in both the composition and morphology. From the EIS data, it is concluded that the formation of CdS and ZnS occurs via the formation of intermediate metal tartrate complex. The results provide a new perspective on the formation of these binary sulfides with better composition and grain distribution. CdS films are stoichiometric containing conformal flower-like particle and ZnS having spherical grains as affirmed from SEM-EDS. Optical studies indicate transparency of CdS and ZnS films as desired for application in thin films solar cells with a band gap of 2.49 eV and 3.8 eV respectively. These properties obtained without heat treatment is particularly important from the perspective of device fabrication.

References

1. J. Gawroński and K. Gawrońska, *Tartaric and malic acids in synthesis : a source book of building blocks, ligands, auxiliaries, and resolving agents*, p. 17, Wiley (1999).
2. Y. Chung and C.-W. Lee, *Journal of Electrochemical Science and Technology*, **3**, 95 (2012).
3. A. A. Ojo and I. M. Dharmadasa, *Materials Chemistry and Physics*, **180**, 14 (2016).
4. D. M. Figen KADIRGAN, Wenjie SONG, Tim OHNO,Brian McCANDLESS, *Turk J Chem*, **24** 21 (2000).
5. N. A. Abdul-Manaf, A. R. Weerasinghe, O. K. Echendu and I. M. Dharmadasa, *Journal of Materials Science: Materials in Electronics*, **26**, 2418 (2015).
6. N. Elgrishi, K. J. Rountree, B. D. McCarthy, E. S. Rountree, T. T. Eisenhart and J. L. Dempsey, *Journal of Chemical Education*, **95**, 197 (2017).
7. S. Dennison, *Electrochimica Acta,*, **38**, 2395 (1993).
8. F. Kesri, Affoune, Abed, Djaghout, Ilhem, *Journal of the Serbian Chemical Society*, **84**, 41 (2019).
9. A. Sahari, A. Azizi, G. Schmerber and A. Dinia, *Surface Review and Letters*, **15**, 717 (2008).
10. M. E.-r. Akif Shikhan Aliyev, Z. H. Hasanli, R. H. Huseynova, Y. A. Nuriyev, *International Journal of Nano and Material Sciences*, **2**, 36 (2013).
11. J. J. Yongkuk Kim, Seunghun Kim and Won-Seok Chae, *Materials Transactions,*, **54**, 1467 (2013).
12. F.-H. Li, W. Wang, J.-P. Gao and S.-Y. Wang, *Journal of The Electrochemical Society*, **156**, D84 (2009).
13. Y. Kim, J. Jung, S. Kim and W.-S. Chae, *Materials Transactions*, **54**, 1467 (2013).
14. B. Scharifker and G. Hills, *Electrochimica Acta*, **28**, 879 (1983).
15. K. Raeissi, A. Saatchi and M. A. Golozar, *Journal of Applied Electrochemistry*, **33**, 635 (2003).
16. F. Peng, S.-J. Qin, Y. Zhao and G.-B. Pan, *International Journal of Electrochemistry*, **2016**, 1 (2016).
17. H. Y. R. Atapattu, S. De Silva, K. A. S. Pathiratne, O. Olusola and I. Dharmadasa, *Journal of Materials Science: Materials in Electronics*, **28**, 18592 (2017).
18. O. Aaboubi, J. Douglade, X. Abenaqui, R. Boumedmed and J. VonHoff, *Electrochimica Acta*, **56**, 7885 (2011).
19. D. Boosagulla, S. Mandati, R. Allikayala and B. V. Sarada, *ECS Journal of Solid State Science and Technology*, **7**, P440 (2018).
20. J. S. Patil, S. S. Dhasade, A. R. Babar, S. Patil and V. J. Fulari, *Superlattices and Microstructures*, **83**, 565 (2015).
21. Y.-L. Zhou, W.-H. Zhou, M. Li, Y.-F. Du and S.-X. Wu, *The Journal of Physical Chemistry C*, **115**, 19632 (2011).
22. S. Mandati, B. V. Sarada, S. R. Dey and S. V. Joshi, *Journal of Renewable and Sustainable Energy*, **5**, 031602 (2013).
23. K. R. Murali, S. Kumaresan and J. Joseph Prince, *Materials Science in Semiconductor Processing*, **10**, 56 (2007).
24. A. Majid, R. Ahmad, A. Nabi, A. Shakoor and N. Hassan, *Nanomaterials and Nanotechnology*, **2**, 2 (2012).

25. K. W. Böer, *Energy Conversion and Management*, **52**, 426 (2011).
26. K. Ravichandran and P. Philominathan, *Solar Energy*, **82**, 1062 (2008).
27. V. Hernández-Calderón, O. Vigil-Galán, M. Guc, A. Carrillo-Osuna, S. Ramírez-Velasco, F. J. Sánchez-Rodríguez, P. Vidal-Fuentes, S. Giraldo, E. Saucedo and Y. Sánchez, *ACS Applied Energy Materials*, **3**, 6815 (2020).
28. H. I. Salim, O. I. Olusola, A. A. Ojo, K. A. Urasov, M. B. Dergacheva and I. M. Dharmadasa, *Journal of Materials Science: Materials in Electronics*, **27**, 6786 (2016).
29. S. Xue, X.-F. Jiang, G. Zhang, H. Wang, Z. Li, X. Hu, M. Chen, T. Wang, A. Luo, H.-p. Ho, S. He and X. Xing, *ACS Sensors*, **5**, 1004 (2020).
30. H. Wu, Z. Zheng, Y. Tang, N. M. Huang, R. Amal, H. N. Lim and Y. H. Ng, *Sustainable Materials and Technologies*, **18**, e00075 (2018).
31. S. Mandati, B. V. Sarada, S. R. Dey and S. V. Joshi, *Electronic Materials Letters*, **11**, 618 (2015).
32. A. Pareek, R. Dom and P. H. Borse, *International Journal of Hydrogen Energy*, **38**, 36 (2013).
33. M. Zhang, *Nano-Micro Letters*, **5**, 242 (2013).
34. Q. Wang, J. Lian, J. Li, R. Wang, H. Huang, B. Su and Z. Lei, *Sci Rep*, **5**, 13593 (2015).
35. O. D. Echendu, Imyhamy, *Energies*, **8**, 4416 (2015).
36. X. Fang, T. Zhai, U. K. Gautam, L. Li, L. Wu, Y. Bando and D. Golberg, *Progress in Materials Science*, **56**, 175 (2011).
37. P. H. Borse, W. Vogel and S. K. Kulkarni, *Journal of colloid and interface science*, **293**, 437 (2006).
38. M. A. Shakil, S. Das, M. A. Rahman, U. S. Akther, M. K. Hassan and M. K. Rahman, *Materials Sciences and Applications*, **09**, 751 (2018).
39. A. Zyoud, S. Al-Yamani, H. Bsharat, M. H. Helal, H. Kwon, D. Park and H. S. Hilal, *Materials Science in Semiconductor Processing*, **74**, 277 (2018).
40. B. Divya, S. Harish, K. Ramaswamy, M. Kishorebabu, N. Raju, R. Govindaiah, U. Rambabu and N. R. Munirathnam, *International Journal of Environmental Science and Technology*, **14**, 2603 (2017).
41. S. Siebentritt, *Solar Energy*, **77**, 767 (2004).
42. T. Nakada and M. Mizutani, *Japanese Journal of Applied Physics*, **41**, L165 (2002).
43. B.-R. K. Won Song, Seok Eui Choi, Yong-Taeg Oh, and Dong-Chan Shin, *International Journal of Materials and Metallurgical Engineering*, **6** (2012).
44. M. Izi, G. Heidari, S. M. Mousavi Khoie and J. Najafi, *Surface Engineering and Applied Electrochemistry*, **53**, 245 (2017).
45. H. S. Kim, G. Kim, E. Kim, S. J. Cho, D. J. Lee, S. G. Choi, F. Shan and S. J. Kim, *Journal of nanoscience and nanotechnology*, **19**, 1799 (2019).
46. T. T. Ngoc Van, A. S. Ansari and B. Shong, *Journal of Vacuum Science & Technology A*, **37**, 020909 (2019).
47. M. L. Madugu, O. I.-O. Olusola, O. K. Echendu, B. Kadem and I. M. Dharmadasa, *Journal of Electronic Materials*, **45**, 2710 (2016).
48. S H Mohamed1, MEl-Hagary1,3 andMEmam-Ismail1,4, *JOURNAL OF PHYSICS D: APPLIED PHYSICS*, **43** (2010).
49. T. N. 'M.A. Contreras, 'M. Hongo, 'A.O. Pudov, and 'J.R. Sites, *3rd World Conference on Phorovolraic Energv Conversion* (2003).

50. K. Y. Motoshi Nakamura , Yoshinori Kimoto, Yusuke Yasaki, Takuya Kato , and Hiroki Sugimoto, *IEEE JOURNAL OF PHOTOVOLTAICS*, **9**, 1863 (2019).
51. M. Jafarov, E. Nasirov, S. A. Jahangirova and R. Jafarli, in (2015).
52. S. Mandati, B. V. Sarada, S. R. Dey and S. V. Joshi, in *Semiconductors-growth and characterization*, p. 109, INTECH (2018).
53. M. Bouroushian, *Electrochemistry of Metal Chalcogenides* (2010).
54. B. W. Sanders, *Journal of Crystal Growth*, **100**, 405 (1990).
55. K. R. Murali, *IOSR Journal of Applied Physics*, **6**, 9 (2014).
56. R. Bengas, H. Lahmar, K. M. Redha, L. Mentar, A. Azizi, G. Schmerber and A. Dinia, *RSC Advances*, **9**, 29056 (2019).
57. H. M. M. N. Hennayaka and H. S. Lee, *Thin Solid Films*, **548**, 86 (2013).
58. A. A. Ojo, *Materials Research Express*, **6**, 086465 (2019).
59. N. O. Naohiro Matsuda, and Takeyasu Saito, in *ICEP-IAAC 2018 Proceedings*, Kuwana, Mie, Japan (2018).
60. O. K. Echendu, A. R. Weerasinghe, D. G. Diso, F. Fauzi and I. M. Dharmadasa, *Journal of Electronic Materials*, **42**, 692 (2013).
61. N. Fathy and M. Ichimura, *Solar Energy Materials and Solar Cells*, **87**, 747 (2005).
62. Q. Cheng, D. Wang and H. Zhou, *Journal of Energy Chemistry*, **27**, 913 (2018).
63. Fabio Galvani and Ivani A. Carlos, in *Nickel and Chromium Plating*, M. finishing Editor, p. 70, Elseiver, NY (1997).
64. M. B. Dergacheva, K. A. Urazov, G. M. Khussurova and K. A. Leontyeva, *Coatings*, **6**, 14 (2016).
65. J. Torrent-Burgués and E. Guaus, *Journal of Applied Electrochemistry*, **37**, 643 (2007).
66. A. Dolati, A. Afshar and H. Ghasemi, *Materials Chemistry and Physics*, **94**, 23 (2005).
67. X. Xu, F. Wang, Z. Li, J. Liu, J. Ji and J. Chen, *Electrochimica Acta*, **87**, 511 (2013).
68. C. G. Jeffrey R. S. Brownson, Gerardo Larramona, Alain Jacob, Bruno Delatouche, and Claude Lévy-Clémenta, *Journal of The Electrochemical Society*, **155**, D40 (2008).
69. A. E. N. M. B. Dergacheva, K. A. Urazov, N. N. Gudeleva, V. I. Yaskevich, and V. P. Grigor'eva, *Russian Journal of Applied Chemistry*, **91**, 778 (2018).
70. R. S. G. Nabiyouni, M. Toghiany, M. H. Majles Araand K. Hedayati, *Rev.Adv.Mater.Sci.*, **27**, 52 (2011).
71. K. Ghezali, L. Mentar, B. Boudine and A. Azizi, *Journal of Electroanalytical Chemistry*, **794**, 212 (2017).
72. F. Long, W.-M. Wang, Z.-k. Cui, L.-Z. Fan, Z.-g. Zou and T.-k. Jia, *Chemical Physics Letters*, **462**, 84 (2008).
73. J. T.-B. a. E. Guaus, *Journal of Applied Electrochemistry* (2007).
74. A. Karimi, B. Sohrabi and M. R. Vaezi, *Thin Solid Films*, **651**, 97 (2018).
75. F.-P. Yu, Ou, Sin-Liang,Yao, Pin-Chuan,Wu, Bing-Rui,Wuu, Dong-Sing, *Journal of Nanomaterials*, **2014**, 1 (2014).
76. B. Y. S. Ebrahimi, N. Naderi, *Advanced Ceramics Progress*, **3** (2017).
77. S. Wojtyła and T. Baran, *Materials Chemistry and Physics*, **212**, 103 (2018).
78. S. Mandati, B. V. Sarada, S. R. Dey and S. V. Joshi, *Journal of Power Sources*, **273**, 149 (2015).
79. M. A. Ehsan, T. A. N. Peiris, K. G. U. Wijayantha, H. Khaledi, H. N. Ming, M. Misran, Z. Arifin and M. Mazhar, *Thin Solid Films*, **540**, 1 (2013).
80. J. Torrent-Burgués and E. Guaus, *Journal of Applied Electrochemistry*, **37**, 643 (2007).

81. A. Fairbrother, V. Izquierdo-Roca, X. Fontané, M. Ibáñez, A. Cabot, E. Saucedo and A. Pérez-Rodríguez, *CrystEngComm*, **16**, 4120 (2014).
82. J. H. A. Dong Hyun Hwang, Kwun Nam Hui, Kwan San Hui and Young Guk Son, *Nanoscale Research Letters*, **7** (2012).

CHAPTER 6

PULSE ELECTRODEPOSITION OF ZINC OXIDE (i-ZnO) AND Al DOPED ZnO (Al:ZnO) WINDOW LAYERS

CHAPTER 6
PULSE ELECTRODEPOSITION OF ZINC OXIDE (i-ZnO) AND Al DOPED ZnO (Al:ZnO) WINDOW LAYERS

6.1 Introduction

Aluminum doped zinc oxide (Al: ZnO/AZO) is a multifunctional material and an n-type semiconductor with a bandgap > 3.3 eV. AZO thin-films have exceptional transparency over the whole visible spectrum of the sun (400-800 nm). Because of their electrical and optical qualities, as well as their non-toxicity, they have attracted interest for a variety of applications that need low resistive materials, such as flat panel displays, light-emitting diodes (LEDs), gas sensors, transistors, and solar cells (1-5). The material's low cost and thermal stability make it an appealing alternative for flexible electronics (6). It is a possible contender for window applications due to its significant absorption in the UV portion of the solar spectrum (7). AZO is widely used as a transparent conducting oxide (TCO) in thin-film solar cells such as CIGS, CZTS, and CdTe. Although some research has suggested other group III metals as dopants, such as Ga and In (5, 8), Al has been the most commonly used dopant since it is abundant on Earth and cost-effective, competing with ITO films for transparent electrodes (**Figure 6.1**). In addition, Al as a dopant improves various aspects of ZnO, including transparency, band-gap, and electrical conductivity. AZO has a hexagonal wurtzite crystal structure under standard conditions, with lattice constants a = 3.24 and c = 5.2 (c/a = 1.6) (9). Chemical bath deposition (CBD), chemical vapor deposition (CVD), sputtering, successive ionic layer adsorption reaction (SILAR), spray pyrolysis, sol-gel, dip coating, and electrodeposition are the most successful ways for creating Al: ZnO thin films (3, 5, 10, 11).

Most research groups focused on lowering costs through the use of non-vacuum solution processing. Among the methods listed above, electrodeposition has the potential to create higher quality ZnO thin films with a variety of nanostructures and is being intensively researched. The electrodeposition approach is simply appealing because of its ability to control several variables such as pulse parameters, deposition potential, time, current, pH, and temperature. The most

intriguing aspect is the use of pulse electrodeposition, in which the pulse parameters such as duty cycle, frequency, and pulse current/potential may be adjusted independently, affecting the characteristics of the deposits and producing smooth and homogeneous thin films (12).

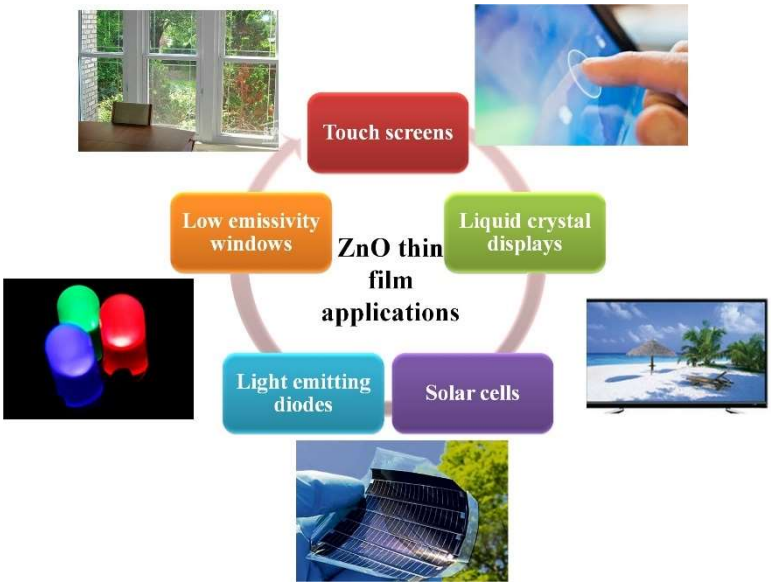

Figure 6.1: Applications area of ZnO materials

Several research groups have developed electrodeposited Al-doped ZnO films using aluminum salt precursors such as aluminum chloride (13) and aluminum nitrate (14). Similarly, zinc nitrates or zinc chlorides have been used as zinc precursors in the majority of the published literature. ZnO deposition is frequently performed in aqueous solutions at elevated temperatures (60-80 °C) (13). The use of oxygen-containing salts such as $Zn(NO_3)_2$ and $Al(NO_3)_2$ as precursors for both cationic and anionic species is beneficial (14). When compared to undoped ZnO thin films, Al doping changes both the structural and optical properties. Several groups devised various ways for accurately controlling the composition and doping of Al, and have observed a modest upshift in the X-ray diffraction angle and an increase in the bandgap due to moderate Al doping into the ZnO lattice (15). Some investigations reported utilizing Al foil from aqueous solutions to produce AZO via a chemical bath approach to dope Al (16). It is also critical to generate crystalline quality thin films; thus, deposition is frequently performed at high temperatures to accelerate the rate of reaction. Hodes et al(17) were the first to publish the use of DMSO as a solvent for the production of ZnO, whereas Choi et al (18) reported Al doping using $Al(NO_3)_2$ in DMSO. The Al metal foil is used as a source of Al to serve as a precursor in this work, and the metal dopant

concentration is properly tuned. It is widely known that in aqueous solutions, Al tends to form the dominant and stable Al_2O_3 phase, which inhibits its dissociation into metal ions and results in subsequent phases with low doping concentration. In many cases, electrochemical deposition of Al: ZnO is carried out at temperatures ranging from 90 to 140 °C in order to favor Al deposition and get the hexagonal phase with a larger crystal size (10). In this context, the usage of metal foils/sheets, as well as their dissolution process in various electrolytes, needs to be investigated further in order to extend deposition temperatures and electrochemical potential windows depending on the solvent utilized.

As a consequence, the current study investigated the use of aluminum foil as an Al source for doping into ZnO, which is deposited using DMSO electrolyte. It is studied and understood that Al from its metal foil complexes with DMSO and enhances the doping of Al to produce AZO thin films that mimic the quality of films formed from the metal salt precursor. To the best of our knowledge, no papers have been published on the impregnation of Al metal foil as a source of Al doping during ZnO electrodeposition. Therefore, this is the first study to include Al doping from an aluminum metal foil into the ZnO lattice. The doping is confirmed by interpreting the structural and optical properties of the films before and after the annealing treatment.

6.2 Experimental

6.2.1 Optimization of Al:ZnO Thin Films using Novel Doping Approach

In the present work, the growth of Al-doped ZnO thin films takes place with the dissociation of $ZnCl_2$ to Zn^{+2} ions in the presence of LiCl as a supporting electrolyte. These metal ions combine with the readily available oxide ions from the molecular oxygen and Al^{3+} ions released from the aluminum metal foil at the working electrode and form Al-doped ZnO thin films. The doping of Al atoms is optimized with the insertion of metal foil at various temperatures during heating of the electrolyte. Under applied constant potential -3.0 V, the Zn^{2+} ions are produced from the metal precursor as shown in reaction 6.1. The pH of electrolyte strongly influences the growth and orientation of the films and hence the most widely used value lies within range 7-10 as studied by Jianping et al (19). Therefore, the work presented here, involves the deposition in an electrolyte having pH 7.0 at temperature 90 °C. The formation of Al^{3+} ions via the metal complex with DMSO as given in reaction 6.2 is dominated due to the dissolution of metal foil compared to the formation of Al_2O_3 at elevated temperature of the bath as reported previously (20). The release of Al atoms

from the metal foil mainly involves the mechanism of forming the metal (Al) complex as an unstable intermediate due to the available unshared electrons of sulfoxide, that bonds with the Al having unfilled *p*-orbital where DMSO plays a vital role and is the most suitable solvent (21). Finally, the dissolved oxygen species from the bubbled oxygen combines with the readily available Zn^{2+} and forms ZnO as shown in reactions 6.3 at the cathode.

$$ZnCl_2 \rightarrow Zn^{2+} + 2Cl^- + 2e^- \quad (6.1)$$

$$Al + ((CH_3)_2SO) \leftrightarrow [Al\,((CH_3)_2SO)]^{3+} \quad (6.2)$$

$$Zn^{2+} + \tfrac{1}{2}O_2 + 2e^- \rightarrow ZnO \quad (6.3)$$

6.2.2 Optimization of Al Doping with Aluminum Foil

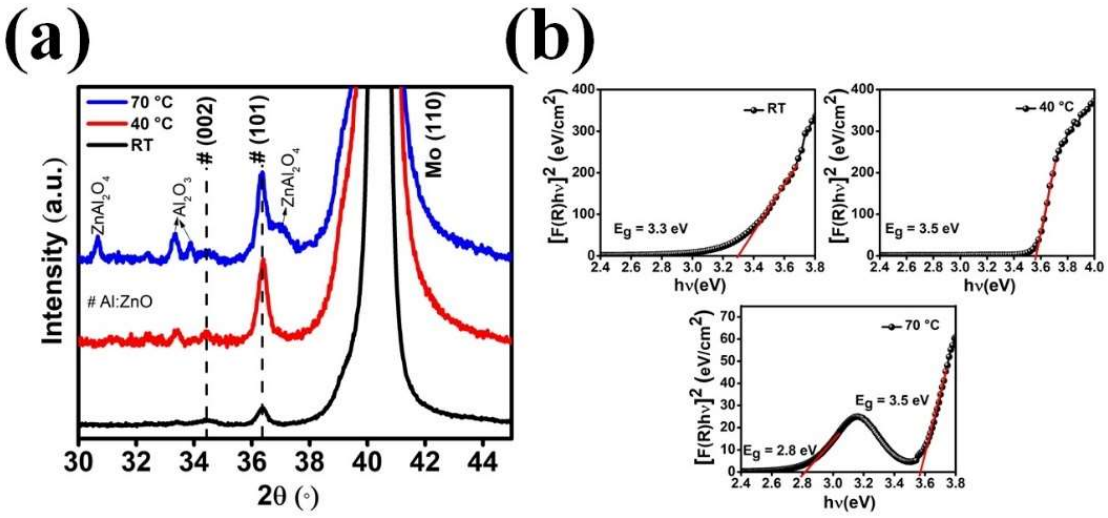

Figure 6.2: (a) XRD patterns (b) Bandgap of AZO thin films at different concentrations of Al deposited at -3.0 V at 25 % duty cycle for 10 minutes

During the preliminary experiments, molybdenum (Mo) coated soda lime glass is utilized for characterization of films at varied conditions. It is observed that the 2θ values of impurity phases emerging during the deposition has nearly similar 2θ values corresponding to FTO peaks. Thus, our choice of Mo substrate appears to be reasonable for investigating structural aspects of secondary phases. Therefore, Al doping is optimized by varying the insertion of aluminum foil at different temperatures while elevating bath temperature to 90 °C. This variation led to an interesting result as depicted in Figure 6.2a that when the foil is dipped into the electrolyte at room

temperature while ramping to the desired deposition temperature 90 °C negligible dissociation of Al^{3+} ions from the foil is observed resulting in the formation of ZnO alone. While at 40 °C, the films have shown an Al content of about 2 atomic % with a significant shift in the XRD peak of (101) orientation (JCPDS 04-019-3163) towards higher 2θ indicating the formation of Al: ZnO films. The shift is because of the smaller ionic size of Al^{3+}, which substitutes the Zn atoms in the ZnO lattice and results in the reduction of lattice parameters. This is evident in the present case where the lattice constants a and c are reduced when the deposition is carried out with the insertion of Al foil at 40 °C compared to the films deposited with insertion at RT and 70 °C indicating the formation of Al:ZnO film as presented in Table 6.1.

From Figure 6.2a, it is also verified that XRD patterns of the film deposited at 70 °C showed the formation of secondary phases such as alumina (Al_2O_3) (JCPDS no. 10-0414) and zinc gahnite phase $ZnAl_2O_4$ (JCPDS no. 05-0669) due to excess Al content of ~ 37 atomic % in support with the previous observations (22, 23). This is indicative that aluminum dissolution from the metal foil is higher at 70 °C thereby leading to impure phases. It is also observed that the Al doping at various temperatures affected the bandgap of the films as shown in Figure 6.2b. At room temperature, where the Al content is negligible, the Tauc's plot revealed the formation of the ZnO phase with a 3.3 eV bandgap as indicated in Table 6.1. Further, when the films are deposited at elevated temperatures as expected, there is a considerable blue shift in the bandgap towards higher photon energy. This is due to the substitution of Zn atoms with Al atoms in the ZnO lattice that inserts the band energy levels and therefore enlarges the bandgap values. However, the film deposited from the electrolyte with Al foil inserted at 70 °C, revealed two different absorption edges that can lead to the presence of defect states.

As inferred from the XRD results, the film contains a higher concentration of unreacted Al and thereby gives rise to poor-quality films. The first linear segment corresponds to the Al: ZnO with a bandgap of 2.9 eV and the next linear segment showing 3.5 eV bandgap is due to the impure phase formed with the excess Al content as identified by other works (24, 25). Therefore, it is important to note that the gradual dissolution of Al^{3+} ions at lower temperatures from the metal foil favors better growth than the vigorous release of Al^{3+} ions due to increased corrosion at a higher temperature. This is the core aspect that greatly signifies the quality of deposit as evident from the XRD results. To understand the electrical properties of the as-deposited and annealed

films, further depositions are performed under this controlled condition where Al foil is impregnated at 40 °C while ramping to 90 °C for the deposition.

Table 6.1:Elemental composition and lattice parameters of the deposited AZO thin films at -3.0 V, 90 °C with varied Al foil impregnation

Al foil insertion temperature	(hkl)	2θ (°)	Lattice parameters		Composition at %		
			a (A°)	c (A°)	Zn	Al	O
RT	(101)	36.3	5.8	9.5	52.2	0.5	47.3
40 °C	(101)	36.4	5.7	9.5	46.4	2.3	51.3
70 °C	(101)	36.3	5.8	9.5	17.3	37.5	45.2

During the preliminary experiments, Al doping is optimized by varying the insertion of aluminum foil at different temperatures while elevating bath temperature to 90 °C. This variation led to interesting results when the foil is dipped into the electrolyte at room temperature while ramping to the desired 90 °C. In this condition, there appears negligible dissociation of Al^{3+} ions from the foil resulting in the formation of ZnO alone with 0.5 atomic % of Al. While at 40 °C, the films have shown an Al content of about 2 atomic % indicating the formation of moderately doped Al: ZnO films. When the deposition is carried out with the Al foil at 70 °C there is excess Al deposition with ~ 37 % as detailed in Table 6.1. Therefore, it is important to note that the gradual dissolution of Al^{3+} ions at optimal temperatures from the metal foil favors better growth than the vigorous release of Al^{3+} ions due to increased corrosion at higher temperature. This is the core aspect that greatly signifies the quality of deposit. To further, understand the electrical and optical properties, the films are deposited under the controlled condition where Al foil is inserted into electrolyte at 40 °C, while ramping the electrolyte to 90 °C prior to the deposition.

6.2.3 Surface Morphology and Elemental Mapping of AZO Thin Films

Based on the EDAX measurements, the atomic chemical composition of the AZO films is determined which showed 46.4 % zinc and 51.3 % oxygen with ~ 2.3 % aluminum incorporation and identical films are utilized for the annealing treatment. Figure 6.3a shows the EDS spectrum of the AZO film along with the elemental mapping showing the uniform distribution of aluminum in the film.

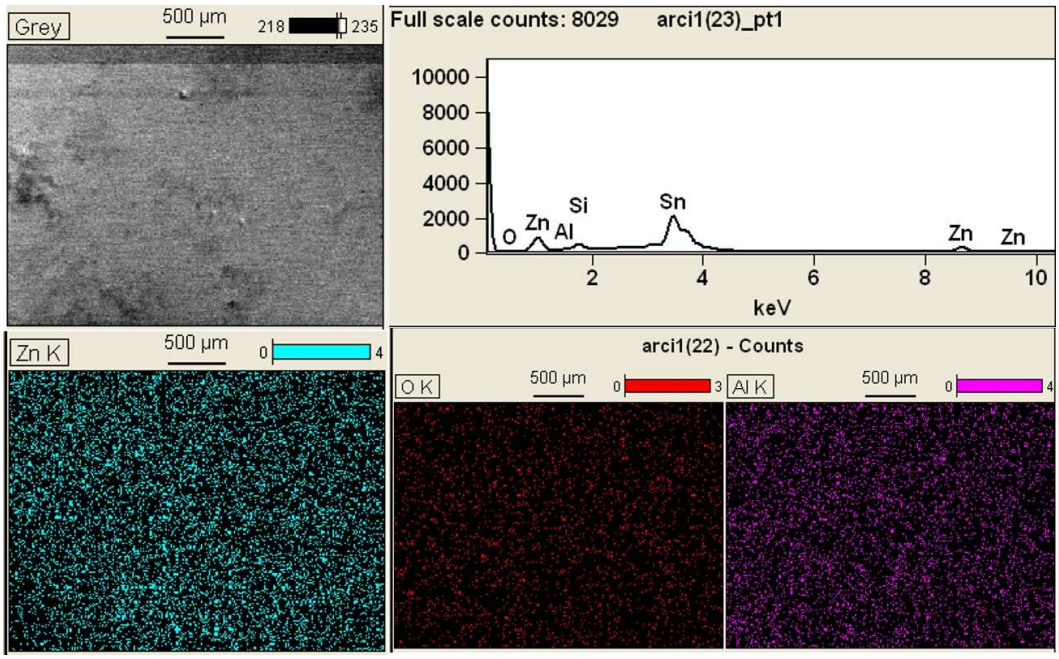

Figure 6.3: EDS spectrum and elemental mapping of the electrodeposited AZO thin film at -3.0 V, for 80 minutes

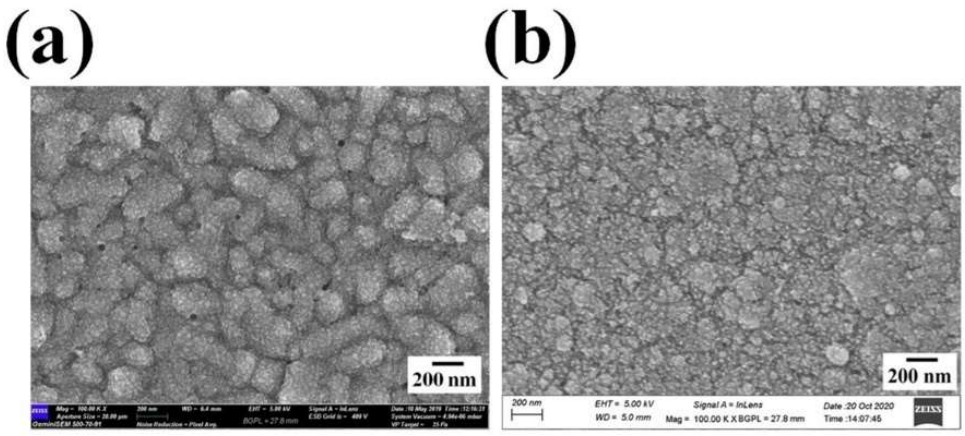

Figure 6.4: surface morphology of (a) as-deposited (b) annealed AZO thin film on FTO at -3.0 V for 80 minutes

Further, Figure 6.4a depict the surface morphology of the as-deposited AZO film deposited over FTO/glass at -3.0 V for 80 minutes. The morphology represents spherical granular grains deposited with good coverage over the substrate. Figure 6.4b illustrates a steady increase in the roughness of the films due to an increase in the grain size by recrystallization after annealing treatment in air at 300°C for 1hr.

6.2.4 Structural Analysis

Figure 6.5 depicts the XRD patterns of ZnO, as-deposited and annealed AZO films. The impact of annealing is studied by calculating the crystallite size and lattice parameters for the films from their preferred orientations using Equations

$$D = \frac{K\lambda}{\beta cos\theta} \quad (3.19),$$

$$a = \frac{1.54}{\sqrt{3}\, sin\theta} \sqrt{h^2 + hk + k^2} \quad (6.4),$$

and

$$c = \frac{2\sqrt{2} \times a}{\sqrt{3}} \quad (6.5)$$

respectively.

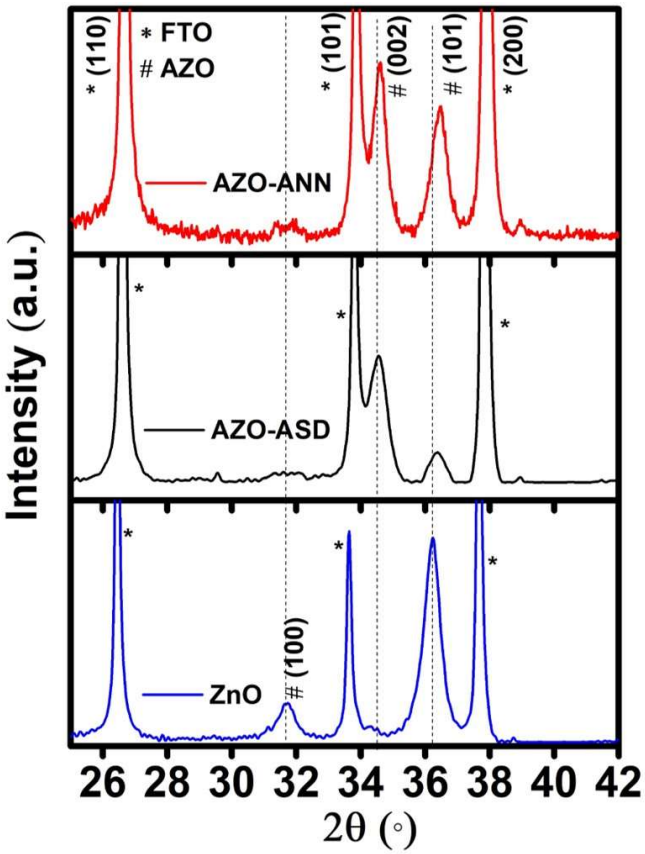

Figure 6.5: XRD patterns of as-deposited and annealed AZO thin films at – 3.0 V

The findings reveal that the deposited ZnO showed two strong and prominent peaks at 31.7° (100) and 36.3° (101) along with a broad peak at 34.3° (002) planes. This shows that the growth of the film is dominated in the (101) plane parallel to the substrate in line with previous reports (26). The as-deposited AZO films are having hexagonal phase with broad peaks at 34.4° (002) and at 36.4° with (101) orientation respectively (JCPDS 04-019-3163) as observed previously by Gal et al when chloride precursor salts are utilized for the deposition (17). However, when the films are annealed in air at 300 °C for 1 hr, there is a significant improvement in sharpness of the peaks with better crystallinity along with FTO substrate peaks with an asterisk symbol (*) (JCPDS 00-041-1445) as shown in Figure 6.5. The presence of two intense peaks at 2θ values 34.4° and 36.4° corresponding to the (002) and (101) orientations respectively are observed for the annealed films indicating the recrystallization of the films. The calculation of c/a ratio with 1.6 for the films before and after the annealing treatment revealed the formation of AZO with no secondary phases. Moreover, one can observe clear upshift in the 2θ value of AZO films both in the as-deposited and annealed films compared to the ZnO film due to incorporation of Al into ZnO lattice that replaces the Zn atoms. This causes reduction in the lattice parameter 'a' value due to differences in the atomic radii of Zn and Al atoms as given in Table 6.2 (27).

A typical calculation of texture coefficient determines the preferential growth of the films. This can be done as given in equation 6.6 and the values obtained for as-deposited and annealed films. It can be seen from **Table 6.2** that, there is a difference in the texture coefficient (TC) values of (100) and (101) of ZnO thin film that show higher value (~ 1.5) of TC for the (101) plane. Similarly, (101) and (002) orientation for the as-deposited films, having 1.4 for (101) that is referred to as the preferred growth for the films. As the films are annealed at 300 °C, 5°/min for 1hr, both the orientations (101) and (002) are predominant with the texture coefficient of >1.0 in agreement with the previous reports obtained from other methods for the solar cell applications (13, 14, 28, 29). The incorporation of Al atoms into the ZnO lattice is confirmed from the calculation of lattice parameters as per equations 5 and 6 where the c/a ratio for the films is calculated to 1.6 for both the (002), (101) planes that are agreeing well with JCPDS card (04-019-3163) (11). As expected, the narrower values of FWHM of the annealed film compared to the as-deposited films that are presented in Table 6.2 is related to the increment in the crystallite size showing better crystallinity of the film after the heat treatment. Comparative analysis of these

parameters represents the films annealed at 300 °C for 1 hr, with 5°/min ramp rate showed higher crystallite size ~ 17 nm with better crystallinity for both the (002) and (101) orientations.

$$a = \frac{1.54}{\sqrt{3}\,sin\theta}\sqrt{h^2 + hk + k^2} \quad (6.4)$$

$$c = \frac{2\sqrt{2}\times a}{\sqrt{3}} \quad (6.5)$$

Texture coefficient (TC) $\frac{I_{(hk\,)}/I_{0(hkl)}}{\frac{1}{N}\sum_{i=1}^{i=N} I_{(hk\,)}/I_{0(hkl)}}$ (6.6)

Where I(hkl), I_0(hkl) are the intensities of the XRD peaks of the film and the intensities of peaks of JCPDS card 04-019-3163 respectively, N is the number of peaks considered.

Table 6.2: Various parameters calculated from diffraction patterns of as-deposited and annealed AZO thin films

Sample	(hkl)	2θ (°)	Lattice parameter 'a' (Å)	c/a ratio	Texture coefficient	Crystallite size D (nm)	FWHM
ZnO	(100) (101)	31.7 36.2	3.3 2.9	1.6 1.6	0.5 1.5	11 14	0.8 0.7
As-deposited	(002) (101)	34.5 36.4	3.0 2.8	1.6 1.6	0.6 1.4	12 14	0.7 0.6
Annealed	(002) (101)	34.6 36.4	3.0 2.8	1.6 1.6	1.3 1.5	15 17	0.5 0.5

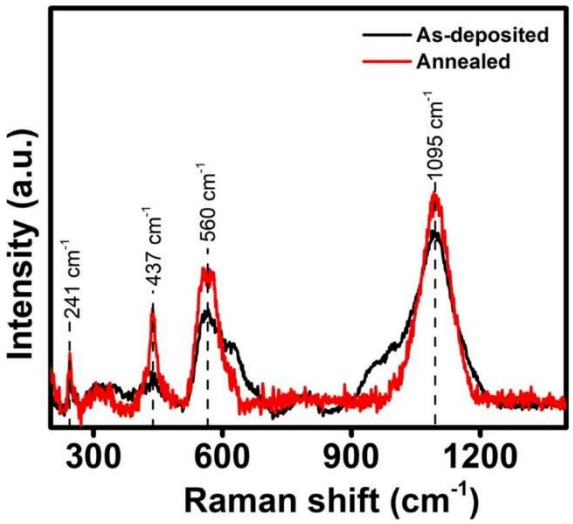

Figure 6.6: Raman spectra of AZO thin films before and after the annealing treatment

The structural aspects of the films are also analyzed using Raman spectroscopy. The thin films are incident with an Ar ion laser beam of about 532 nm. ZnO exhibits hexagonal wurtzite structure with C_{6v}^4 symmetry having 6 optical phonon modes A_1, $2B_1$ (silent), E_1, and $2E_2$. It is an excellent tool for interpreting the structure of the material for the lattice vibrations of the atoms. Figure 4 shows the comparable peaks of spectra obtained before and after the annealing treatment of AZO thin films. There are well-recognized peaks at 241, 437, 560 and 1095 cm^{-1} Raman shift are observed due to the lattice vibrations of the inorganic materials revealing ZnO. In both the cases, the peak positions are similar; however, sharper peaks with an increment in the Raman intensity for the annealed film. Another observation is the absence of E_1 (TO) mode that confirmed the c-axis orientation of grains in accordance with the available literature and corroborating with the XRD results **(30)**. The presence of intense peaks at 437, 560 cm^{-1} in the spectra, correspond to major contribution from E_2 (high) and E_1 LO modes, respectively **(31)**. The peaks at 560 cm^{-1} are most likely attributable to both the A_1 (LO) and E_1 (LO) modes due to the oxygen vacancies and free charge carriers in the thin films **(32)**. There also appears a peak at 241 cm^{-1} due to $2E_2$ (low) and the important feature of all these peaks more prominent for the annealed films compared to as-deposited ones. This signifies that the crystallinity is better solely due to the heat treatment owing to recrystallization of the grains. Another peak at 1095 cm^{-1} is identified to be A_1 (TO) mode due to the zinc interstitials and oxygen vacancy revealing the substitution of Zn atoms with Al atoms in the lattice. The most obvious feature is the phase-purity and high crystallinity for the TCO development, that are obtained in the present simple approach of doping Al into the ZnO lattice and outperforms the existing methods.

6.2.5 Optical Properties

The transparency of the generated films is investigated using UV-VIS-NIR spectroscopy which examines the ability of materials to interact towards the solar spectrum. Figure 6.7a shows the transmission spectra of pulse electrodeposited AZO thin films between 300-900 nm. The films with a thickness of 900 nm exhibited an average transmittance of 76% for the as-deposited film and 70 % for the annealed film. This reduction in the transmittance is attributed to the roughness of the grains after the annealing treatment as observed from FESEM analysis and by the other researchers (33). The bandgap of the AZO film is calculated from Tauc's equation (3.11)

and is determined to be ~ 3.4 eV for the as-deposited and 3.3 eV for the annealed film as shown in Figure 6.7b. This fall in the optical bandgap of the annealed film is due to the alteration in the surface morphology and particle size in agreement with the previous reports (34).

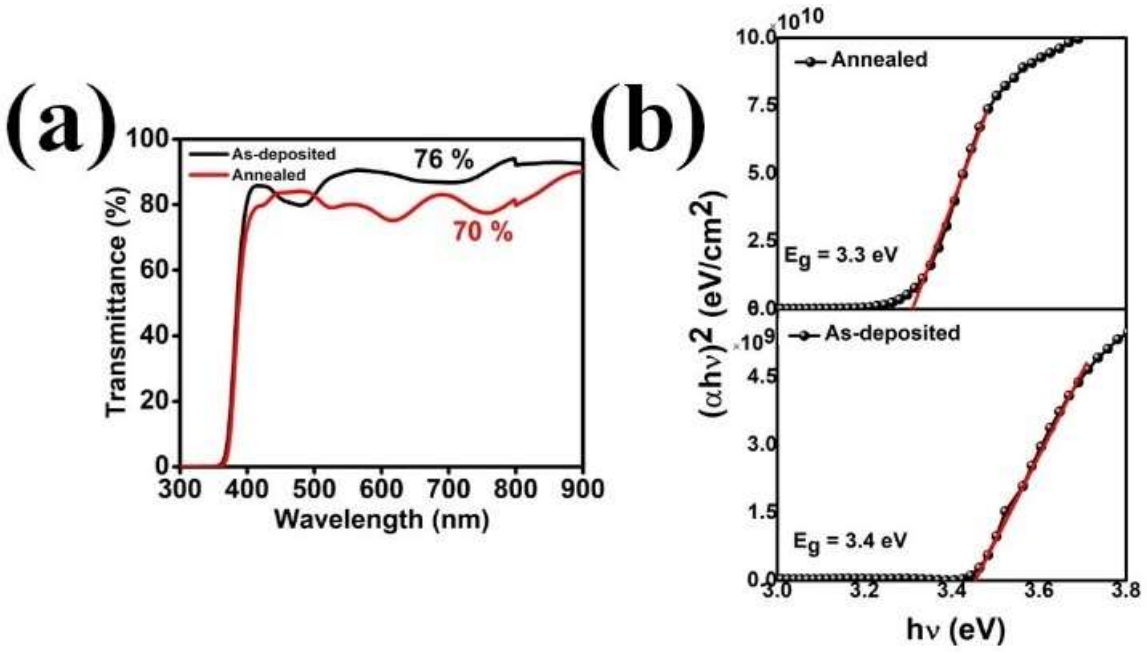

Figure 6.7: (a) Transmittance spectra and (b) Tauc's plots of the as-deposited and annealed AZO/FTO thin films deposited at -3.0 V for 80 minutes

6.2.6 Mott-Schottky Analysis

The Mott-Schottky analysis for the pulse electrodeposited (at – 3.0 V potential) AZO films is depicted in Figure 6.8. The positive slope of the curves indicates the n-type semiconducting behavior of the film. The flat band potential is found to be - 0.9 V vs SCE for the as-deposited film and -0.8 V vs SCE for the annealed film that is in good agreement with the reported value (35).

The carrier density is calculated from the slope of the curves using equation $N_D = \frac{2}{\varepsilon\varepsilon_0 e slope}$ (3.15) and is determined to 1.3×10^{18} and 4.8×10^{18} cm^{-3} for the as-deposited and annealed films respectively. This reduction in the flat band potential and increment in the carrier concentration values from as-deposited to annealed ones is due to the possible loss of adsorbed oxygen that creates oxygen vacancies and decreases the band energy levels.

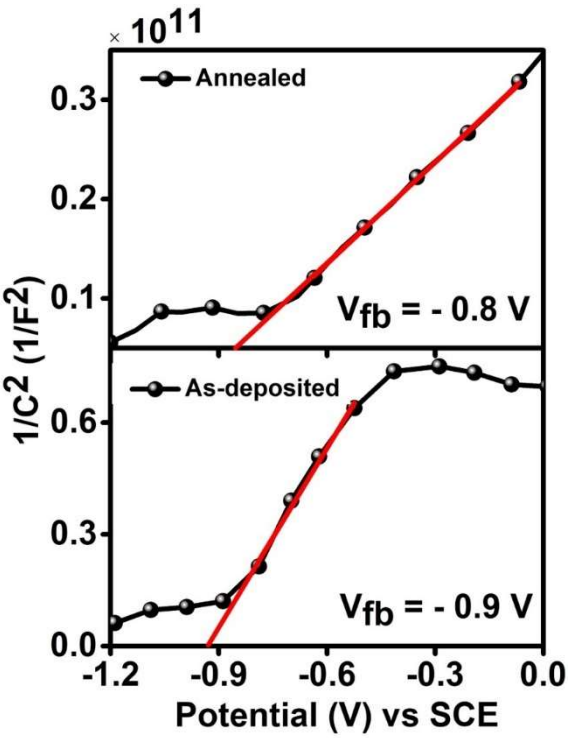

Figure 6.8: Mott-Schottky analysis of the as-deposited and annealed AZO thin films

6.2.7 Electrochemical Impedance Spectroscopic Analysis

Electrochemical impedance analysis helps in the evaluation of the rectifying property of the semiconductor thin films. The measurements are carried out in the frequency range of 1kHz to 0.1Hz with an amplitude of 5mV at an applied potential of -1.0 V vs SCE

Figure 6.9 shows the Nyquist plots of both the as-deposited and annealed electrodeposited AZO thin films. Changes in the impedance parameters with annealing, verify the electrical behavior of the films. The experimental data are fitted with the equivalent circuit having semicircle with notation R_s which gives the solution resistance and R_{ct} the charge transfer resistance as shown in Figure 6.9. This indicates the diffusion of ions towards electrode and thereby defines the resistance between the electrode and liquid electrolyte forming a double layer with capacitance. The impedance parameters obtained after fitting are presented in Table 6.3

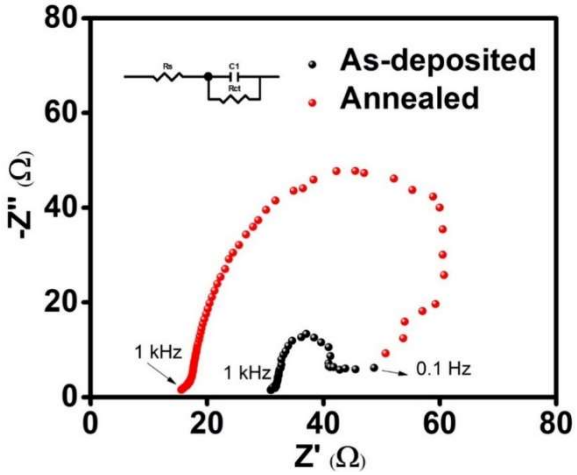

Figure 6.9: Impedance spectra of the as-deposited and annealed AZO thin films at -3.0 V

It can be viewed from Table 6.3 that, there is a significant increment in the charge transfer resistance (R_{ct}) for the films after the annealing treatment. This is due to the enlarged grains with fewer grain boundaries that resulted in the uniform coating over the FTO substrate and hence the diffusion of electrolyte is less. However, the capacitance values attained are higher and R_{ct} values are lesser for the as-deposited films when compared to the annealed films. This behavior is attributed to the porous grain structure of the film before the annealing treatment, therefore the diffusion of electrolyte takes place through the coating (36).

Table 6.3: Effect of annealing treatment on the impedance parameters of the electrodeposited AZO films

Sample	R_s (Ω)	R_{ct} (Ω)	Capacitance (C) (μF)
As-deposited	31	2.6	1696
Annealed	16	4.5	1184

6.3 Summary

Al-doped ZnO thin films are successfully electrodeposited from non-aqueous electrolyte DMSO using Al foil as a source of Al. The impregnation of metal foil in the electrolyte during the electrochemical deposition of Al metal is explored for the first time. The outcome of the present work leads to the conclusion that mild corrosion of metal foil plays a vital role at elevated bath

temperatures in the release of Al^{3+} ions for the Al doping and forms Al: ZnO. The effectiveness of the procedure is reflected in the film's properties and has confirmed polycrystalline films with the hexagonal phase formation. It also has been observed that the annealing at 300 °C, 5°/min has a significant effect on the crystallinity of the film. Moreover, impedance measurements of the annealed AZO films revealed the high charge transfer resistance due to reduced grain boundaries and defect traps. Overall, this work offers a better, simple, and new approach to Al doping into the films with the use of metal foils and produces films with desirable properties.

References

1. H. Kong, P. Yang and J. Chu, *Journal of Physics: Conference Series*, **276**, 012170 (2011).
2. J. L. Dan Chen, Rongkai Lu, Lingxiang Chen, and Zhizhen Ye, *IEEE TRANSACTIONS ON ELECTRON DEVICES*, **64**, 2549 (2017).
3. D. Ramírez, D. Silva, H. Gómez, G. Riveros, R. E. Marotti and E. A. Dalchiele, *Solar Energy Materials and Solar Cells*, **91**, 1458 (2007).
4. Y. Sun, T. Maemoto and S. Sasa, in *2014 IEEE International Meeting for Future of Electron Devices, Kansai (IMFEDK)*, p. 1 (2014).
5. M. Kemell, F. Dartigues, M. Ritala and M. Leskelä, *Thin Solid Films*, **434**, 20 (2003).
6. T. Minami, *Thin Solid Films*, **516**, 5822 (2008).
7. S. Chen, G. Carraro, D. Barreca, A. Sapelkin, W. Chen, X. Huang, Q. Cheng, F. Zhang and R. Binions, *Journal of Materials Chemistry A*, **3**, 13039 (2015).
8. M. Thambidurai, J. Y. Kim, J. Song, Y. Ko, N. Muthukumarasamy, D. Velauthapillai and C. Lee, *Solar Energy*, **106**, 95 (2014).
9. A. Hadri, M. Loghmarti, A. Mzerd and M. Taibi, in *2014 International Renewable and Sustainable Energy Conference (IRSEC)*, p. 61 (2014).
10. A. Tello, H. Gómez, E. Muñoz, G. Riveros, C. J. Pereyra, E. A. Dalchiele and R. E. Marotti, *Journal of The Electrochemical Society*, **159**, D750 (2012).
11. M. L. a. A. M. Adil Hadri, Mhamed Taibi, *IEEE* (2014).
12. F. Nasirpouri, *Electrodeposition of Nanostructured Materials* (2017).
13. K. D. Arun Kumar, S. Valanarasu, V. Ganesh, M. Shkir, S. AlFaify and H. Algarni, *Journal of Materials Research*, **33**, 1523 (2018).
14. O. Baka, A. Azizi, S. Velumani, G. Schmerber and A. Dinia, *Journal of Materials Science: Materials in Electronics*, **25**, 1761 (2014).
15. J. Kim, J.-H. Yun, Y. C. Park and W. A. Anderson, *Materials Letters*, **75**, 99 (2012).
16. P. Fuchs, H. Hagendorfer, Y. E. Romanyuk and A. N. Tiwari, *physica status solidi (a)*, **212**, 51 (2015).
17. R. Jayakrishnan and G. Hodes, *Thin Solid Films*, **440**, 19 (2003).
18. D. Kang, D. Lee and K. S. Choi, *Langmuir : the ACS journal of surfaces and colloids*, **32**, 10459 (2016).
19. J. Ao, R. Fu, M. J. Jeng, J. Bi, L. Yao, S. Gao, G. Sun, Q. He, Z. Zhou, Y. Sun and L. B. Chang, *Materials*, **11** (2018).
20. A. T. a. R. M. L. Legrand, *Electrochimica Acta*, **41**, 2715 (1996).
21. T. Clark, J. S. Murray, P. Lane and P. Politzer, *J Mol Model*, **14**, 689 (2008).
22. Y. Wu, F. Cao and X. Ji, *Journal of Materials Science: Materials in Electronics* (2020).
23. F. M. a. J. S. Qiongqiong Hou, *Nanoscale Research Letters*, **8** (2013).
24. T. Amakali, L. S. Daniel, V. Uahengo, N. Y. Dzade and N. H. de Leeuw, *Crystals*, **10** (2020).
25. R. Mahdavi and S. S. A. Talesh, *Advanced Powder Technology*, **28**, 1418 (2017).
26. M. Fahoume, O. Maghfoul, M. Aggour, B. Hartiti, F. Chraïbi and A. Ennaoui, *Solar Energy Materials and Solar Cells*, **90**, 1437 (2006).
27. D. Aryanto, P. Marwoto, T. Sudiro, A. S. Wismogroho and Sugianto, *Journal of Physics: Conference Series*, **1191** (2019).
28. F. Z. Bedia, A. Bedia, M. Aillerie, N. Maloufi, F. Genty and B. Benyoucef, *Energy Procedia*, **50**, 853 (2014).

29. H. Lahmar, A. Azizi, G. Schmerber and A. Dinia, *RSC Advances*, **6**, 68663 (2016).
30. M.-C. Huang, T.-H. Wang, S.-H. Cheng, J.-C. Lin, W.-H. Lan, C.-C. Wu and W.-S. Chang, *Nanoscience and Nanotechnology Letters*, **6**, 210 (2014).
31. M. Belhaj, C. Dridi, H. Elhouichet and J. C. Valmalette, *Journal of Applied Physics*, **119** (2016).
32. D. N. Montenegro, V. Hortelano, O. Martínez, M. C. Martínez-Tomas, V. Sallet, V. Muñoz-Sanjosé and J. Jiménez, *Journal of Physics D: Applied Physics*, **46** (2013).
33. J. Sengupta, R. K. Sahoo and C. D. Mukherjee, *Materials Letters*, **83**, 84 (2012).
34. A. K. Zak, Abrishami, M. Ebrahimizadeh, Majid, W. H. Abd, Yousefi, Ramin, Hosseini, S. M., *Ceramics International*, **37**, 393 (2011).
35. C. F. Windisch and G. J. Exarhos, *Journal of Vacuum Science & Technology A: Vacuum, Surfaces, and Films*, **18**, 1677 (2000).
36. S. Majumder, A. C. Mendhe, D. Kim and B. R. Sankapal, *Journal of Alloys and Compounds*, **788**, 75 (2019).

CHAPTER 7

FABRICATION OF ALL-ELECTRODEPOSITED CIGS SOLAR CELL

CHAPTER 7
FABRICATION OF ALL-ELECTRODEPOSITED CIGS SOLAR CELL

7.1 Introduction

In the development of all electrodeposited CIGS solar cells, each layer of the stack is optimized and deposited using electrodeposition technique. In this view, the top most layer of the complete stack (Mo/CIGS/CdS/ZnO/AZO) includes the transparent conducting oxide Al: ZnO and *i*-ZnO. However, the use of ZnS thin film as buffer layer omits CdS and i-ZnO layers due to the wide bandgap for band alignment between CdS and AZO layers. Therefore, the number of layers are reduced during the preparation (Mo/CIGS/ZnS/AZO). The use of electrodeposited stack layers are explored by Kemell et al for the first time wherein they studied the devices Mo/CIS/ZnO:Al, Mo/CIS/i-ZnO/ZnO:Al, Mo/CIS/CdS/ZnO:Al(1). The present work deposited Al:ZnO with a unique process of Al doping using the Al metal foil as precursor. The films are deposited using pulse electrodeposition in potentiostatic mode. The films are deposited both on FTO and Mo substrate for studying the optical properties, structural and morphological aspects. Prior to the inclusion of AZO films for the device fabrication, the optimization is performed on Mo substrate and compared with AZO on FTO for the structural aspects and grain growth. The as deposited films are annealed under air at varied temperatures, ramp rate, and duration. The film thickness is measured using stylus Profilometer and cross-sectional analysis which is found to be ~300 nm.

7.2 CIGS Device Fabrication using Conventional CBD-CdS as Buffer Layer

For device fabrication, the prepared CISe (approach 1) and CIGSe (approach 3) absorbers from multilayer depositions are used. The n-type CdS is deposited using a conventional chemical bath deposition process that includes precursors for Cd & S, and ammonium hydroxide as a complexing agent. The chemical reaction is allowed for 8 minutes at temperature 65^{o}C with agitation, as detailed elsewhere (2). Finally, ZnO and AZO layers are deposited by DC sputtering, which also serves as the device's top contact connecting terminals and extracting the power (3).

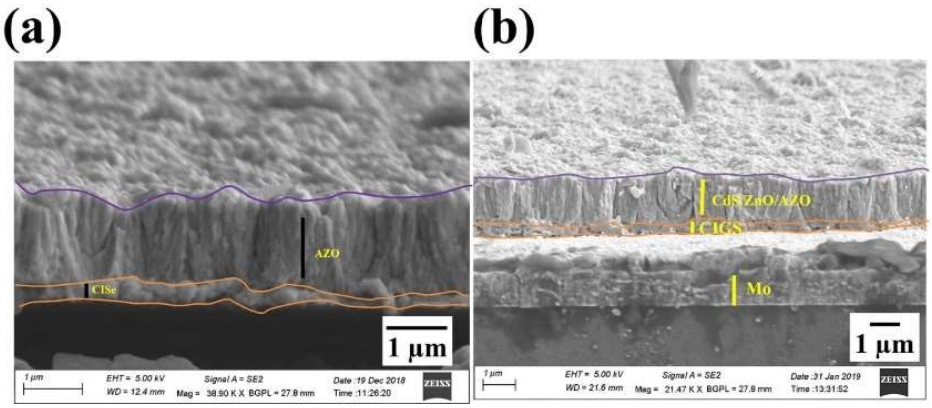

Figure 7.1: Cross-section of (a) CISe (b) CIGSe device

Figure 7.1 shows the cross-section FESEM images of the devices various stack layers. The cross-sectional examination of both devices revealed an absorber thickness of around 250 nm for CISe and CIGSe absorbers.

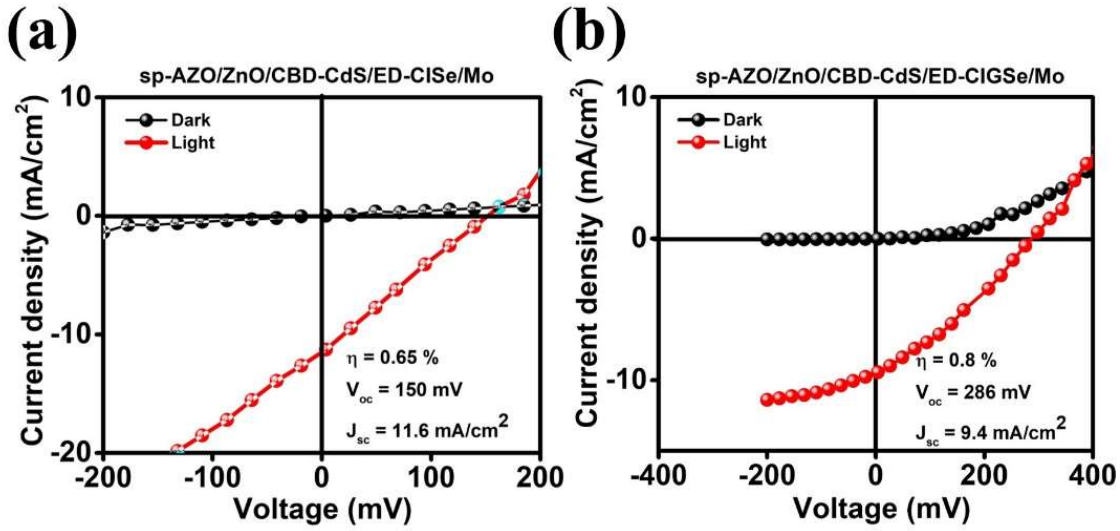

Figure 7.2: I-V characteristics of (a) CISe (b) CIGSe solar cell

The I-V characteristics of the devices are examined under dark and illumination to validate the performance of absorber deposited using multilayer approach. It is well understood from Figure 7.2a and b, that the power conversion efficiency of a CIGSe device is greater than that of a CISe device. They are about 0.6 % for CISe and 0.8 % for CIGSe indicating of photoactivity of the absorber films. These findings imply that the low efficiency may be caused due to thin

absorbers that need to be improved. This suggests that the duration of deposition has a significant effect on thickness, and hence both precursors deposited for around 15 minutes have equal thickness. In addition, multiple layers of the device, as well as the substrate Mo, are visible. It is crucial to highlight that, despite very thin absorbers, the absence of voids within the absorber is a good indication that these approaches have the potential to make superior films with further refinement (4).

7.3 Device Performance of CIGS Device with Electrodeposited CdS Buffer Layer

Under standard conditions, the power generated by the constructed solar cell is evaluated using solar simulator. **Figure 7.3**b shows the I-V characteristics of the device with a 1.0 % conversion efficiency with 800 nm CISe absorber and 20 nm CdS buffer layer. This improvement in efficiency over earlier devices suggests that increasing absorber thickness can limit carrier recombination to the rear contact. However, the nature of the curve implies that there is still series resistance existing due to the contacts as no metal grids are used.

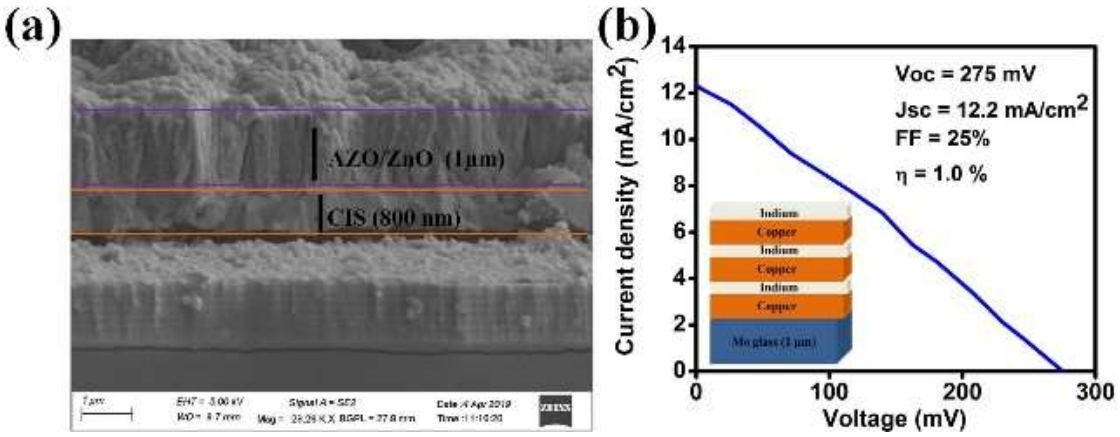

Figure 7.3: (a) Cross section of the CIS device with ED-CdS (b) J-V Characteristics of the CISe device

Figure 7.4a depicts the successive deposition of copper gallium and indium layers (4.3.2), followed by selenization to form the CIGS absorber layer. As per the elemental analysis, the composition with the indium rich film included less gallium. The device's buffer layer is ED-CdS, while the TCO layers are sputtered ZnO/AZO. **Figure 7.4**b's, cross-sectional view clearly reveals the absorber layer, which has a thickness of roughly 800 nm. A closer look at the absorber layer reveals several imperfections that result in smaller CIGS grains with more grain boundaries, which

contributed to recombination creating shunting channels. The J-V characteristics of a CIGS solar cell with electrodeposited CdS as a buffer layer are shown in **Figure 7.4**c. The device fabricated in this approach resulted in a conversion efficiency of 1.3.%.

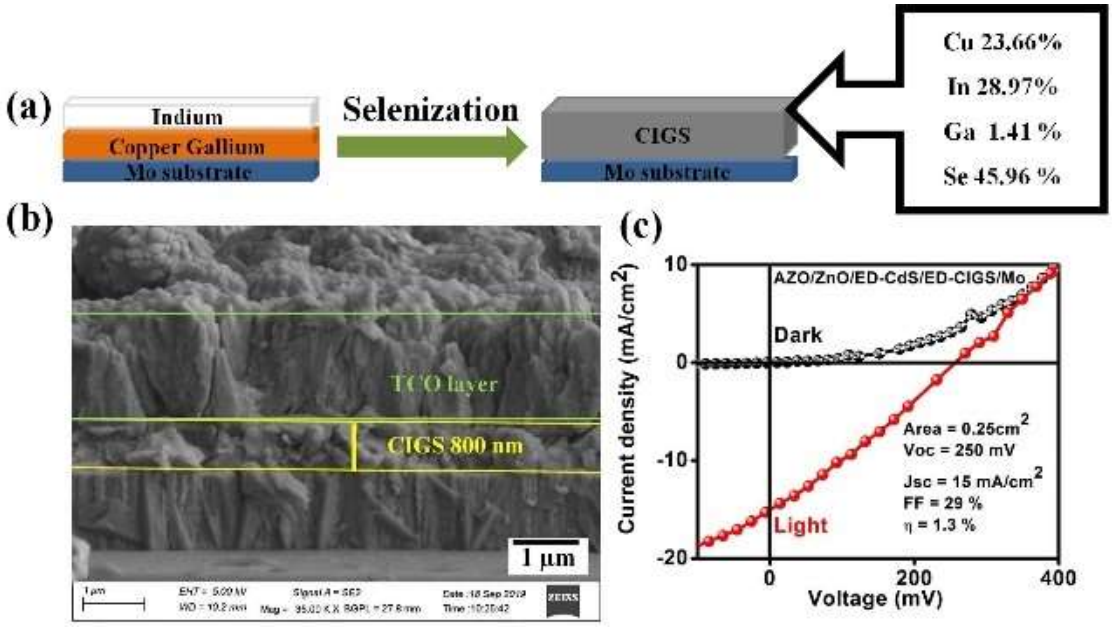

Figure 7.4: (a) Schematic of CIGS deposition and elemental composition (b) Cross sectional analysis and (c) I- V characteristics of the CIGS device

7.4 Photovoltaic performance of CIGS device with electrodeposited ZnS as buffer layer

Further, the photovoltaic performance of CIGS solar cells is studied using ED-ZnS as the buffer layer. Figure 7.5a shows the cross-section of the Cd-free CIGS solar cell that displays the different stack layers of the device including the electrodeposited absorber thickness of about 200 nm

Figure 7.5b depicts the J – V characteristics under dark and illuminated conditions. The measurement reveals the diode behavior of the cells and exhibits a conversion efficiency of about 1.6 % with other derived parameters as V_{oc} = 0.3 V, J_{sc} = 17 mA cm^{-2}, Fill factor = 29 %. The low V_{oc} and low J_{sc} attributes to the possible defects due to thin CIGS absorber layer. This is the first-ever device fabricated using electrodeposited ZnS as an intermediary layer for CIGS solar cells and further studies can scope to enhance the device performance.

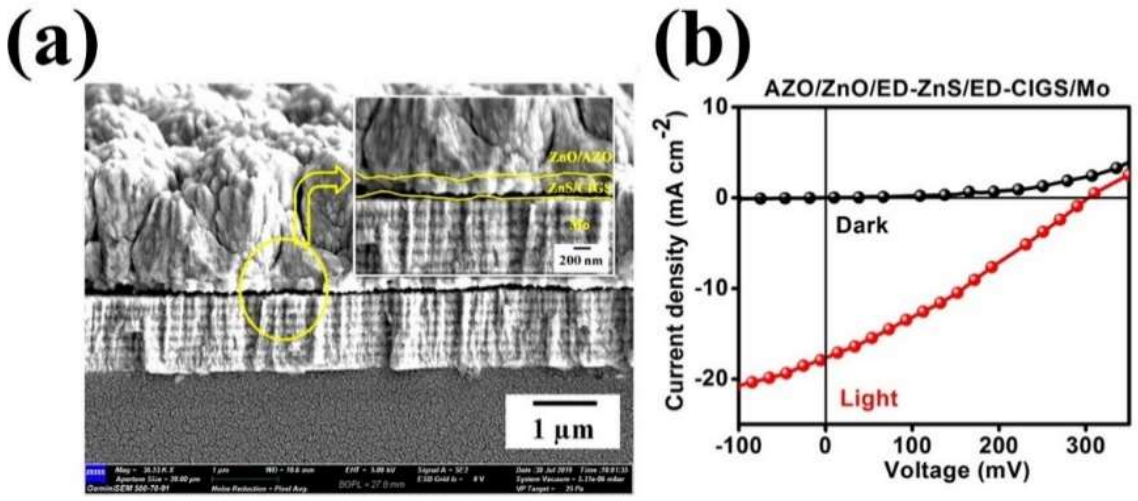

Figure 7.5: (a) Cross-section of Cd-free CIGSe solar cell (b) J – V characteristics of CIGSe solar cell with electrodeposited ZnS as a buffer layer

7.5 Optimization of AZO Thin Films on Mo substrate

7.5.1 Surface Morphology

In order to obtain better crystallinity, the films are annealed at different temperatures and the ramp rates. The annealing treatment is performed on the reproduced films deposited with identical experimental conditions to observe the effect of annealing treatment at different conditions.

Figure 7.6a, a' depicts the surface and cross-section of as deposited AZO films deposited for 30 minutes at 25% duty cycle. Figure 7.6b, b' shows the cross-section of films annealed at 300 °C with ramp rate at 2°/min. Here, the aligned grains are compact and uniform revealed that they are substantially better than the as-deposited AZO films. From, Figure 7.6d, d' it is seen that when the AZO thin films deposited on Mo and annealed at 300 °C, 5°/min, island growth of the grains is observed. The grains beneath the larger ones appears quite smaller compared to the top layer. This is due to the incomplete crystallization of the grains at this temperature.

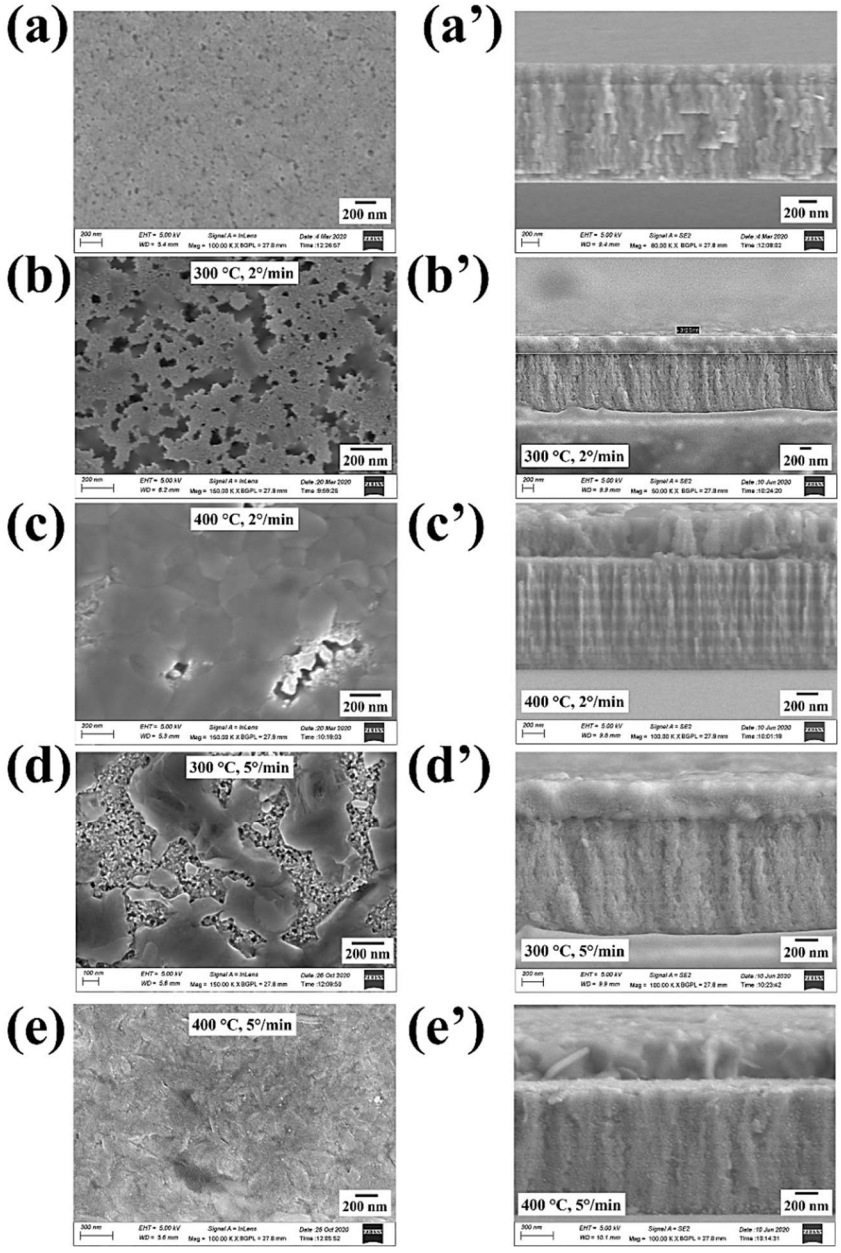

Figure 7.6: Planar and cross-sectional view of AZO/Mo thin films (a) & (a') As-deposited (b) &(b') annealed at 300°C, 2°/min; (c) &(c') annealed at 400°C, 2°/min; (d) & (d') annealed at 300°C, 5°/min; (e) & (e') annealed at 400°C, 5°/min for 1 hr duration

Figure 7.6c, c' shows the films annealed at 400 °C ramping at 2°/min with incomplete recrystallization in the planar view. Further, it is observed that the growth is better at 400 °C temperature with 5°/min having closely packed crystalline grains as shown in Figure 7.6e, e'

compared to Figure 7.6c, c' at 2°/min. With these observations, it can be concluded that the films annealed at 400 °C with 5 °/min ramp rate show desired properties.

7.5.2 Structural Analysis

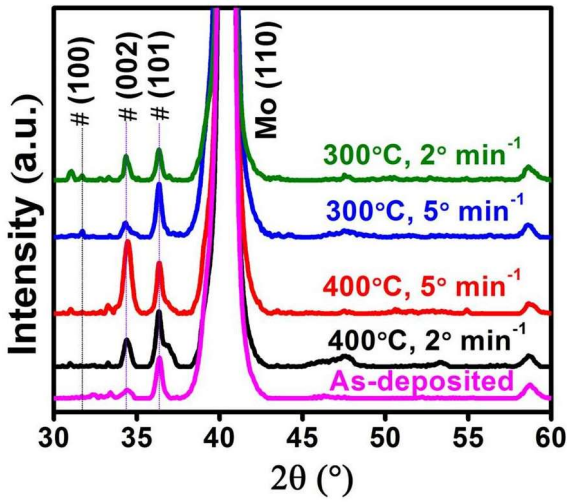

Figure 7.7: XRD patterns of AZO thin films at varied annealing temperatures

Figure 7.7 presents the XRD patterns of annealed AZO/Mo/glass films are different temperatures at varied ramp rate. Regardless to the annealing temperature and ramp rate all the films confirmed the formation of hexagonal phase (5). The comparison of patterns has revealed that the films annealed at 300 °C at 2°C/min showed two dominant reflections corresponding to (002) and (101) having similar intensity of the planes. The films annealed at 300 °C at 5°C/min revealed dominant (101) orientation with retained (002) plane. Then, on increasing the annealing temperature to 400 °C at 5°C/min the (002) orientation dominates due to recrystallization of the films at high temperatures compared to film annealed at 400 °C at 2°C/min having both the orientation (002) and (101) corresponding to the hexagonal phase of the Al:ZnO formation. These results showed remarkable improvement in the quality of the grains showing the impact of annealing treatment.

Table 7.1: Various parameters calculated from diffraction patterns of as-deposited and annealed AZO thin films

Film	D (nm) (101)	D (nm) (002)	TC (101)	TC (002)	Sheet resistance (Ω/□)
As-deposited	44	12	0.3	0.4	4×10^7
Annealed 400 °C, 2°/min	22	17	0.9	1.1	6×10^6
Annealed 400 °C, 5°/min	14	17	0.4	1.5	9×10^6
Annealed 300 °C, 5°/min	22	17	1.7	1.0	0.4
Annealed 300 °C, 2°/min	29	22	1.0	1.8	0.3

7.6 Incorporation of electrodeposited AZO into CIGS thin film solar cells

7.6.1 Surface Morphology

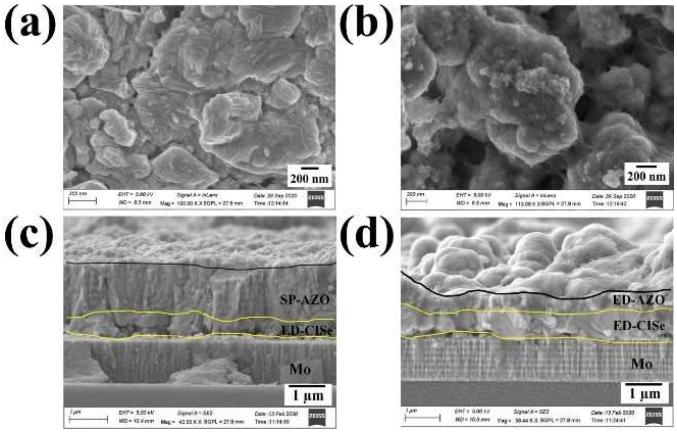

Figure 7.8: Surface morphology (a) Bare CISe/Mo (b) ED-AZO/ED-ZnS/ED-CISe/Mo and Cross-sectional analysis of (c) CISe device with sputtered AZO (d) CISe device with as-deposited AZO

On comparison of bare CIGSe absorber and the device fabricated using all electrodeposited layers in **Figure 7.8**b, it is observed that the bare CIGSe showed significant roughness with twinned grains having grain size of about 200-300 nm. Therefore, the surface of all electrodeposited device showed comparatively higher roughness of the grains due to low thickness of AZO layer. However, it is interesting to note that the absorber with CdS layer are uniformly covered with the AZO layer deposited using electrodeposition.

7.6.2 XRD Analysis

In order to understand the variation of structural aspects before and after annealing of electrodeposited AZO layer in the device, the XRD patterns are compared with the conventional device prepared using sputtered ZnO/AZO layer. In all the cases, the patterns showed peaks corresponding to CIGSe and AZO layers. Figure 7.9 represent the XRD patterns of CIGSe devices where it is observed that the device fabricated using sputtered AZO showed a very intense peak of (002) plane AZO. However, when the device is fabricated using all electrodeposited layers, the device with as deposited AZO showed broad peaks corresponding to the AZO with (101) dominant orientation.

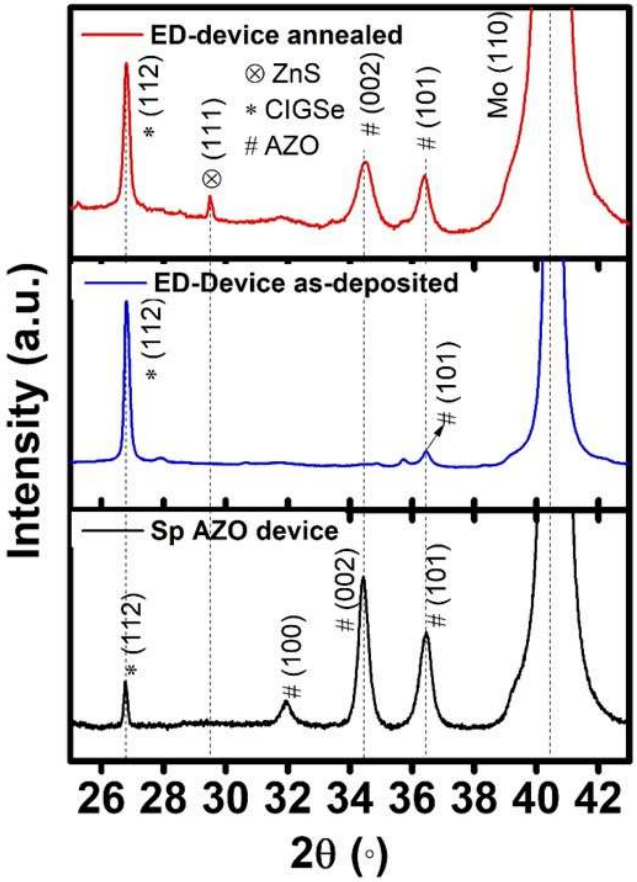

Figure 7.9: XRD patterns of devices fabricated using sputtered AZO and electrodeposited AZO layer

Further, when the device is annealed in the vacuum assisted furnace, the films showed better intense peaks of AZO with both the (002) and (101) planes. It is observed from the patterns that the AZO peak is dominating than the CIGSe absorber in the conventional device which indicates that the thickness of the AZO layer is very high with a crystallite size of about 20 nm. Then, in the all-electrodeposited device in its as-deposited condition it showed CIGSe peak dominating than the AZO peaks that are broad indicating that the film is still amorphous in nature. Moreover, the orientation of AZO is (101) which shows that the growth of AZO grains is parallel to the substrate. In the annealed condition, the AZO peaks are quite better compared to the as-deposited ones and also showed an improvement in the crystallite size from 11 nm to 17 nm. In conclusion, it can be said that there is a need for further improvement in the crystallinity of AZO layer for the all-electrodeposited device.

7.6.3 Impedance and I-V Characteristics

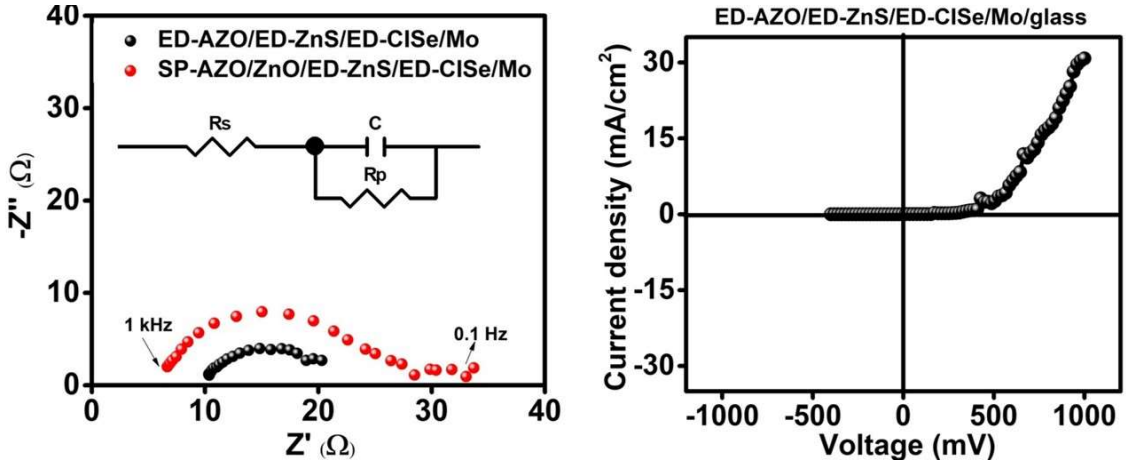

Figure 7.10: Nyquist plots of conventional device (left) and all-electrodeposited device along with the J-V characteristics of the all-electrodeposited device(right)

Impedance measurements plays an important role in evaluating the electrical properties of the devices on the conducting substrates. Figure 7.10 show the Nyquist plots for the conventional device and the all-electrodeposited device obtained in 0.1 M KOH in the frequency range of 1kHz to 0.1 Hz with an amplitude of 5mV/s. The obtained data are fitted with the equivalent circuit having series resistance (Rs), polarization resistance (Rp) and capacitance (C) components. From the fitted data, it is observed that the series resistance of conventional device with sputtered AZO is ~ 7Ω and that of electrodeposited device is ~ 10Ω at the higher frequency. Similarly, there is

also presence of charge transfer resistance which is ~ 2Ω for the all-electrodeposited device and it is 12Ω for the conventional device with sputtered AZO. This indicate that the device with electrodeposited AZO layer possess a greater number of grain boundaries with smaller grains or presence of amorphous grains leading to shunting path for the electrolyte to percolate and thus reduces the charge transfer resistance. On the other hand, there is better charge transfer resistance of conventional device due to obstruction of charged particles of electrolyte into the device due to less grain boundaries in sputtered AZO. Finally, it is also observed from the IV characteristics that the all-electrodeposited device still requires improvement in the electrical properties and hence no response is observed under illumination condition. However, the IV curve in Figure 7.10 shows the diode behavior of the device under dark indicating fewer shunting paths and but confirms the formation of pn junction.

7.7 Summary

In conclusion, the present method of depositing CdS showed reliability in pn junction formation at room temperature deposition with the CIGS absorber and showed the photovoltaic performance with ~ 1.3 %. Thus, this method breaks free the limitations of current approaches for producing ZnS thin-films and be fruitful for further exploration in the Cd-free solar cells. Further, a Cd-free CIGS device is constructed using room temperature electrodeposited ZnS as a buffer layer and gained a conversion efficiency of 1.6 %. High-quality CdS and ZnS films obtained by an economic pulse electrodeposition route without any high temperature requirement during deposition and/or post deposition high temperature treatment are of high relevance in practical applications in thin films solar cells and photoelectrochemical water splitting. Also, the use of wide bandgap semiconductor like ZnS can omit the ZnO layer that is used for the band alignment between absorber and window layers. These findings support the conclusion that reliable results can be obtained using the buffer layer prepared from this novel approach.

Moreover, the inclusion of ZnS not only omits CdS and ZnO but also offers wide spectral range to reach the absorber layer and extract the power. From the XRD results of devices fabricated, it is clearly observed that all the stack layers possess good crystallinity after annealing treatment. However, impedance studies showed better charge transfer properties for the sputtered AZO compared to the electrodeposited one. But there is still room to improve the grain structure with annealing treatment of all electrodeposited devices to obtain a work solar cell.

References

1. M. Kemell, F. Dartigues, M. Ritala and M. Leskelä, *Thin Solid Films*, **434**, 20 (2003).
2. A. C. Badgujar, R. O. Dusane and S. R. Dhage, *Solar Energy*, **199**, 47 (2020).
3. S. R. Dhage and A. C. Badgujar, *Journal of Alloys and Compounds*, **763**, 504 (2018).
4. N. Naghavi, F. Mollica, J. Goffard, J. Posada, A. Duchatelet, M. Jubault, F. Donsanti, A. Cattoni, S. Collin, P. P. Grand, J. J. Greffet and D. Lincot, *Thin Solid Films*, **633**, 55 (2017).
5. H. Kong, P. Yang and J. Chu, *Journal of Physics: Conference Series*, **276** (2011).

CHAPTER 8

SUMMARY AND CONCLUSIONS

CHAPTER 8
SUMMARY AND CONCLUSIONS

In summary, the main contribution of this thesis is the viability of producing an all-electrodeposited CIGSe thin film solar cell in the substrate configuration. The different stack layers of the CIGSe solar cell such as absorber, buffer and TCO are prepared using electrodeposition technique. This approach helps in device fabrication using a single technique that is time saving and cost effective. We have developed 4 different thin films and explored the pulse conditions to obtain the better properties for the photovoltaic applications.

S.No	Thin film	Novelty/improvement
1	Absorber CISe/CIGSe	Sequential deposition of Cu, In and Ga using methanol electrolyte with SDS additive and achieved phase pure CISe/CIGSe films
2	Buffer CdS and ZnS	Use of organic reagents such as tartaric acid and glycerol to produce phase pure crystalline thin films at room temperature without post annealing treatment
3	TCO layer Al:ZnO	Use of Al metal foil as a source for Al doping into ZnO films using DMSO electrolyte

8.1 Pulse Electrodeposition of CISe/CIGSe Absorbers

The development of absorber layer using methanol electrolyte with SDS additive was explored and detailed in chapter 4. The initial studies were carried out using aqueous electrolyte for the single pot deposition of Cu, In, Ga and Se during the electrodeposition. The films were then annealed or selenized at 550 °C to form CIGSe. However, this approach led to porous films even upon annealing and formation of $MoSe_2$ with uneven growth of CIGSe grains is observed during selenization treatment. It is therefore not surprising that the devices fabricated using these films resulted in shunting paths that deteriorated the devices. Addressing these issues, sequential deposition of metal stack is explored using non aqueous electrolyte methanol with SDS additive. The choice of SDS surfactant in the case of sequential deposition of metals such as Cu, In and Ga

was deemed most appropriate as it favored in grain refinement. Moreover, non-aqueous solvent such as methanol for the Cu and Ga deposition was helpful in widening the reduction potentials and facilitated the deposition of two metals together to form an alloy CuGa at -2.0 V, 50% duty cycle. However, in the case of indium deposition aqueous electrolyte with SDS worked well at -2.0 V, 50% duty cycle and produced uniform films.

8.2 Pulse Electrodeposition of CdS and ZnS at Room Temperature

The semiconductor thin films CdS are deposited utilizing pulse electrodeposition with an electrolyte comprising tartaric acid for pH control instead of conventional strong acids. In the instance of ZnS, a mixture of tartaric acid and glycerol is investigated for deposition onto several substrates, including FTO, Mo, and eventually CIGS/Mo, as reported in chapter 5. Tartaric acid was used in both cases to control the development of colloidal sulfur at the acidic pH and allow deposition at room temperature. ZnO, is the most often generated secondary phase during ZnS deposition, glycerol played a critical role in influencing the synthesis of ZnS. The films XRD patterns revealed polycrystalline hexagonal CdS and cubic ZnS structures. Mott-Schottky analysis revealed n-type conductivity and higher carrier density for the films deposited at room temperature without any post-annealing treatment.

8.3 Pulse Electrodeposition of ZnO/AZO Thin Films

The transparent conducting oxide Al:ZnO was used as the top layer for the CIGSe device preparation, and it also served as the top contact for power extraction in the current work. DMSO electrolyte is used to deposit the Al:ZnO films. After conducting preliminary trials with DC deposition, it is observed that direct current induced crack formation in the films. Therefore, pulse electrodeposition was investigated and deposited ZnO films as explained in Chapter 7. Similar approach is used in the case of AZO, where Al metal foil is employed as a source of Al doping and put into the electrolyte before beginning film deposition. The insertion of this foil is optimized while investigating the compositional and structural characteristics at various insertion temperatures. Deposition was carried out at -3.0 V, 25% duty cycle, and 90 °C. The film thickness is examined while depositing the films for various durations, and a direct correlation of thickness to their respective transmittance is observed, with a drop in transmittance of the films with a rise in thickness. Further research was conducted on the post-annealing treatment of the films, and it was discovered that films annealed at 300 °C have improved crystallinity, as evidenced by the

XRD results. The electrical properties of the films are examined using impedance measurements, and it is found that annealed films has low charge transfer resistance than as-deposited films. The results showed that the films were much more compact after annealing than as-deposited films. As a result, this method of depositing AZO can offer significant advantages over earlier methods that used Al salt as a precursor for Al doping to make Al:ZnO.

8.4 Fabrication of All-Electrodeposited CIGSe Solar Cell

Finally in chapter 7, the device performances are discussed wherein the electrodeposited CdS and ZnS buffers are incorporated for the CIGS thin film solar cells. CIGS devices are made from a 200nm thick CIGSe absorber with electrodeposited CdS and sputtered AZO demonstrated 1.3 % efficiency over a 0.5 cm^2 area. While the Cd-free device made with ED-ZnS had an efficiency of 1.6 %. The devices showed good device response and observed to possess semiconductor properties to form pn junction without heat treatment. Further, all the different stack layers are electrodeposited and produced an all-electrodeposited solar cell wherein CIGSe, ZnS and AZO is utilized. The use of ZnS not only omits CdS but also ZnO. This is a notable advantage where the use of ZnS without heat treatment was able to form the pn junction with the CIGSe absorber. As a final step AZO was deposited and annealed the device at 300 °C for 1hr. A comparative study was performed with ED-device and SP-device which possess sputtered AZO as the top contact. The XRD results clearly showed the presence of electrodeposited AZO before and after annealing treatment. The SP-device the sputtered AZO showed dominant AZO peak with higher intensity compared to the annealed AZO layer on the ED-device. This signals that the ED-AZO needs improvement in the crystallinity as well thickness when deposited on device. To interpret the electrical properties of the devices, impedance measurements were performed and observed that device with sputtered AZO showed low charge transfer resistance indicative of compact grains in contrast with electrodeposited device.

To further verify the photovoltaic performance, the I-V characteristics of the device was studied for the ED-device and observed no response in light but showed diode behavior in dark condition indicating the formation of pn junction which is also notable that no damage was done during annealing of the device. As it is difficult to solve the problems posed by both absorber and TCO layer, the aim was to at least ensure the formation of pn junction with intact layers of the

device. With these observations, it can be concluded that this work provides an easy fabrication process for the CIGSe device using pulse electrodeposition of different stack layers of the device.

8.5 Scope for Future Work

From the above conclusions, it can be suggested that future work can be done to improve the device fabrication and obtain a working device.

- Annealing treatment of the device can be done at 400 °C and study the photovoltaic behavior
- Use of UV treatment of the device to avoid the junction damage while improving the crystallinity of the AZO layer
- More studies will be needed to improve the deposition conditions of the galvanostatic mode to improve thickness of the CIGSe absorber

LIST OF PUBLICATIONS

Publications in Peer-Reviewed/Refereed International Journals

1. **Divya Boosagulla**, Sreekanth Mandati, Ramachandraiah Allikayala, and B. V Sarada, "Room Temperature Pulse Electrodeposition of CdS Thin Films for Application in Solar Cells and Photoelectrochemical Cells," *ECS Journal of Solid-State Science and Technology*., vol. 7, no. 8, pp. 440–446, (2018)
2. **Divya Boosagulla,** Sreekanth Mandati, Ramachandraiah Allikayala, and B. V Sarada, "Pulse Electrodeposition of CdS and ZnS thin films: Role of Tartaric acid in the Growth Mechanism" *Thin Solid Films*, 741 (2021).
3. **Divya Boosagulla**, Sreekanth Mandati, Prashant Misra, Ramachandraiah Allikayala, and B. V Sarada, "Pulse electrodeposited ZnS as an eco-friendly buffer layer for the Cd-free CIGS solar cells" *Superlattices and Microstructures*, Volume 160**,** 107060 (2021).
4. **Divya Boosagulla**, Ramachandraiah Allikayala, and B. V Sarada, "Al doped ZnO thin films using pulse electrodeposition by a novel process" (submitted)

List of co-author publications not included in PhD Thesis

5. Sreekanth Mandati, Prashant Misra, **Divya Boosagulla**, Tata Narasinga Rao and Bulusu V Sarada, "Economic pulse electrodeposition for flexible $CuInSe_2$ solar cells", *Materials for Renewable and Sustainable Energy*, 9 (2020)
6. Sreekanth Mandati, Prashant Misra, **Divya Boosagulla**, Tata Narasinga Rao and Bulusu V Sarada, "Control Over $MoSe_2$ Formation with Vacuum-assisted Selenization of One-step Electrodeposited Cu-In-Ga-Se Precursor Layers" 2020, *Environmental Science and Pollution Research*
7. Sreekanth Mandati, Prashant Misra, **Divya Boosagulla**, Tata Narasinga Rao and Bulusu V Sarada, "Solar Energy Harvesting through Photovoltaic and Photoelectrochemical Means from Appositely Prepared CuInGaSe2 Absorbers on Flexible Substrates by a Low-Cost and Industrial Benign Pulse Electrodeposition Technique" 2021, *Industrial & Engineering Chemistry Research*

LIST OF NATIONAL AND INTERNATIONAL CONFERENCES ATTENDED

1. **Divya Boosagulla,** Sreekanth Mandati, Ramachandraiah Allikayala and Sarada. V. Bulusu " Electrodeposition: An effective and economic technique for the fabrication of CIGS thin film solar cells" at *EIHE 2020, BARC Mumbai (poster presentation)*
2. **Divya Boosagulla,** Sreekanth Mandati, Ramachandraiah Allikayala and Sarada. V. Bulusu " Electrodeposition of ZnO and Al:ZnO as transparent conducting oxides for CIGS thin film solar cells" at *ACST 2019, NIT Warangal (Poster presentation)*
3. **Divya Boosagulla,** Sreekanth Mandati, Ramachandraiah Allikayala and Sarada. V. Bulusu " Electrodeposition of Device Quality Thin Films for the photovoltaic applications" at *MRSI 2019, IISc Bangalore (Poster presentation)*
4. **Divya Boosagulla,** Sreekanth Mandati, Ramachandraiah Allikayala and Sarada. V. Bulusu " Electrodeposition of ZnS Thin Films : Influence of Organic Acids on Structural and Optical Properties'' at *TSSC-2018, NIT Warangal (Poster presentation)*
5. **Divya Boosagulla,** Ramachandraiah Allikayala. & Sarada. V. Bulusu "Application of Electrodeposited CdS as n-type Semiconductor Layer for CIGS based Thin Film Solar Cells" at *ICASMD 2018, Hyderabad (poster presentation)*
6. **Divya Boosagulla,** Sreekanth Mandati, Ramachandraiah Allikayala and Sarada. V. Bulusu "Room temperature pulse electrodeposition of CdS thin films for application in solar cells" at *National conference on Recent Developments in chemical sciences and allied technologies (RDCST-2017), NIT Warangal (Oral presentation)*
7. Attended GIAN course on Advanced Materials for Sustainable Energy & Storage 23rdMay-3rd June 2016 at NIT Warangal